POLITECNICO DI MILANO

SCUOLA DI INGEGNERIA DEI PROCESSI INDUSTRIALI

DIPARTIMENTO DI CHIMICA, MATERIALI E INGEGNERIA CHIMICA "GIULIO NATTA"

LAUREA SPECIALISTICA IN INGEGNERIA DEI MATERIALI

LINEAR AND VOLUMETRIC STRAIN DETERMINATION BY 3D DIGITAL IMAGE CORRELATION: A STUDY ON PROPYLENE-ETHYLENE COPOLYMERS

Tutor for Politecnico di Milano:

Prof. Marta RINK

Tutor for Universitat Politècnica de Catalunya:

Prof. Antonio MARTÍNEZ BENASAT

Thesis by:

Lorenzo CORTI

749897

Academic Year 2010-2011

TABLE OF CONTENTS

INDEX OF FIGURES

INDEX OF TABLES

ABSTRACT

The linear and volumetric true strains under uniaxial tension are determined by 3D Digital Image Correlation in highly deformable polymers: a polypropylene homopolymer and four ethylene-propylene copolymers. Three issues were found during the application of this technique. Firstly, proper black and white paints have to be individuated to create the stochastic pattern. Secondly, a good randomly spread surface pattern necessary in order to facilitate the analysis has been obtained by optimizing the distance between the spray of paint and the specimen, the pressure on the valve and the time of exposition. Thirdly, the hardest problem was carrying out the analysis up to high strain. Initially the software could analyze the test until a true linear strain of almost 1, but a technique has been developed in order to overcome this problem and extend the range of analysis. The final 3D DIC technique adopted exploits a double analysis and the results are obtained by summing the partial strain values. The uniaxial tensile tests were conducted at constant strain rate. Hence, a crosshead rate profile has been set up for every material in order to obtain a constant strain rate in the most stressed section of the specimen. From the analysis of the uniaxial tensile tests the true stress-true strain and volumetric strain-linear strain curves of each material were obtained. The analysis of the behaviors suggests different deformation mechanisms one of which displays higher volumetric strain due to the presence of a more diffused cavitation phenomenon. This was shown by the three copolymers with the highest ethylene content. The second behavior was the one shown by the homopolymer which presents lower volumetric strain values due to the presence of low molecular fractions in the material. Moreover, one of the copolymer shows a behavior similar to the one of the polypropylene. This is related with the high molecular weight of the material. Finally, the volumetric strain curves show a decreasing trend at high linear strain. This is explained by a recrystallization phenomenon in the material and is supported by the results of the DSC analysis carried out.

ABSTRACT IN ITALIAN

Al fine di determinare la deformazione volumetrica di materiali polimerici altamente deformabili è stata utilizzata una tecnica Digital Image Correlation 3D. I materiali analizzati sono un polipropilene omopolimero e quattro copolimeri etilene-propilene. L'applicazione della tecnica DIC 3D ha incontrato alcuni problemi che hanno richiesto lo sviluppo di idonee soluzioni al fine di permettere una corretta analisi del comportamento dei materiali. Il primo problema affrontato è stato la scelta delle pitture utilizzate per creare il pattern random. Queste devono essere opache, presentare una buona aderenza con il substrato e deformarsi come il polimero. Il secondo problema incontrato è stato quello di ottenere un pattern disperso che renda possibile l'analisi delle immagini da parte del software. Infine, il problema di più difficile soluzione è stato permettere l'analisi dei tests da parte del software fino a deformazioni lineari elevate. Inizialmente, infatti, il software era in grado di analizzare le immagini fino a *true strain* modesti. La tecnica qui sviluppata permette di estendere il campo di deformazioni analizzabili raggiungendo valori molto elevati. L'analisi viene svolta in due steps e il risultato finale è dato dalla somma dei risultati parziali. Al fine di effettuare i test tensili a velocità di deformazione costante nella sezione più sollecitata del provino, è stato ricavato un profilo di velocità di spostamento della traversa per ogni materiale. Dall'analisi dei risultati dei tests di trazione uniassiali sono state ricavate le curve *true stress-true strain* e *volumetric strain-linear strain* dei cinque materiali. L'analisi di queste ultime evidenzia differenze nel meccanismo di deformazione tra l'omopolimero e i copolimeri. Nei copolimeri la deformazione volumetrica è più elevata a causa della presenza di un più diffuso fenomeno di cavitazione. Infine, le curve *volumetric strain-linear strain* ricavate, presentano un andamento decrescente per deformazioni lineari elevate. Ciò è dovuto alla presenza di un fenomeno di ricristallizzazione nel materiale e in tal senso concordano anche i risultati delle analisi DSC effettuate.

ESTRATTO IN ITALIANO

La maggior parte dei polimeri, se sottoposti a un test di trazione uniassiale, presentano un fenomeno di instabilità geometrica chiamato "necking". Per valori di deformazione maggiori di quello di necking i metodi tradizionali di misura delle deformazioni perdono di utilità. Un estensimetro meccanico, infatti, misura la deformazione media del provino seguendo la posizione relativa di due punti. Tuttavia, dopo il necking, la deformazione varia con la coordinata assiale del provino. Per questo motivo, lo studio del comportamento meccanico dei polimeri è spesso limitato a piccole deformazioni.

L'obiettivo principale di questo lavoro di tesi è lo sviluppo, l'ottimizzazione e l'applicazione di una tecnica DIC 3D a provini cilindrici di materiale polimerico altamente deformabile analizzando i risultati fino a deformazioni elevate. In letteratura sono presenti lavori simili a questo che, tuttavia, analizzano il comportamento dei materiali a deformazioni molto più piccole e nei quali non vengono quindi osservati alcuni dei fenomeni riportati in seguito. Una volta che la tecnica DIC 3D è stata ottimizzata sono stati ricavati i comportamenti true stress-true strain e volumetric strain-linear strain di cinque materiali: un polipropilene omopolimero e quattro copolimeri a blocchi etilene-propilene le cui caratteristiche sono riportate in Tabella i.

Materials	RMN		GPC			
	Ethylene content	Iso-tacticity index	Mn	Mw	Mz	Polydispersity (Mw/Mn)
PP 060	0 %	97.4	53000	396000	1250000	7.48
PB 110	6.9 %	83.3	160000	816000	2250000	5.09
PB 150	8.5 %	85.4	66000	353000	1030000	5.37
PB 170	8.5 %	84.2	56000	302000	880000	5.39
PB 171	11.2 %	81	61000	307000	880000	5.05

Tabella i: Caratteristiche dei materiali studiati.

Negli ultimi anni, sistemi di misurazione ottica delle deformazioni sono stati utilizzati con sempre più frequenza. A differenza dei sistemi meccanici, i sistemi ottici non operano a contatto con il provino; ciò è un notevole vantaggio nei test effettuati su polimeri (soprattutto quelli con basso modulo elastico) poiché viene completamente evitato l'effetto di concentrazione degli sforzi dato dal contatto tra estensimetro e provino.

Tra i sistemi di misura ottici si possono distinguere due famiglie differenti: i video estensimetri e i sistemi di analisi delle deformazioni a "tutto campo" chiamati Digital Image Correlation (DIC). Le tecniche DIC sono basate sulla comparazione di un pattern random posto sulla superficie del provino tra uno stato deformato e uno indeformato preso come riferimento. In questo modo si ottiene la distribuzione delle deformazioni locali senza conoscere il comportamento costitutivo del materiale a priori. I video estensimetri, invece, permettono la misura delle deformazioni di una piccola area della superficie del provino ma non localmente.

Tra i sistemi di misura DIC si possono distinguere tecniche 2D e 3D. la principale differenza tra le due è che le tecniche 2D visualizzano la superficie del provino come la sua proiezione su un piano perpendicolare alla direzione di osservazione; per questo motivo la misura delle deformazioni può risultare errata nel caso di materiali altamente deformabili o geometrie di provini che favoriscono spostamenti al di fuori del piano di visualizzazione. Al contrario, le tecniche DIC 3D, necessitano di una calibrazione del sistema prima di effettuare la misura che non è invece richiesta nel caso del 2D.

L'utilizzo di un sistema DIC permette di calcolare, anche nella zona maggiormente deformata del provino (i.e. la zona del neck), la *true strain*, il *true stress*, la deformazione di volume e il coefficiente di Poisson di ogni punto sulla superficie del campione. Questi dati possono poi essere elaborati ottenendo i comportamenti *true stress-true strain* e *volumetric strain-true strain* del materiale nel regime di post snervamento.

Tipicamente lo studio del comportamento meccanico a trazione dei polimeri (e dei materiali in genere) viene eseguito analizzando le curve ingegneristiche sforzo-deformazione; le quali tuttavia non colgono i fenomeni locali della deformazione. Per ovviare a questa mancanza svengono analizzate le curve *true stress-true strain* che riescono a evidenziare i comportamenti locali del polimero. Tuttavia, per ricavare questi

diagrammi, è necessario conoscere il campo di deformazioni in tutto il provino e il valore dell'area della sezione più sollecitata del provino stesso.

Lo sforzo vero viene calcolato con la seguente espressione:

$$\sigma_{true} = \frac{F}{A}$$

Dove F è il carico applicato e A è la superficie reale (tenendo conto delle deformazioni) della sezione più sollecitata del provino.

La deformazione volumetrica è un indicatore macroscopico dei processi deformativi microscopici. Il suo studio, infatti, permette di comprendere quali micromeccanismi di deformazione plastica agiscono nel polimero. La deformazione volumetrica viene calcolata con la seguente espressione:

$$\varepsilon_v = \varepsilon_1 + \varepsilon_2 + \varepsilon_3 = \ln\left(\frac{V}{V_0}\right)$$

Dove le tre ε sono le true strain nelle tre direzioni dello spazio nella sezione più sollecitata del provino.

Il meccanismo di deformazione del polipropilene è composto da diversi fenomeni che si innescano per livelli crescenti di deformazione: espansione elastica iniziale (indice di Poisson < 0.5); riorganizzazione della fase amorfa nella zona interlamellare che causa una compattazione del volume libero del materiale; stiramento delle catene molecolari nella zona amorfa interlamellare accompagnato da movimenti degli stack di lamelle e tra le lamelle stesse; distruzione della fase cristallina che si manifesta per deformazioni maggiori di quella di snervamento e che causa la progressiva trasformazione degli sferuliti in fibrille; e infine un fenomeno di cavitazione che si manifesta per deformazioni ancora maggiori e che rappresenta la causa principale dell'espansione volumetrica osservata nel polimero.

I copolimeri a blocchi etilene-propilene sono costituiti da due fasi: una matrice di polipropilene e una fase dispersa. La fase dispersa è tipicamente descritta come una struttura *core-shell* composta di tre livelli: un nucleo interno costituito dalle macromolecole a blocchi etilene-propilene ricche in etilene, uno strato intermedio

principalmente costituito da EPR e un secondo strato esterno costituito ancora da macromolecole a blocchi etilene-propilene ricche in propilene.

Il meccanismo di deformazione dei copolimeri a blocchi etilene-propilene avviene in tre fasi:

1. Le inclusioni agiscono da concentratori di sforzo creando un campo di sforzi triassiali all'interno delle particelle e nella matrice circostante.
2. Il crescente campo di sforzi triassiale causa fenomeni di cavitazione nelle particelle e di distaccamento all'interfaccia matrice/particella.
3. La cavitazione nelle particelle causa un rilassamento del campo di sforzi nella matrice che a sua volta causa la formazione di bande di scorrimento nel polipropilene; si ha quindi shear yielding nella matrice.

Come precedentemente esposto l'obiettivo principale del lavoro di tesi è l'applicazione di una tecnica DIC 3D a provini cilindrici di materiale polimerico altamente deformabile cercando di estendere il campo di deformazioni analizzabili. Questo ha rappresentato un problema di difficile soluzione; il software di analisi, infatti, riusciva ad analizzare le immagini solamente per piccole deformazioni. Si è reso dunque necessario lo sviluppo di una tecnica che permettesse il superamento di questo ostacolo: l'analisi viene eseguita in due steps. Nel primo step l'analisi viene effettuata fino al momento in cui il software riesce a misurare la deformazione della sezione più sollecitata del provino. Nel secondo step l'analisi viene effettuata prendendo come stato indeformato l'ultima immagine dell'analisi del primo step. Agendo in questo modo la deformazione totale è data dalla somma delle deformazioni parziali delle due analisi.

I test tensili sono stati eseguiti a velocità di deformazione costante in modo tale che i risultati tra i diversi materiali fossero confrontabili. Per questo si è reso necessario lo sviluppo di un profilo di velocità della traversa per ogni materiale che rendesse costante tale valore. Il profilo è stato ricavato con un metodo iterativo try-and-error.

Inizialmente è stato effettuato un test a velocità di spostamento della traversa costante dal quale è stato ricavato l'andamento *true strain-time*. Questo diagramma è stato suddiviso in sezioni in ognuna delle quali è stata calcolata la pendenza che è la velocità di

deformazione. È stato quindi disegnato un secondo profilo aumentando o diminuendo la velocità di spostamento della traversa nelle varie sezioni in funzione della differenza tra il valore della velocità di deformazione calcolato in quella sezione e un valore arbitrariamente scelto ($\dot{\varepsilon} = 0.15\ s^{-1}$). È stato quindi realizzato un secondo test di trazione adottando quest'ultimo profilo di velocità di spostamento della traversa e ottenendo un differente diagramma *true strain-time* analizzando il quale è stato rifinito il profilo. Agendo in questo modo, in un certo numero (dipendente dal materiale) di cicli iterativi è stato ottenuto un profilo che garantisce un valore di velocità di deformazione, nella sezione più sollecitata del provino, pressoché costante e confrontabile tra i diversi materiali.

Una volta ottimizzata la tecnica ottica di misura e messa a punto la tecnica meccanica sono state ricavate e analizzate le curve *true stress-true strain* e *volumetric strain-linear strain* dei cinque materiali in esame.

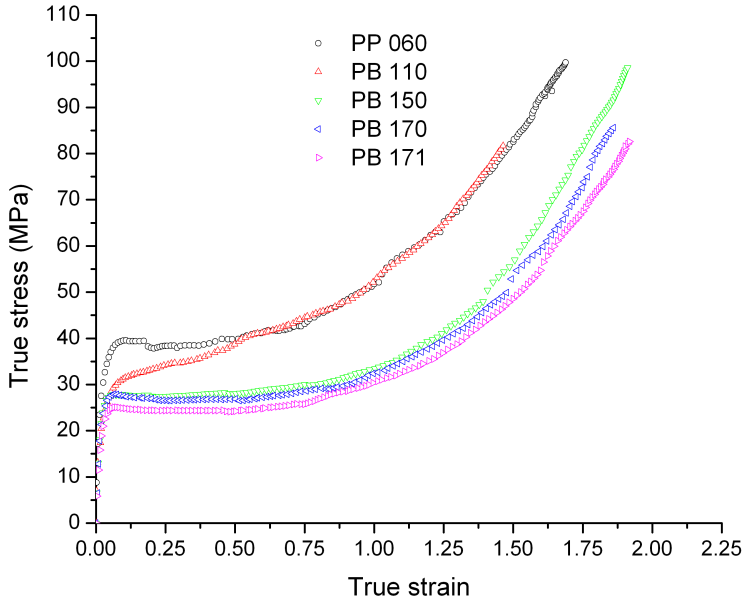

Figura i: Curve true stress-true strain dei cinque polimeri analizzati a velocità di deformazione costante.

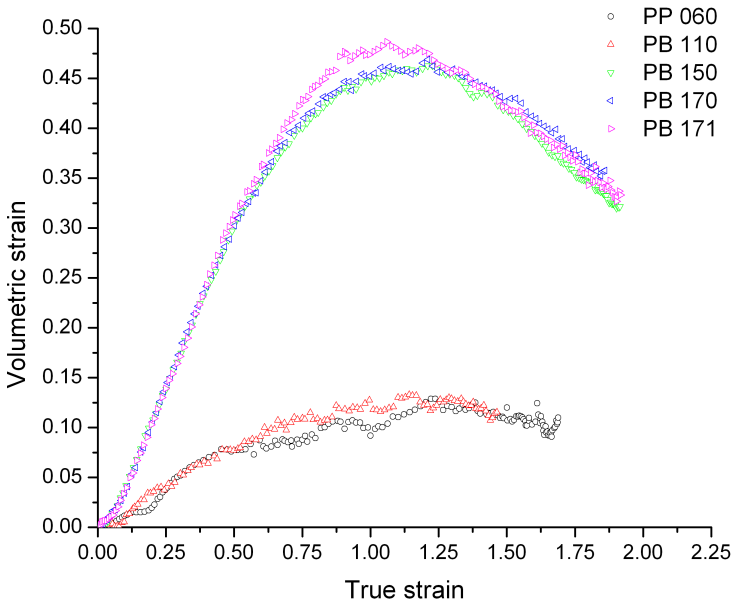

Figura ii: Curve volumetric strain-linear strain dei cinque materiali analizzati a velocità di deformazione costante.

Osservando i grafici in Figura i e Figura ii si possono ricavare alcune considerazioni:

- Tutti i materiali presentano un andamento comune nel primo tratto del diagramma *volumetric strain-linear strain*: la pendenza della curva è minore di quella a deformazioni lineari elevate. Il cambio di pendenza sembra avvenire in corrispondenza dello snervamento dei materiali e si pensa quindi che il differente comportamento sia dovuto ai meccanismi deformativi agenti nel materiale. In zona elastica non è ovviamente presente deformazione plastica e gli unici fenomeni agenti sono espansione elastica (coefficiente di Poisson < 0.5), compattazione delle macromolecole e cristallizzazione indotta. Questi ultimi fenomeni sono meccanismi di compressione volumetrica e, quindi, la deformazione di volume cresce lentamente.
- Diversamente da quanto riportato in letteratura il valore massimo di deformazione volumetrica del polipropilene omopolimero è relativamente basso. Questo può essere spiegato con il fatto che il polimero non è stato purificato prima dell'analisi e, quindi, presenta al suo interno frazioni a basso peso molecolare. Queste molecole tendono a riempire le cavità che costituiscono il volume libero del polimero e in corrispondenza delle quali si innesca la cavitazione ostacolandone quindi l'innesco e la crescita.

- Il materiale PB 110 pur essendo un copolimero a blocchi presenta un comportamento molto simile a quello dell'omopolimero e alquanto differente dagli altri tre copolimeri analizzati. La bassa deformazione volumetrica osservata si pensa sia dovuta alla presenza, nel materiale, di ponti fibrillari di polipropilene che stabilizzano i vuoti formati per cavitazione impedendone l'espansione. L'efficacia di questi ponti fibrillari è maggiore quanto più elevato è il peso molecolare del polimero e, come precedentemente illustrato (Tabella i), il PB 110 è il materiale con il peso molecolare maggiore tra quelli analizzati.
- Gli altri tre copolimeri a blocchi in analisi presentano valori di deformazione volumetrica molto superiori a quelli dell'omopolimero e del PB 110. Questo comportamento è dovuto ad un più esteso fenomeno cavitazionale sia nella matrice che nella fase dispersa del copolimero dovuto alla microstruttura del materiale.
- Tutti e cinque i materiali in analisi presentano un trend decrescente nella curva *volumetric strain-linear strain* per deformazioni molto elevate. Per spiegare questo andamento si è ipotizzato che nel materiale, durante la deformazione, avesse luogo un fenomeno di ricristallizzazione. A tal proposito sono state effettuate delle prove DSC su campioni indeformati e deformati dei materiali in analisi calcolando la cristallinità nei due casi. Confrontando i valori si è osservato che in tutti i materiali a eccezione del PB 110 la cristallinità nello stato deformato è superiore a quella nello stato indeformato. I risultati meccanici e termici convengono quindi alla medesima conclusione: si ha un incremento di cristallinità nel materiale dovuto alla deformazione che causa una diminuzione della deformazione volumetrica.

Chapter 1. Introduction

Ductile thermoplastics polymers like polypropylene and polyethylene are increasingly being used in the manufacturing industry. For some applications, as for example in automotive components, the main goals of using polymers is reducing weight and enhance passenger and pedestrian safety. A detailed knowledge about the behavior of these materials under severe deformations (e.g. crash accidents) is required in order to fully utilize their energy absorbing capabilities in a robust and crashworthy design. Knowledge of the intrinsic material behavior of polymeric materials from the small strain range up to ultimate failure is of crucial importance for developing adequate material laws for numerical modeling. Further, they are also fundamental for a deeper understanding of the microscopic deformation mechanisms necessary for material development.

During a uniaxial tension test, most engineering polymers begin to deform inhomogeneously ('neck') at relatively small strains, and the so-called "necking" occurs. Once necking begins, traditional deformation measuring methods provide little useful information. A contacting extensometer measures only the average strain over a gage length by tracking the relative position of two points on the specimen. Until the neck stabilizes and propagates over the length of the specimen, however, the strain varies with axial position on the specimen. For this reason, polymer tensile stress-strain data is often limited to small strains, and less is known about the post-yield tensile behavior of polymers. The data typically reported, engineering (nominal) stress versus strain, does not capture the local deformation phenomenology. In order to determine the more informative true stress-true strain data after the onset of necking, the local displacement field must be measured. Moreover, the determination of the true stress at a given axial location on the specimen requires knowledge of the actual cross-sectional area at that location.

However, in both their neat and filled forms, many polymers increase in volume during tensile extension. The interest in the measure of volumetric strain is that it can be a key macroscopic indicator of microscopic deformation processes. In homopolymers,

processes such as crazing (both in glassy amorphous and semicrystalline polymers) give rise to an increase in by volumetric strain. In filled polymers, the debonding of rigid particulate fillers or the cavitation of elastomeric fillers allows void growth, an additional source of volumetric strain. Debonding and cavitation are important events to quantify as they are considered a critical ingredient to toughening, acting to relieve stress triaxiality and enable dissipative plastic flow.

The presence of significant volumetric strain complicates the calculation of the true stress (load per current cross-sectional area) in the specimen during the tensile test. Traditional tensile testing techniques measure the axial strain and approximate the current cross-sectional area of the specimen by assuming constant volume. If the volumetric strain is not negligible, however, this assumption, in addition to being wrong causes the true stress to be overestimated. Displacements and strains must thus be measured not only in the axial direction but also in one (if transversely isotropic deformations may be assumed) or both lateral directions.

Recently, mechanical special extensometers were developed to measure simultaneously the strains in the three directions of space, but:

1. They are complicated to manipulate;
2. They are likely to damage locally the specimen;
3. They cannot be used at high temperatures;
4. They are not applicable to materials which exhibit necking, since their calibrated reference volume is much larger than the zone affected by plastic instability.

In addition to mechanical extensometry, optical strain measurement devices have been increasingly applied in recent years for various materials to characterize their mechanical behavior. In contrast to clip-on or contact extensometers, which are mechanically attached to the test specimen, optical measurement devices operate contactless. Optical techniques are particularly necessary for soft polymeric materials, as local stress concentrations arising from the indentation of the specimen and the weight of an attached mechanical extensometer are entirely avoided.

As for optical strain measurement systems two types can be distinguished: devices with a fixed gauge length on the test sample, commonly referred to as video extensometers, and full-field strain analysis system referred to as Digital Image Correlation (*DIC*). In general *DIC* is based on the principle of comparing speckle pattern structures on the surface of the deformed and undeformed sample or between any two deformation states. For this purpose, an optical camera system observes and follows a virtual grid of subset ("mesh" of facets). This grid is superimposed by the software on the preexisting or artificially sprayed-on surface speckle pattern. In this manner, the in-plane local strain distribution is gained without assuming the constitutive behavior of the material a priori. Furthermore, this method is independent of specimen geometry and can also be applied to complex parts and geometries to gain information on the deformation behavior of components in real service.

For traditional extensometry, the limits of resolution and accuracy are well known and can easily be determined. In the case of optical measurement devices (video techniques and DIC) the situation is more complicated, since resolution and accuracy depend on the whole measurement system including the objective, the camera and the light system. The number of pixels per mm, which represent an important characteristic as to the resolution of optical systems, strongly depends on the distance between camera and the specimen. Of specific importance, environmental conditions such as vibrations of the test equipment or glass panels between specimen and camera when testing at non-ambient temperatures may have a significant influence on the strain accuracy obtained. Moreover, out-of-plane movements of the specimen affect the apparent size of the specimen and, thus, may also alter the strain result in 2D measurements. Finally, the range of the depth of sharpness is limited and determines the operating distance to the measured object if significant out-of-plane movements occur.

As *DIC* provides a full description of longitudinal and transversal strain distributions also in the highly strained neck region of the specimen, true strain and true stress as well as Poisson's ratio and volume strain can be calculated, also giving information on the local strain history at each position of the specimen surface. Thus, *DIC* allows the determination of the true stress–true strain relationships in the post-yield regime.

The main objective of this work is to suitably apply a 3D *DIC* technique which allows the measurement of the three components of the strain in cylindrical specimens up to very large deformations. In the works present in literature no such values of strain was ever reached; all the authors analyzed the data up to lower deformations and, thus, do not observe some of the phenomena observed in this thesis work. Moreover, once the technique was set up, the true uniaxial stress-true strain and volume strain-true strain curves are determined for a polypropylene homopolymer and four propylene-ethylene copolymers with varying ethylene content and/or molecular weight.

Chapter 2. Background

2.1. Polypropylene and Copolymers

2.1.1. Polypropylene homopolymer

Polypropylene is a versatile thermoplastic material, compatible with many processing techniques and used in many different commercial applications. It is one of the fastest growing classes of commodity thermoplastics, with a market share growth of 6-7 %/year. The volume of polypropylene produced is exceeded only by polyethylene and polyvinyl chloride [1].

The moderate cost and favorable properties of polypropylene contribute to its strong growth rate. It is one of the lightest thermoplastics with a density of 0.9 g/cm^3. Due to its high strength-to-weight ratio it is more rigid than other polyolefins. It also has the highest melting temperature of all commodity thermoplastics (160-170°C) and better heat resistance than other low-cost thermoplastics.

Its excellent chemical resistance includes resistance to most organic solvents, except for very strong oxidizing agents. However, softening may occur due to the permeation of chlorinated solvents and hydrocarbons. Its good fatigue resistance makes it widely used in living hinge applications. Moreover, it is usually not susceptible to environmental stress cracking.

Polypropylene is available in a wide variety of melt flow rates and it is easily recycled. It can be processed by virtually all methods, including injection molding, blow molding, extrusion, blown and cast film, and thermoforming.

Many available grades with different properties make polypropylene useful in applications such fibers, films, filaments, and injection molded parts for automotive industry, rigid packaging, appliances, medical equipment, food packaging, and consumer products.

Polypropylene is prepared by polymerizing propylene, a gaseous byproduct of petroleum refining, in the presence of a catalyst under carefully controlled heat and pressure

conditions. Propylene is an unsaturated hydrocarbon, containing only carbon and hydrogen atoms. Propylene is reacted with an organometallic, transition metal catalyst to provide a site for the reaction to occur, and propylene molecules are added sequentially through a reaction between the metallic functional group on the growing polymer chain and the unsaturated bond of the propylene monomer [1] (Figure 2.1.1):

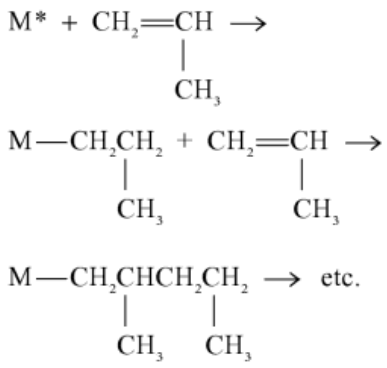

Figure 2.1.1: Polymerization reaction of propylene to form polypropylene.

When cooled to temperatures below the melting point, polypropylene molecules associate to form supramolecular structures. Polypropylene is a semicrystalline polymer; varying degrees of crystallinity and different types of crystal structures are possible, depending on the stereochemical structure, the processing or crystallization conditions, and the presence of additives.

Crystallinity arises from the stereoregularity in the molecular structure; occasional irregularities such as branching or tail-to-tail addition during polymerization or the presence of copolymers limit the extension of crystallization. Atactic polypropylene, with its random, irregular molecular structure, is predominantly amorphous. Semicrystalline polymers have high strength, stiffness, and density and sharp melting points. Amorphous polymers are tough and ductile, with higher impact strength, lower density, and lower haze. Properties of a polypropylene resin can be adjusted, depending on processing conditions and catalysts, by varying the level of crystallinity in the polymer.

The deformation mechanism of polypropylene is complex and composed by different phenomena [2, 3]. Initially, the increase in volume strain is less than expected, if only an elastic phenomenon (Poisson's ratio <0.5) was present, because of the presence of a strain induced reorganization of the amorphous phase in the interlamellar zones. At

higher strains tensile deformation includes straining of molecular chains in the interlamellar amorphous phase which is accompanied by lamellae separation, rotation of lamellar stacks, and interlamellar shear. In this phase the volume strain starts to increase significantly. At yield the crystalline order destruction begins and crystal spherulitic structure begins to transform into a fibrillar structure. Cavities may nucleate in the equatorial zones of spherulites, and void multiplication, growth and coalescence occur as micro-fibrillation takes place. At large strain cavitation is the main cause of dilatation. Polypropylene presents this crazelike phenomenon of deformation at temperatures higher than the glass transition temperature, however, this mechanism is observed only in the polar region of the α-phase spherulites of polypropylene (β- and γ- phases do not present this mechanism of deformation [4]).

2.1.2. Impact resistant polyolefinic copolymers

Impact resistant copolymers are constituted by a matrix and a dispersed phase. The matrix is made of polypropylene homopolymer or random copolymers while the dispersed phase can be synthetized by adding to the homopolymer matrix ethylene and propylene monomers, ethylene propylene and diene monomers or polyethylene. In the first case the dispersed phase, after the polymerization, will be constituted primary by EPR (ethylene-propylene rubber) while, in the second case, by EPDM. Comonomer levels in impact copolymers vary from 5% to 25% [1].

Due to the high level of co-monomer used in impact copolymers, the second phase is not miscible in the homopolymer matrix. Instead, it usually forms an amorphous elastomeric phase that is evenly distributed throughout the polypropylene semicrystalline matrix. The phase separation results in copolymer nodules distributed throughout the semicrystalline homopolymer matrix.

Impact (or block) copolymers are primarily used when increased impact resistance or toughness is required, especially at low temperatures. Impact resistance is dependent on the type, amount and morphology of the elastomeric phase, while the polypropylene matrix determines stiffness. The elastomeric nodules provide impact resistance by changing the deformation mechanisms and, thus, by increasing the energy absorption of the material.

The production process of the impact copolymers is the Spheripol process. In the Spheripol process, polymerization takes place in a loop reactor filled with liquid propylene. The three-component catalyst system, together with liquid propylene and any other comonomer for random copolymer or terpolymer production and hydrogen for molecular weight control are continuously fed into a loop reactor in which polymerization takes place at a temperature of 60-80°C and a pressure of 3.5-4 MPa [5] (Figure 2.1.2).

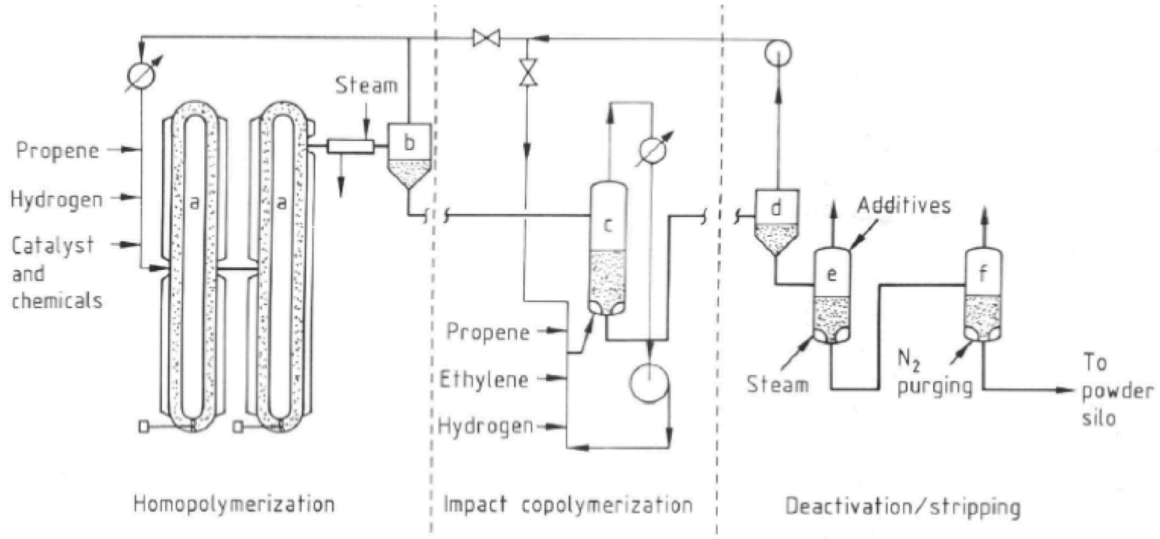

Figure 2.1.2: Scheme of the production process of polypropylene.

The process is composed by three different phases: the homopolymerization, the "impact copolymerization" and the phase of deactivation and stripping of the products. The homopolymerization is a continuous process and takes place in tube reactors in presence of hydrogen as a molecular weight moderator. In this phase the slurry of catalysts, monomers and polymers are pumped in the reactors. The second copolymerization phase takes place in a fluid reactor. In this phase the ethylene and propylene are inserted in the homopolymer thanks to the adsorption of the monomers in the gas phase. In this phase the reactors reach 70°C and pressure of 4 MPa. In the third phase the final product is treated with live stream to deactivate the catalyst and to complete removal of unreacted monomer. This is followed by removal of moisture in the polymer to the low parts-per-million range. The product is truly uniform because of the highly turbulent liquid flow conditions in the loop reactor result in a very homogeneous reaction mixture. Polymer particles as small as 0.3 mm or as large as 5 mm with identical

properties and morphologies can be produced with this process by the use of different catalyst.

To make heterophasic, high toughness copolymers in a liquid bulk process (like the Spheripol), the homopolymer or random copolymer particles exiting in the first reactor are fed to a gas phase reactor. The solid, porous polymer particle entering the gas phase reactor has the accessible polymerization active sites in the catalyst dispersed throughout it, allowing copolymerization of propylene and other olefinic monomers such as ethylene into a polymeric rubber. The rubber is heterophasically dispersed evenly in the solid polymer matrix, minimizing particle stickiness and fouling of the reactor. The addition of a second gas phase reactor allows the synthesis of a third polymeric phase, such as polyethylene, inside the heterophasic copolymer matrix particle exiting from the first gas phase reactor. Thus, a complicated multiphase polymer structure having a homopolymer, copolymer or terpolymer matrix, within which ethylene-propylene copolymer rubber and a polyethylene homopolymer are uniformly dispersed, can be produced directly in the reactor.

It is possible to produce copolymers with a content of EPR rubber of 40%. The resulting material is biphasic because of the thermodynamic immiscibility between the semicrystalline phase (isotactic propylene homopolymer) and the amorphous dispersed phase (inclusions of random ethylene-propylene copolymer). This process allows to obtain smaller inclusions with respect to the ones obtained by direct mixing of polypropylene and EPR rubber in an extruder.

In order to understand the deformation mechanisms of the ethylene-propylene block copolymers the microstructure of these materials will be presented.

Impact polypropylene copolymer mainly contains three “compositions”: ethylene-propylene random copolymer (EPR), a series of ethylene-propylene block copolymers with different sequence lengths (E*b*P) and propylene homopolymer. The latter “composition” constitutes the matrix of the material while the dispersed phase is composed of EPR and some ethylene-propylene block copolymer. A particle model with a core-shell structure has been proposed recently [6] in order to explain the microstructure of these materials. In this model EPR and the crystallizable polypropylene

segments in the block component forms the shell, and the crystallizable polyethylene segments are the major part of the core. A study on the chain structure of the ethylene-propylene block component has been presented recently [6-8] and the results suggested that these chains contain not only crystallizable polyethylene and polypropylene segments but also some ethylene-propylene random sequences. Four kinds of chain structures have been proposed: the first kind dominated by polypropylene segments (type I), the second one dominated by polyethylene segments (type II), the third one with equivalent polypropylene or polyethylene content (type III) and the last one which contain some ethylene-propylene random sequences (type IV) (Figure 2.1.3)

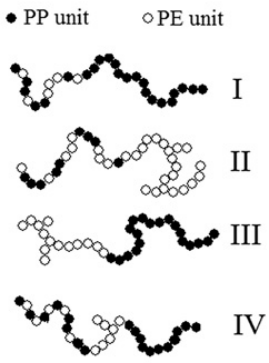

Figure 2.1.3: Kinds of chain structures proposed in order to describe the dispersed phase of ethylene-propylene block copolymers [6].

Figure 2.1.4 presents the core-shell structure phase model. As can be noticed the dispersed phase is composed of an ethylene-propylene block copolymer core and two layers: the inner layer is primary composed of EPR while the outer one of ethylene-propylene block copolymer. In particular, some block copolymer pass through the EPR layer forming some bridges connecting the core of the dispersed phase and the outer block copolymer layer. As can be seen in Figure 2.1.4 the block copolymer chains rich in polypropylene tend to locate in the interface layer between the polypropylene matrix and the dispersed phase, taking a role of compatibilizer. On the other hand the block copolymer chains rich in polyethylene tend to locate inside the EPR layer to form the polyethylene-rich core. The chains with equivalent PP or PE content are indeed block copolymer and may locate in the outer layer, in the core or even stay across the EPR shell to form the block copolymer bridges. Finally the type IV chains which contain some

ethylene-propylene random sequences may stay anywhere of ethylene-propylene block copolymer components.

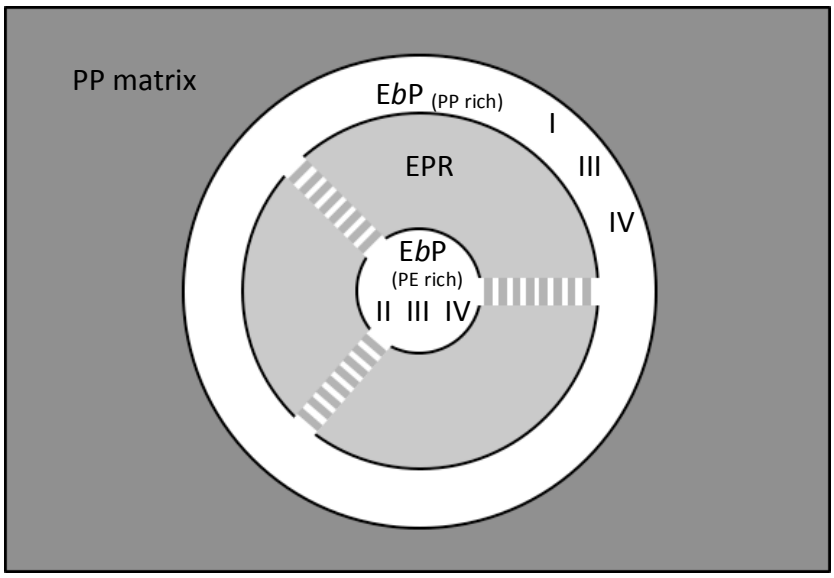

Figure 2.1.4: Scheme of the core-shell structure of the dispersed phase in ethylene-propylene block copolymer.

The deformation mechanism in ethylene-propylene block copolymers takes place in three steps [9-12] (Figure 2.1.5):

1. At first the inclusions act as stress concentrators because they have different stiffness with respect to the matrix. The stress concentration leads to the development of a triaxial stress in the particles and in the surrounding matrix.
2. The triaxial stress builds up inside particles and gives rise to void formation through cavitation inside particles (EPR shell) as well as detachment at the particle/matrix interface (Figure 2.1.6). With continuous growth of voids, simultaneously, shear bands start to form in the surrounding matrix.
3. Finally, at higher strain, cavitation process inside the particles leads up to a relaxation of the triaxial stress state. Thus, shear yielding is induced in the matrix and as a result plastic deformation of matrix is significantly enhanced.

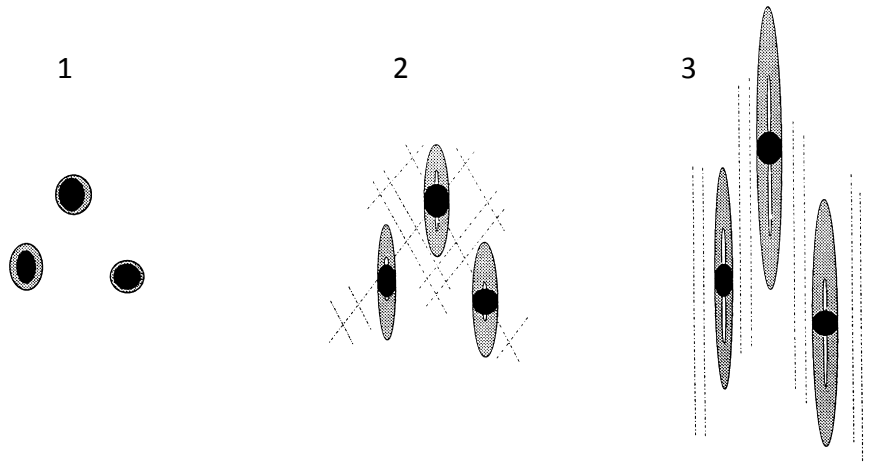

Figure 2.1.5: Scheme of the deformation process in ethylene-propylene block copolymer. Stress concentration (1), void formation (2), and cavitation in the inclusions and shear yielding in the matrix (3).

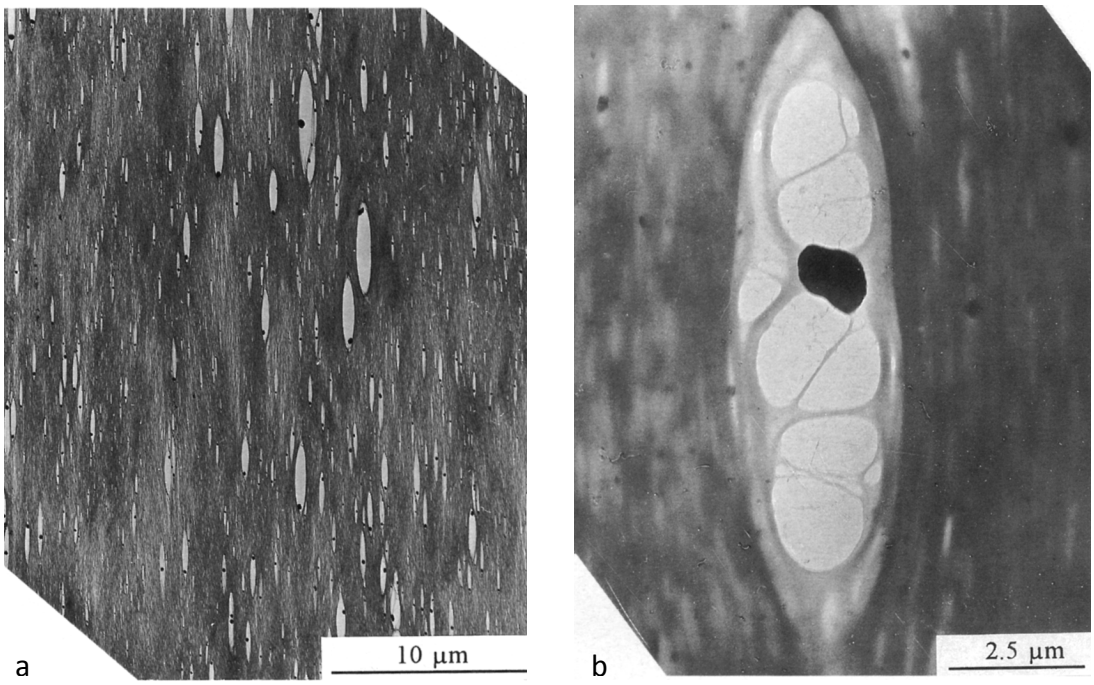

Figure 2.1.6: Image of the deformed inclusions in which cavitation phenomenon can be observed. Low magnification (a) and high magnification (b) [9].

2.2. True stress-strain

Typically, the tensile properties of polymers are analyzed in terms of engineering stress-strain curves. These curves are the classical tensile curves used for every kind of materials including polymers. However, recently [13-18], the study of the tensile properties beyond the elastic limit of polymers has been done analyzing the true stress-

true strain curve. This is principally due to the fact that the engineering stress-strain curve must be interpreted with caution beyond the elastic limit, since the specimen area experience substantial change from its original values. The true stress value is defined as:

$$\sigma_{true} = \frac{F}{A} \qquad (eq.\ 1)$$

Where F is the load and A is the current cross sectional area of the specimen whose value changes in time. Using the true stress rather than the engineering stress ($\sigma_{eng} = \frac{F}{A_0}$ (*eq. 2*), where A_0 is the initial cross sectional area) can give a more direct measure of the material response in the plastic flow range [19]. A measure of strain often used in conjunction with the true stress takes the increment of strain to be the incremental increase in displacement dL divided by the current length:

$$d\varepsilon_{true} = \frac{dL}{l} \rightarrow \varepsilon_{true} = \int_{l_0}^{L} \frac{1}{L} dL = ln \frac{L}{L_0} \qquad (eq.\ 3)$$

This strain is called the true or logarithmic strain or Hencky strain.

The typical engineering stress-strain curve for polymers is the one represented in Figure 2.2.1 and shows a maximum in load, which is commonly associated with the necking (a phenomenon of geometric instability occurring in uniaxial tension), a strain softening section in which there is a drop of the stress and, finally, a strain hardening section which leads up to the ductile fracture which is not observed in this particular case. Figure 2.2.1 also reports four images of the specimen during the test took in correspondence of the four red circles. The first photo on the left represents the end of the elastic zone and the beginning of the plastic one. The second photo was taken in the middle of the necking phenomenon; the third one when the neck starts to propagate and the final one when the neck was already propagated.

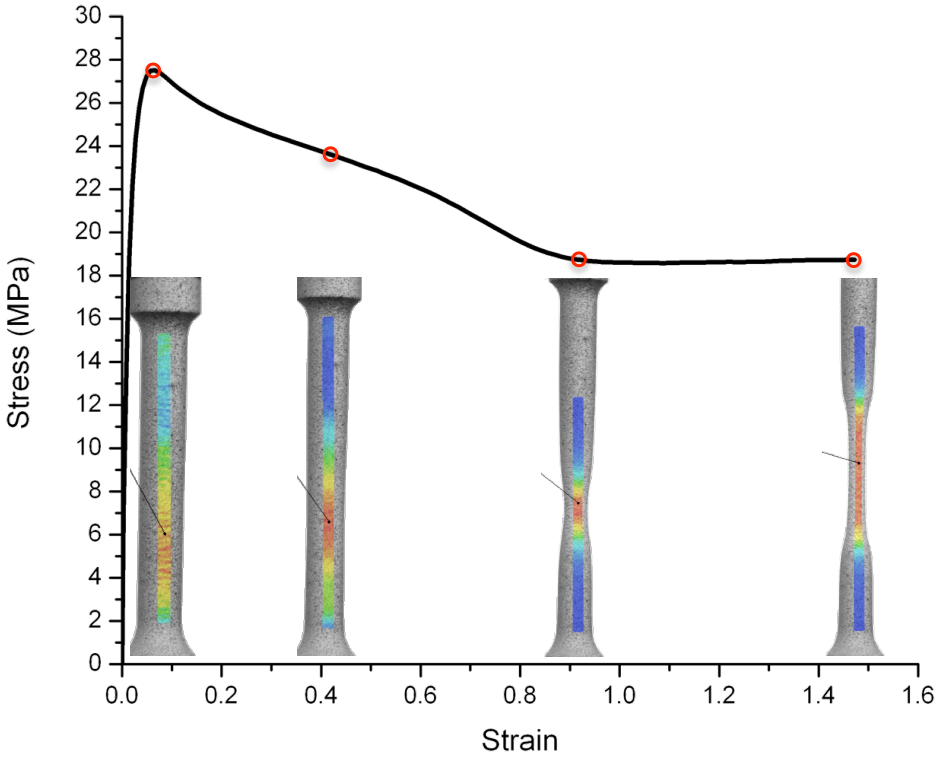

Figure 2.2.1: Engineering stress-strain curve with four images of the specimen during the test took in correspondence of the red circles.

Unlike the engineering stress-strain curve, the true stress-true strain curve represents a better way to describe the mechanical behavior of polymers (and materials in general). The true stress-true strain curve, of the same specimen whose standard stress-strain curve was presented in Figure 2.2.1, is reported in Figure 2.2.2. As can be seen, in the first region (before the elastic limit) the shape of the curve is almost the same of the engineering one because the cross-sectional area do not changes (there is no plastic deformation); in this case, the end of the elastic zone does not represent a maximum in the diagram because the curve keeps rising after this limit. After a brief section in which the value of the true stress is almost constant around 28-29 MPa, the slope of the curve begins to increase reaching the final true stress value of 95 MPa in which the test has been stopped. Thus, it is appropriate thinking that the failure true stress value will be higher than 100 MPa which is a value much higher than the maximum in the standard stress-strain diagram (Figure 2.2.1).

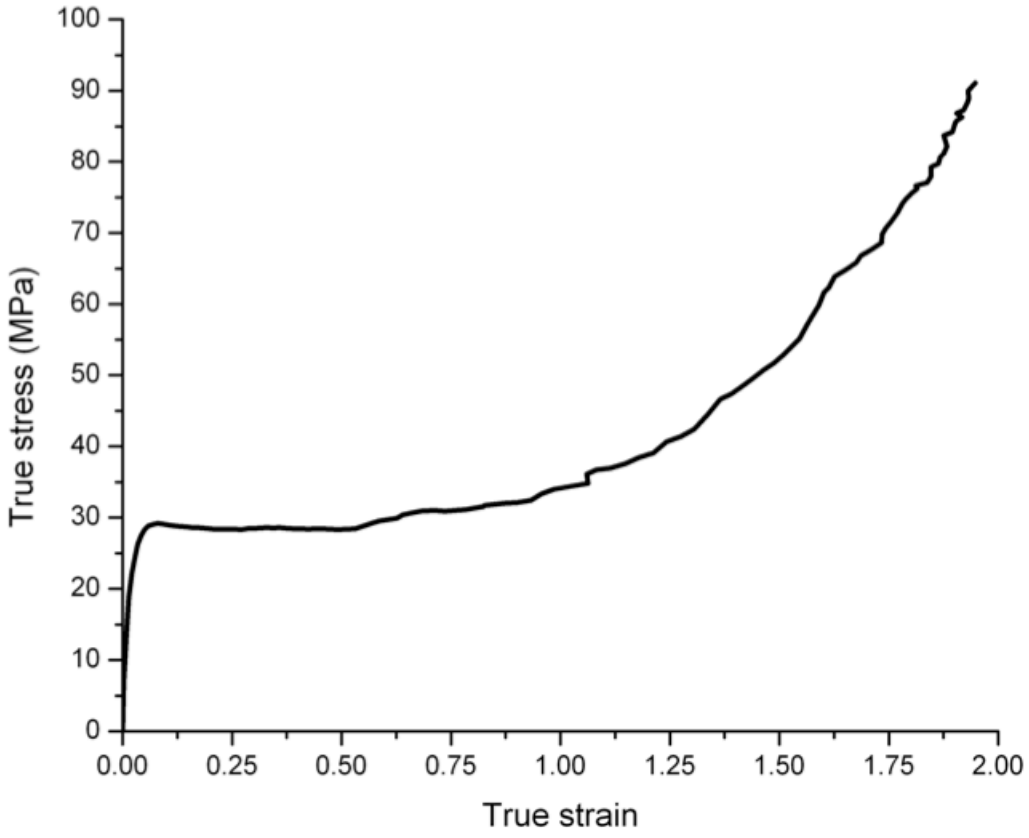

Figure 2.2.2: True stress-true strain curve of the same specimen as the engineering one presented in Figure 2.2.1.

2.3. Digital Image Correlation

Different video-based techniques have been used in many of the reported attempts to measure the true stress-true strain relation of polymers; following three different video-based techniques, three 2D *DIC* techniques and two 3D *DIC* techniques will be presented.

Video based techniques allow the measure of strain in a small (but not local) area of the surface of the specimen, while *DIC* techniques allows the local measure of strain on the surface of the specimen. There are some differences between the 2D *DIC* and the 3D *DIC* technique. Firstly, in the 2D *DIC* the surface of the specimen is seen as the projected image of the real surface. This fact can distort the dimensions of the surface and also the value of the strains measured on the projected surface. This is particularly true in case of highly deformable materials which show a marked necking phenomenon or in those cases in which the geometry of the specimen promotes large thickness reduction (like the one used in this thesis work). Secondly, 3D *DIC* systems require a system calibration

for both strain and displacement calculations unlike 2D *DIC* systems which do not require any calibration for strain calculations. The calibration, as will be explained in paragraph 3.2.1, was run before each experiment to ensure accurate results.

Finally, in the 3D *DIC* systems, like in the case of the 2D *DIC* techniques, there is no way to determine the local stress (while the local strain can be measured). Therefore an average (macroscopic) Cauchy stress for the whole cross section must be calculates from the total load and the current cross-sectional area.

2.3.1. Video based techniques

G'Sell method

G'Sell et al. [13, 14] developed an optical technique where seven dots on one side of a rectangular bar were tracked. In order to localize the strains, they introduced a slight reduction of the cross sectional area in the zone where the markers were applied. The displacement of these dots was used to calculate the true axial and transverse strains. True stress was calculated using the measured transverse strain and assuming transverse isotropy. In this way they omitted the assumption of constant volume.

Thanks to this technique, which is capable of assessing volume changes in real time during the deformation of polymers, they have analyzed the influence of damage mechanisms in a glassy polymer and a polymeric blend. This technique constitutes a new version of the VideoTraction system (Apollor, Vandoeuvre, France). By contrast to the previous version of the system, which was limited to materials deforming homogeneously, the present device is now applicable to materials that exhibit diffuse necking during a tensile test. This type of plastic instability corresponds to the symmetrical reduction of the cross-section caused by the concentration of tensile deformation in a given portion of the specimen.

The technique consists in printing seven ink markers on the front surface prior to deformation and analyzing them during the tensile test in order to locally characterize the plastic behavior. The markers are black, nearly round, with a diameter of about 0.4 mm (Figure 2.3.1).

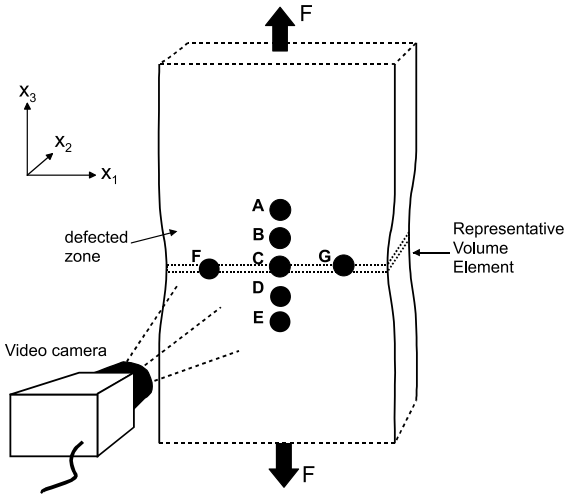

Figure 2.3.1: Scheme of the technique adopted by G'Sell et al. [13].

The five markers (A, B, C, D, and E) are aligned along the tensile axis x_3 and the distance between the centers of successive markers is equal to about 1mm. The other two markers, together with the C marker, aligned along the transversal axis x_1 are more widely separated, in such a way that they occupy a large fraction of the total width in the wasted zone. The aim of this method is to determine the three principal components of strain ε_1, ε_2 and ε_3 in a proper representative volume element (RVE) of the material where the stresses and strains should be nearly uniform. This RVE is defined as the volume delimited by the centers of the F, C and G markers, which are not perfectly aligned.

Considering the axial strain distribution, for every pairs of the markers AB, BC, CD and DE the axial true strain has been defined as following:

- $\varepsilon_3\,(AB) = \ln\left(\frac{AB_3}{AB_{30}}\right)$ (*eq. 4*)
- $\varepsilon_3\,(BC) = \ln\left(\frac{BC_3}{BC_{30}}\right)$
- $\varepsilon_3\,(CD) = \ln\left(\frac{CD_3}{CD_{30}}\right)$
- $\varepsilon_3\,(DE) = \ln\left(\frac{DE_3}{DE_{30}}\right)$

Where AB_{30}, BC_{30}, CD_{30}, DE_{30} and AB_3, BC_3, CD_3, DE_3 are the initial and current distances (along x_3) of the centers of gravity of the two markers in the pairs. As showing in Figure 2.3.2, in a practical case of a PET sample, the axial true strain ε_3 at the level of the RVE

can be obtained by non-linear interpolation from the four values of the axial strain along the axis.

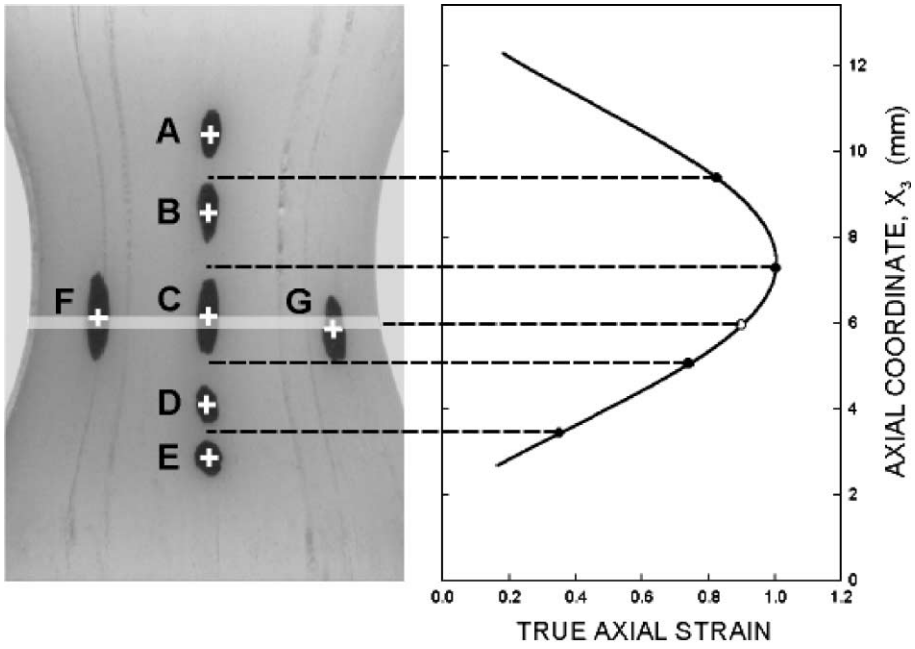

Figure 2.3.2: Calculation of the axial true strain by non-linear interpolation of the values of the axial strain [13].

The second step of this method concern the transversal true strain ε_1 in the RVE, which is obtained from the marker F and G with the same Hencky approach by the relation:

$$\varepsilon_1 = \ln\left(\frac{FG_1}{FG_{10}}\right) \qquad (eq.\ 5)$$

Where FG_{10} and FG_1 are the initial and current distances (along x_1) of the centers of gravity of the two markers in the FG pair.

As for the second transversal strain ε_2 it is simply taken equal to ε_1 by assuming that the strain tensor is transversally isotropic. This involves that the original microstructure of the material is isotropic and that no artifact should favor deformation along one of the two directions x_1 and x_2. This situation could arise for example if the specimen is too wide along x_1 with respect to the thickness along x_2. The loading path would then approach the plane strain tension case for which it is well known that the sample deforms more through the thickness.

Finally, since the three components of strain are defined in the same RVE, the trace of the strain tensor can be calculated. It is called volume strain since it measures the dilatation (or contraction) of the RVE. The volume strain is calculated as follow:

$$\varepsilon_v = \varepsilon_1 + \varepsilon_2 + \varepsilon_3 = \ln\left(\frac{V}{V_0}\right) \qquad (eq.\ 6)$$

The appropriate stress definition associated with the Hencky strain is the Cauchy stress (often called true stress). This stress takes into account the reduction of the cross-sectional area undergone by the specimen while it is stretched. In his work, G'Sell, used the following expression to calculate the true stress:

$$\sigma_3 = \frac{F}{A_0 * \exp\left(\varepsilon_1 + \varepsilon_2\right)} \qquad (eq.\ 7)$$

Where F is the load registered by the traction machine, A_0 is the initial cross-sectional area of the specimen and ε_1 and ε_2 are the two transversal strains. In this way the approximation that the two strains are identical persist in the true stress calculation. This is due to the fact that the cross-sectional area cannot be calculated more precisely in a different way because of the geometry of the specimen.

Figure 2.3.3 illustrates the main features of the VideoTraction system: the one used by G'Sell. Particularly its three interfaces can be noticed:

- The video camera
- The load cell
- The servohydraulic actuator of the tensile testing machine (MTS 810)

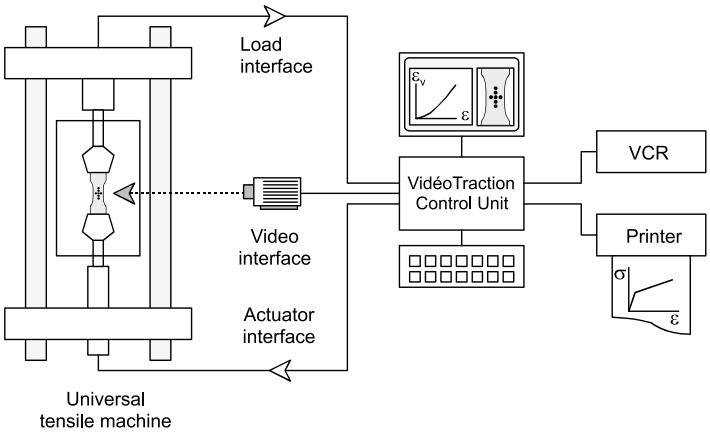

Figure 2.3.3: Scheme of the VideoTraction system.

The first interface acquires the centers of gravity of the seven markers with a frequency of about 30 frame/s, from which it determines the true axial strain ε_3 and the volume strain ε_v. The second interface gives access at the same frequency to the true stress σ_3. The latter interface adjusts continuously the speed of the actuator in such a way that the axial true strain rate, $\dot{\varepsilon} = \frac{d\varepsilon_3}{dt}$ (*eq. 8*), is kept constant during the test.

Mohanraj method

Mohanraj et al [15] used the same G'Sell technique previously explained with a smaller reduction of the cross sectional area of the specimen. In fact the tensile specimens were machined from the compression molded plates with a numerically driven milling machine in order to define a calibrated zone of dimensions 50x10x4 mm^3. In order to force the onset of necking in the central part of the specimen, the width of the samples was locally reduced by 10% with curvature of about 20 mm. The goal of this specimen design is to determine the plastic behavior of the polymer in the representative volume element (RVE) made up of the material slice at the narrowest cross-section, where the strain rate is maximum before and after the initiation of necking.

The principle of this method is the same as the G'Sell method and consists in analyzing in real time, via a computerized vision system, the coordinates (x_1 and x_3) of seven markers printed prior to the test on the front face of the specimens.

Gloaguen and Lefebvre method

The experimental set-up proposed by Gloaguen and Lefebvre [20, 21] has been designed with the aim to offer the most versatile capabilities regarding temperature and strain ranges, and also to avoid the drawbacks of mechanical extensometers which include range limitations, gauge slippage and potential damage initiation on the sample surface at the point of gauge clamping in some cases. This optical system is based on the previously described computer-aided video-controlled tensile testing equipment developed by G'Sell and coworkers, but this procedure did not require any assumption of constant volume or transversal isotropy.

The geometry of the sample used by Gloaguen and Lefebvre is almost the same of the one used by G'Sell. The geometry is still parallelepiped but the specimens have been machined with thickness ranging between 2 and 4 mm (Figure 2.3.4). Instead of using a standard tensile specimen with constant cross-section, they adopted this flat "hour-glass" profile in the central part in order to ensure strain localization while the fairly large radius of curvature minimizes stress heterogeneities. In such a way, stress is maximum in the central part of the sample and plastic deformation always initiates in this area.

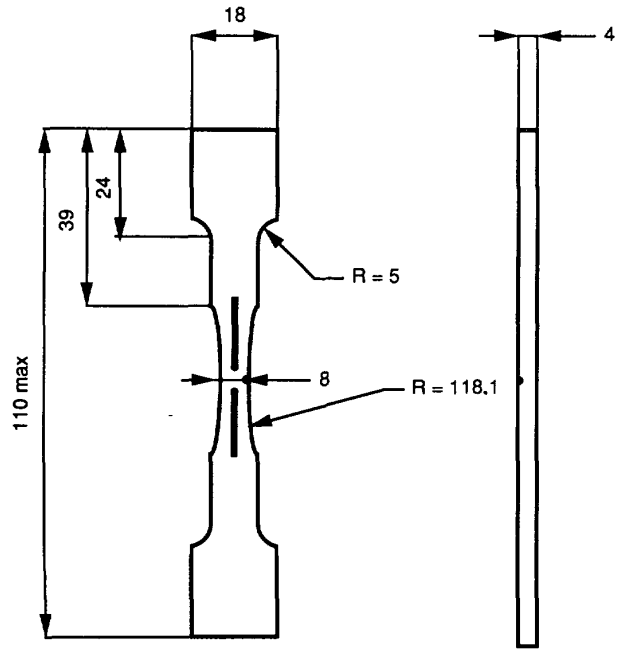

Figure 2.3.4: Geometry of the specimen used by Gloaguen and Lefebvre [21].

As can be noticed in Figure 2.3.4 two adjacent sides of the specimen receive a special treatment in order to make it suitable for optical extensometry. Both surfaces are

covered with a white paint film capable of withstanding the applied deformation without breaking. An optical target is then drawn on the sample. It consists of two vertical black lines aligned along the sample elongation axis on the front surface and of a black dot slightly spread on both surfaces.

The experimental set-up (Figure 2.3.5) for the determination of sample strains is composed of the following elements:

- Two CCD video cameras equipped with zoom lenses mounted on bellows in order to ensure proper focus on the sample surfaces in all experimental configurations. The first camera points at the front surface while the second one records the sample thickness on the lateral surface.
- A digitizing and image processing unit which includes:
    - A microcomputer
    - A video interface board installed in the central unit of the computer
    - Three video monitors, of which two are devoted to the display of analogic images and the third to the processed ones.

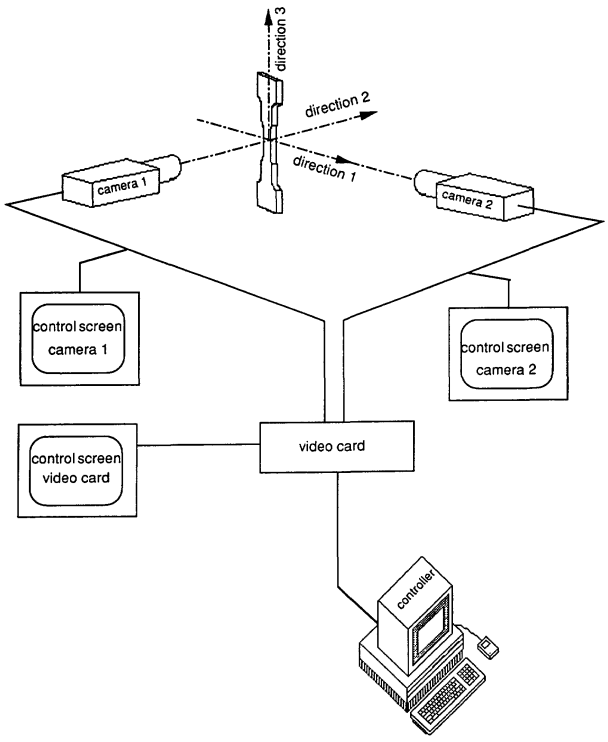

Figure 2.3.5: Experimental set-up used by Gloaguen and Lefebvre to determinate the sample strain [21].

When the picture is digitized, a number taken between 0 and 255 is attributed to each pixel. It corresponds to a particular grey level on a grey scale ranging from 0 for a black element of the picture to 255 for a white one. The following step consists in the definition of a threshold value. The picture is then processed in the following way: any pixel for which the initial grey level is below the threshold will be assigned to level 0 and in the same way a pixel with a grey level above the threshold is brought up to level 255. In this way the processed pictures visualized on the monitor are of the binary type, each pixel appearing black of white.

The sample appears as a white shape on a black background, and the drawings of the target are clearly localized as illustrated in Figure 2.3.6. The images are transmitted to the computer central unit in the form of arrays. The routine has been designed in order to be able to find the location of the lines and columns, which contains the minimum number of pixels of a given type, and also to count that number of pixels. At any time during the experiment, these numbers represent the width, thickness and longitudinal distance between the two black lines of the target.

Figure 2.3.6: processed images of the two faces of the specimen [21].

As the tensile test proceeds, the computer computes the strain as the ratio of these data at time t to the initial set of measurements at the beginning of the experiment:

$$\varepsilon_l = \frac{(n_{l,t} - n_{l,o})}{n_{l,0}} \qquad (eq.\ 9)$$

Where ε_l is the deformation along the direction *l* at the time *t* and $n_{l,t}$, $n_{l,0}$ are the number of pixels measured along the direction *l* at time *t* and *t=0* respectively. Once the

deformations are known in the three principal directions, the local strain volume can be computed.

In the mean time, the computer program records the applied load on the sample and by combining the load and strains data the true stress can be calculate in the same way as G'Sell did in his work as follows:

$$\sigma_a = \frac{F}{[S_0(1+\varepsilon_2)(1+\varepsilon_3)]} \qquad (eq.\ 10)$$

Where S_0 is the initial section of the sample and ε_2 and ε_3 are the strains respectively in the direction 2 and 3.

2.3.2. 2D Digital Image Correlation methods

All of the previously mentioned methods show a relatively poor spatial resolution. Digital image correlation (DIC) has improved spatial resolution of optical full-field strain measurement. Some DIC approaches have been developed recently to measure the strain field of a tensile test specimen. Most of them used only one camera while some used two cameras.

For example Parsons et al. [22, 23] did not assume that the specimen would deform isotropically in the two lateral directions. Therefore, as shown in Figure 2.3.7, the tests were viewed from two orientations: the front view captured the deformation of the thick lateral dimension and the side view captured the deformation of the thin lateral dimension. The two views were recorded simultaneously in the same image utilizing a right-angle prism (Figure 2.3.8). In such way they obtained the strain field on two sides of a rectangular tensile specimens using only one camera.

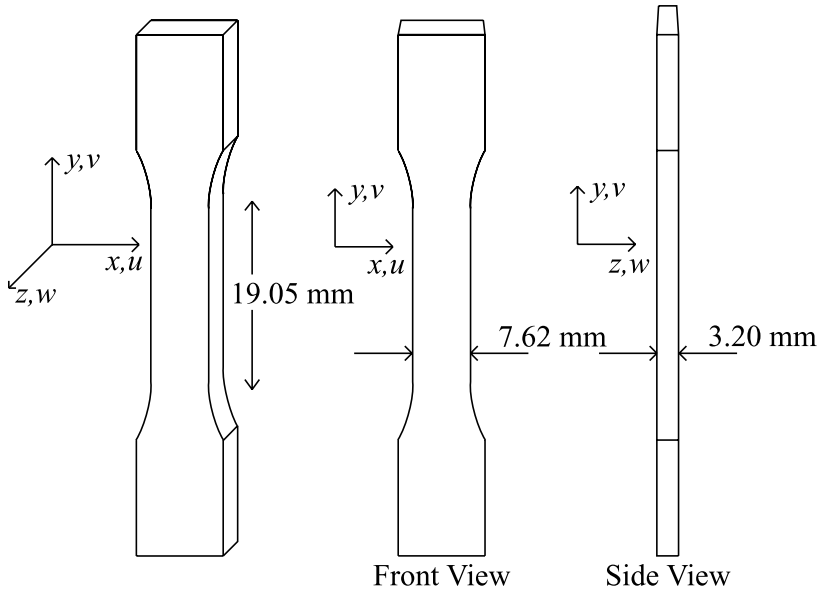

Figure 2.3.7: Geometry and views of the specimen used by Parsons et al. [23].

The camera captured the front view of the specimen directly. The right-angle prism reflected light from the side view 90°, allowing both views to appear in the same image. As shown in Figure 2.3.8 the prism is positioned at the right of the specimen in a fixed position.

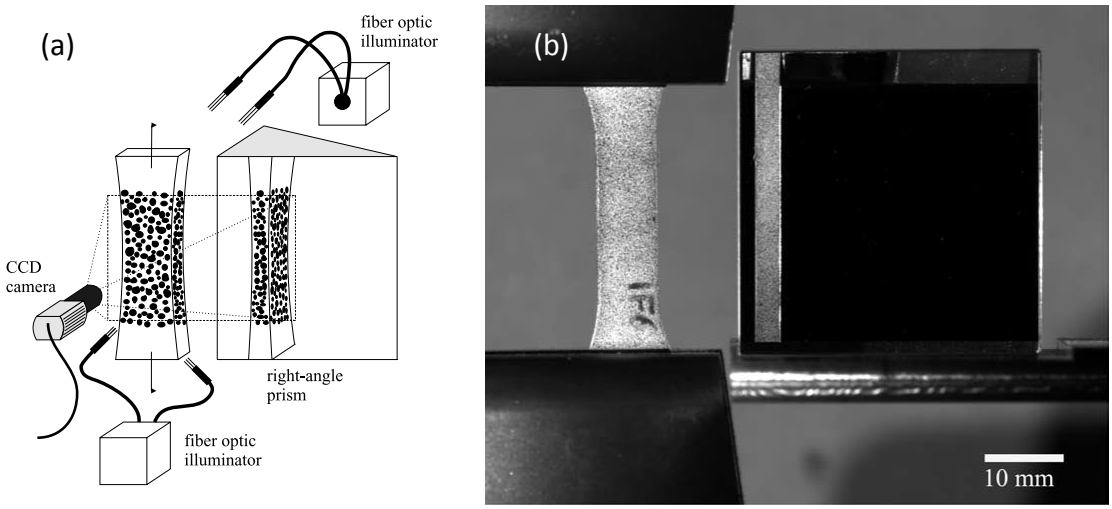

Figure 2.3.8: Scheme (a) and photo (b) of the position of the right angle prism in the experimental test of Parsons [23].

Displacements and strains were evaluated at individual points on the surface of the specimen. Within the neck, the axial strain henceforth varies with axial position on the specimen, and, with the displacement gradient no longer constant, the concept of a gage

length becomes obsolete. Digital image correlation was thus used to measure directly the pointwise displacements and displacements gradients. Local axial, lateral and volumetric strains were calculated from the displacement gradients. Full-field contours were constructed in a two steps process from the local displacements.

The images were analyzed with a DIC algorithm; to correlate the reference image to the deformed images the area of interest in the reference image is divided into small square subsets. The discrete matrix of the pixel gray level values in each subset forms a unique pattern within the image.

Local lateral, axial and volumetric strains were calculated directly from the derivatives of the second order functions, which map the positions within the reference subset to positions within each deformed image.

With displacement and strain data available everywhere on the two visible sides of the specimen, strain can be studied simultaneously as a function of both position and time. Plotting strain contours (Figure 2.3.9) over the course of a tensile test illustrates clearly the localization process and allows ready comparison between different materials.

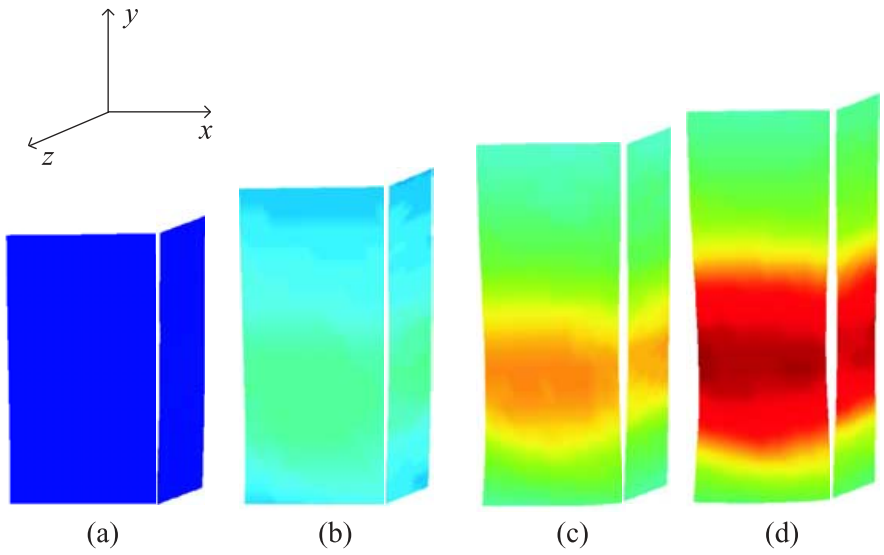

Figure 2.3.9: Strain contours in the two faces of the specimen during a tensile test in Parsons's work [23].

Another example of 2D DIC technique is the work of De Almeida et al. [16]. In order to determine full-field displacement on both front and lateral sides of the specimen, the tensile specimens have been previously covered with a random speckle pattern realized

by spraying white and black powders on both sides of the specimens. This technique leads to a white and black random grain field. A mirror bounded up with the device has been positioned to reflect the lateral pattern of the specimen to the CCD camera (Figure 2.3.10). The short distance between the camera and the specimen led to two different focus positions to get contrasted images of front and lateral patterns of the specimen. To bypass that difficulty, the focus distance of the camera has been adjusted using a micrometer translator without changing camera lens parameters. The scale of the lateral pattern image is then slightly greater than the front pattern image one.

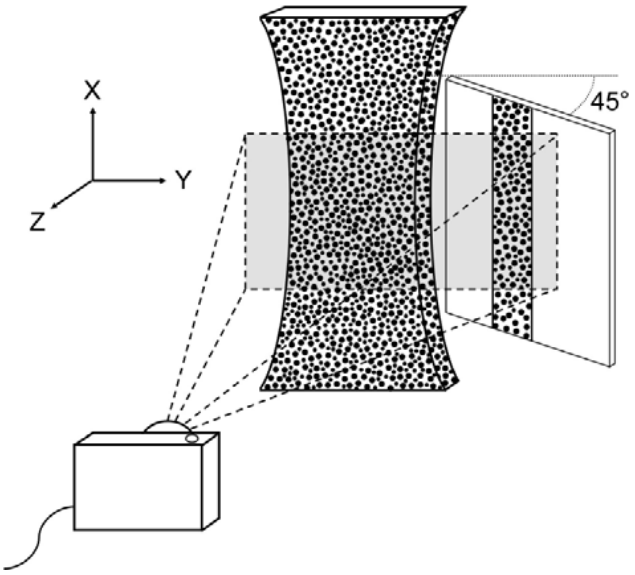

Figure 2.3.10: Scheme of the experimental test of De Almeida et al.; the 45° inclined mirror can be noticed [16].

Finally Fang et al. [17, 24] used two cameras watching one side each. The preparation of the specimen for the test is the same used in the previously explained techniques: the surfaces of the specimen were covered with a random speckle pattern. Differently from the firsts techniques, in this case, the random speckle pattern presents three different colors: black, blue and red. This was done to give a better characterization of the specimen surfaces. The geometry of the specimen is the one according to the ASTM D-638 standard test method and it is shown in Figure 2.3.11. To ensure each specimen necking within the gage length, thickness near the center of the specimen was reduced by 0.1 mm with fine sand paper.

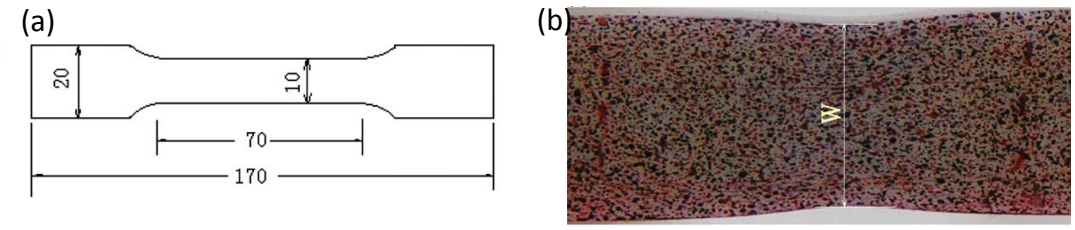

Figure 2.3.11: Geometry of the specimen (a) used by Fang et al. and (b) image of the random speckle 3-color pattern [24].

The three dimensional deformations in the axial, width and thickness directions were recorded through two high resolution cameras each one watching a different surface of the specimen as can be seen in Figure 2.3.12.

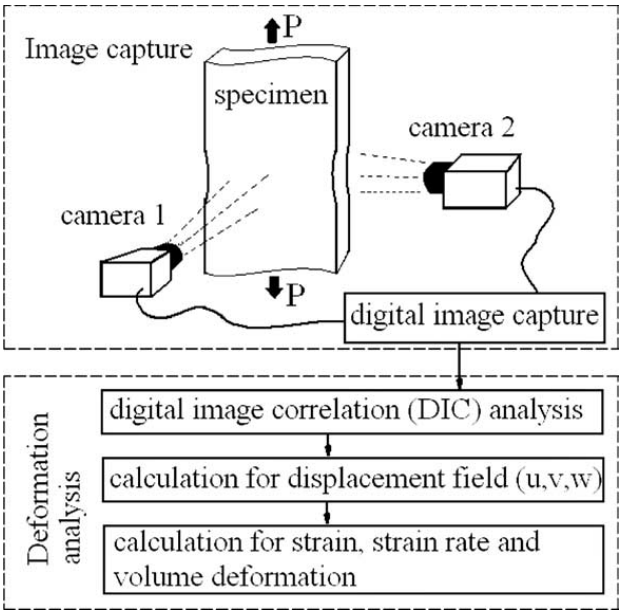

Figure 2.3.12: Scheme of the equipment used by Fang et al. [24].

In all the three methods presented above isochoric or isotropic assumptions are not needed. However, all the methods mentioned are based on the assumption that the strains measured on the surface of the specimen are representative of the strains throughout the thickness of the specimen, i.e. the reduction of width measured on the front surface is representative for the width reduction throughout the thickness.

The same assumption has to be done in the case of a 3D DIC technique because the limit of an optical system is that it record and analyze the deformation on the surface but it can show nothing about what happen in the bulk of the material. Although, 3D DIC

techniques allows a better measurement of strain gradients on the surface of the specimen with respect to the 2D DIC techniques because, as previously explained, they do not see the surface like a projection on a plane an so they can be used in case of specimens which presents large plastic deformations and thickness reduction during the tensile test. This is particularly important in the study of the behavior of ductile thermoplastic materials like the ones studied in this thesis work.

Some 3D DIC techniques have been developed in the last years and some of them will be reported subsequently.

2.3.3. 3D Digital Image Correlation methods

Grytten method [18]

In this method the cameras were mounted on a tripod and arranged so that two adjacent faces of the specimen were visible to both cameras simultaneously as illustrated in Figure 2.3.13.

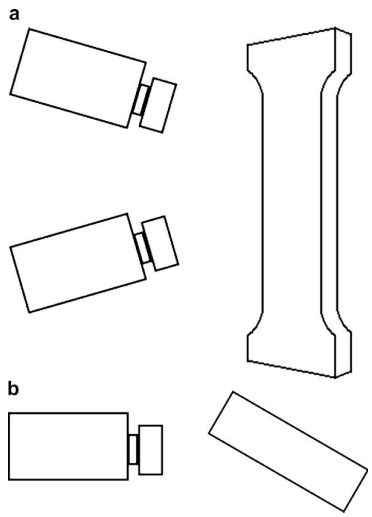

Figure 2.3.13: Scheme of the camera positioning adopted by Grytten [18].

This arrangement of the cameras allows measurement of out-of-plane displacement in addition to in-plane strains on the specimen surface. However, it results in a slightly lower spatial resolution in the transverse direction than in the longitudinal direction due to the acute angle between the optical axis and the surfaces. Further, cross sections in the specimen will in general not be aligned with rows of pixels in the captured images (Figure 2.3.14). Thus, points in a certain cross section have to be identified based on their

3D coordinate in the object coordinate system and not based on the pixel coordinates in the image coordinate system. These points are required to calculate the current cross sectional area and the true stress.

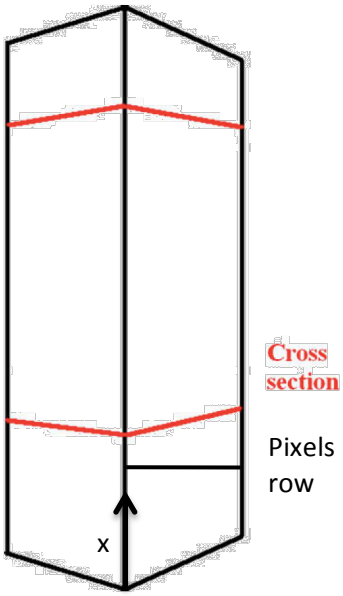

Figure 2.3.14: Alignment of cross sections and pixel rows as seen in the images [18].

The data exported was ordered by pixel coordinates but, as shown in Figure 2.3.14, it is impossible to align all cross sections of the sample with rows of pixels. Therefore, pixels within the same cross section first had to be identified. This was done by searching for all pixels with a certain x-coordinate ±0.5 mm (according to the coordinate system shown in Figure 2.3.14). The average logarithmic strain in the longitudinal direction in any cross section can be calculated from the average Green-Lagrange strain as:

$$\varepsilon_{xx} = \frac{1}{2}\ln(1 + 2\bar{E}_{xx}) \qquad (eq.\ 11)$$

Assuming that the transverse strains measured on the surface are representative of the strains throughout the cross section, the macroscopic Cauchy stress in the longitudinal direction can be calculated in any cross section as:

$$\sigma_{xx} = \frac{F}{A} = \frac{F}{A}\frac{A_0}{A} = \frac{F}{A_0}\frac{w_0}{w}\frac{t_0}{t} = \frac{F}{A_0}\frac{1}{\sqrt{1+2\bar{E}_{yy}}\sqrt{1+2\bar{E}_{zz}}} \qquad (eq.\ 12)$$

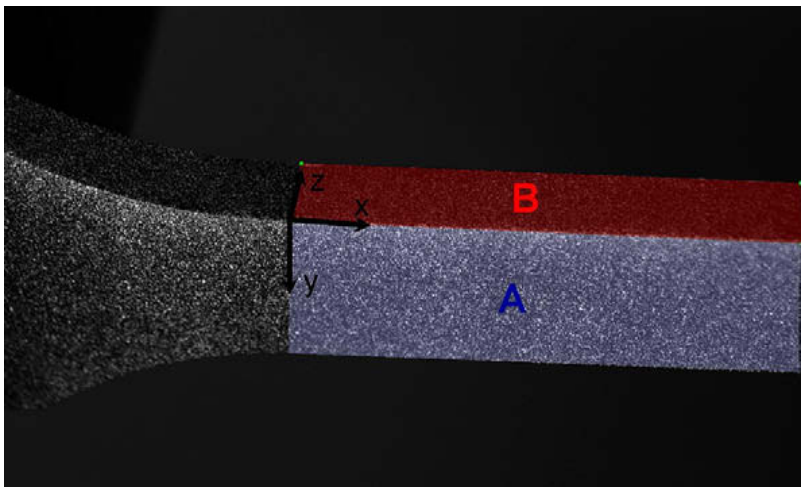

Figure 2.3.15: Image of the specimen during the test; the two faces, A and B, are highlighted [18].

Where σ_{xx} is the Cauchy stress, F is the current force, A and A_0 are the current and initial cross sectional area, w and w_0 are the current and initial width, t and t_0 are the current and initial thickness and $\bar{E}_{yy}$ and $\bar{E}_{zz}$ are the average Green-Lagrange strain in the transverse directions for all points in the current cross section on face A and B respectively (Figure 2.3.15).

As an alternative to using the transverse strains measured on the two faces, the average normal displacement of the two faces can be used to calculate the Cauchy stress as:

$$\sigma_{xx} = \frac{F}{A} = \frac{F}{(w_0 - 2\bar{V})(t_0 - 2\bar{W})} \qquad (eq.\ 13)$$

Where $\bar{V}$ in the average normal displacement of points in the current cross section on face B and $\bar{W}$ is the average normal displacement of points on surface A.

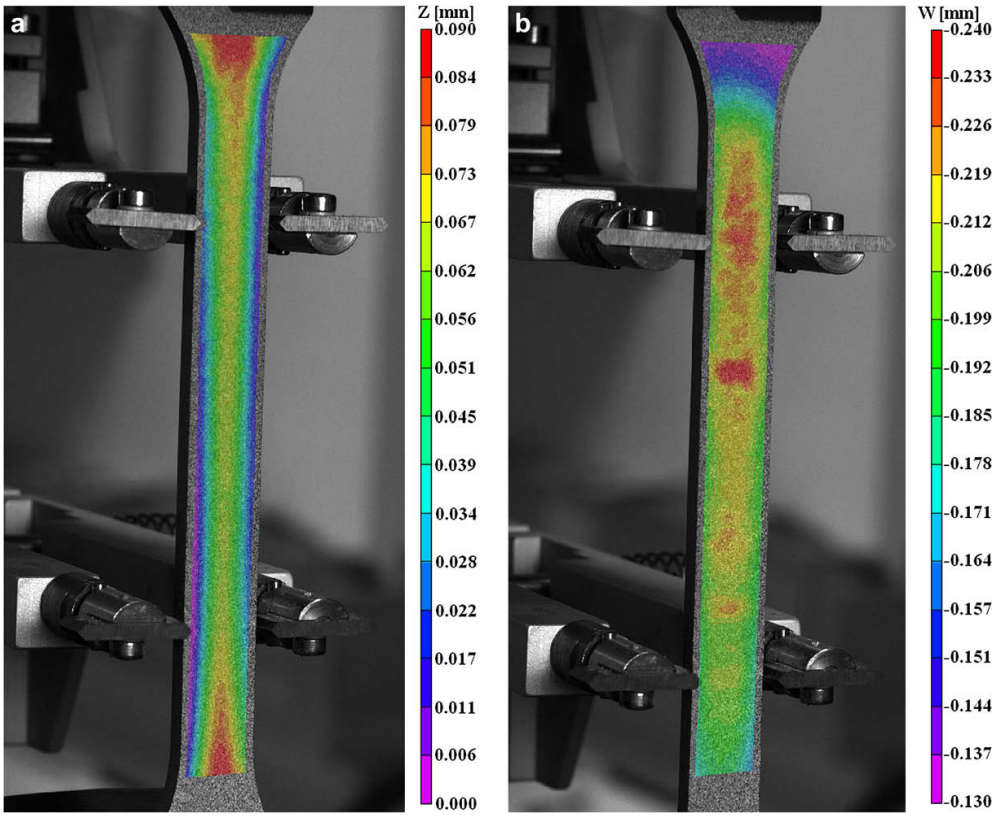

Figure 2.3.16: Analyzed images with strain distribution [18].

Jerabek method [25]

The principal difference between this technique and the Grytten's technique is that in this case the surface of the specimen is parallel to the cameras. In this way only the front surface can be seen and analyzed (Figure 2.3.17).

All the preparation steps used by Jerabek are the same of the previously mentioned technique and the one used in this thesis work. The specimen needs to be covered with a random speckle pattern. This pattern was produced by a black graphite spray so that the specimens were homogeneously covered with densely yet distinctly spaced graphite. A system calibration is needed in order to allow the strain field determination.

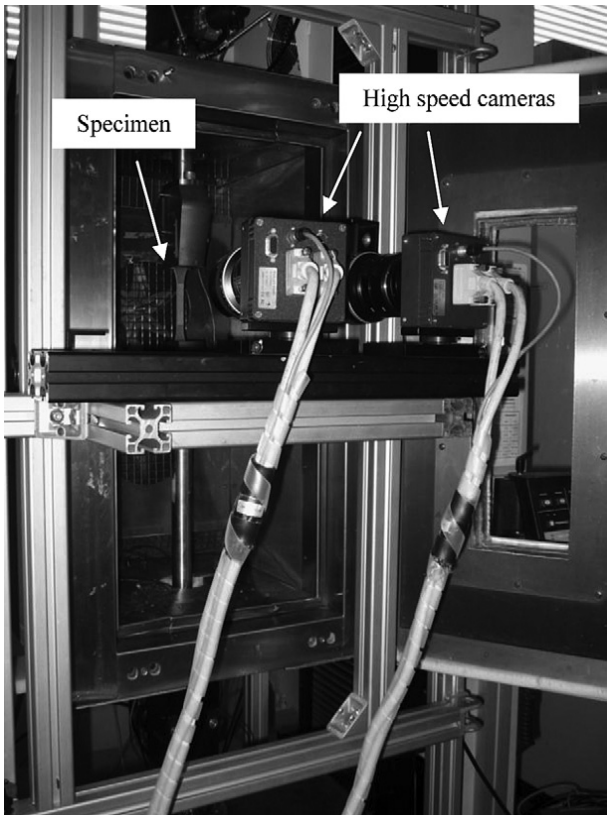

Figure 2.3.17: Equipment and set up of the cameras used by Jerabek during his tests [25].

Chapter 3. Experimental details

3.1. Materials and specimens

3.1.1. Materials

The materials analyzed in this work are five grade of polypropylene produced and commercialized by Repsol: one homopolymer and four propylene-ethylene block copolymers. The copolymers differ from each other in the content of polyethylene and/or for the molecular weight. The commercial names (with which the materials will be called henceforward) of the copolymers are: PB 110, PB 150, PB 170 and PB 171, while the homopolymer is the PP 060.

Table 3.1.1 collects the main characteristics of these materials [26]:

Materials	RMN		GPC			
	Ethylene content	Iso-tacticity index	Mn	Mw	Mz	Polydispersity (Mw/Mn)
PP 060	0 %	97.4	53000	396000	1250000	7.48
PB 110	6.9 %	83.3	160000	816000	2250000	5.09
PB 150	8.5 %	85.4	66000	353000	1030000	5.37
PB 170	8.5 %	84.2	56000	302000	880000	5.39
PB 171	11.2 %	81	61000	307000	880000	5.05

Table 3.1.1: Characteristics of the materials analyzed in this thesis work.

As can be seen in Table 3.1.1 the homopolymer PP 060 is the material that presents the highest polydispersity index (7.48).

Among the copolymers the one with the highest ethylene content is the PB 171 with a value of 11.2% while the PB 110 presents the lowest value (6.9%); the two copolymers PB 150 and PB 170 are very similar concerning the ethylene content (8.5%) but differ one from the other for the molecular weight, which is higher in the PB 150. This fact is very

important because comparing the results of these two materials can give us an idea of the influence of the molecular weight in the properties of the materials.

The PB 171, however, has a molecular weight value that is intermediate between the ones of the PB 150 and the PB 170, but presents an ethylene content a lot higher (11,2%). Comparing the results of this material with the results of the two copolymers previously mentioned would give an idea of the dependence of their properties from the content of polyethylene.

Finally, the PB 110 presents a content of polyethylene lower than the other copolymers and a higher molecular weight.

3.1.2. Injection molding

All the five materials were received in form of pellets and have been transformed into tests specimens by injection molding.

The injection molding process is a cyclic process of transformation of polymers. It allows producing polymer object with complex geometry in a very small time. The process consists in the injection of fluid polymer in the cavity of the mold, the freezing of the mold and the extraction of the finished part.

There are three principal parts that compose the injection molding machine (Figure 3.1.1):

- Injection group
- Mold
- Clamping unit

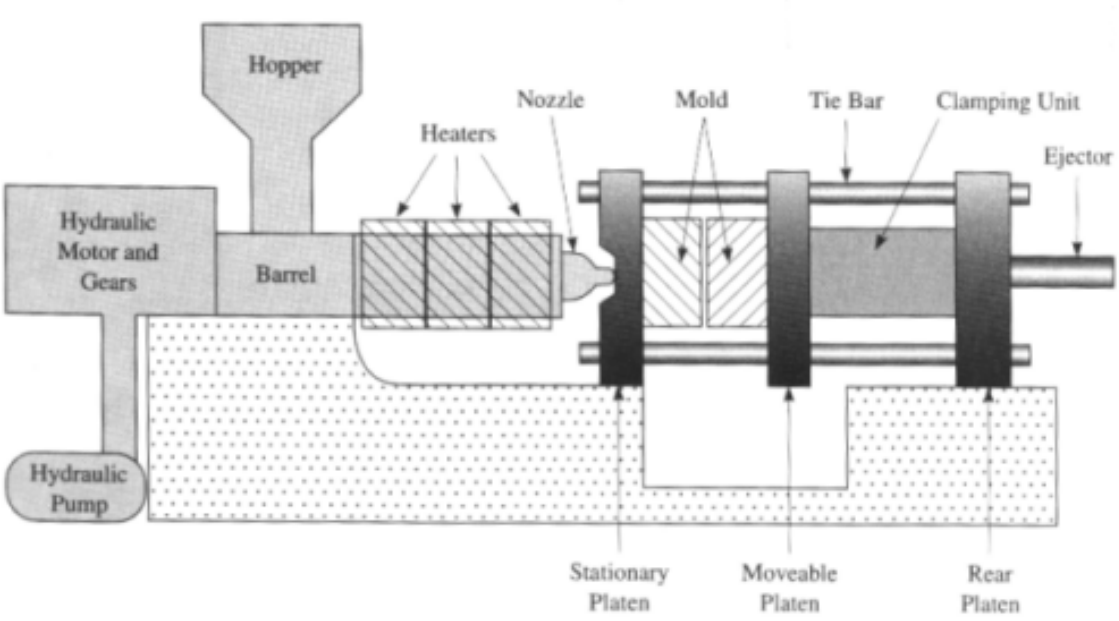

Figure 3.1.1: Scheme of an injection molding machine; the three principal parts can be noticed: the injection group on the left, the mold in the center and the clamping unit on the right.

The phases of the injection process are:

1. Closing the mold;
2. Injection of the material: the injection group advances until it reaches the mold. The screw applies a pressure at the fluid polymer, which flows inside the cavity of the close mold.
3. Pressure maintenance: the screw of the cylinder applies a post-pressure at the fluid polymer. This action improves the filling avoiding defects on the final piece.
4. Plasticization: in this phase the screw inside the cylinder starts to thin the material receding.
5. Opening of the mold and extraction of the piece already freeze.

The injection process has been realized with a machine Engel Victory 110.

3.1.3. Characteristics of the specimens

From the molded part the specimen used in this thesis work were obtained (Figure 3.1.2).

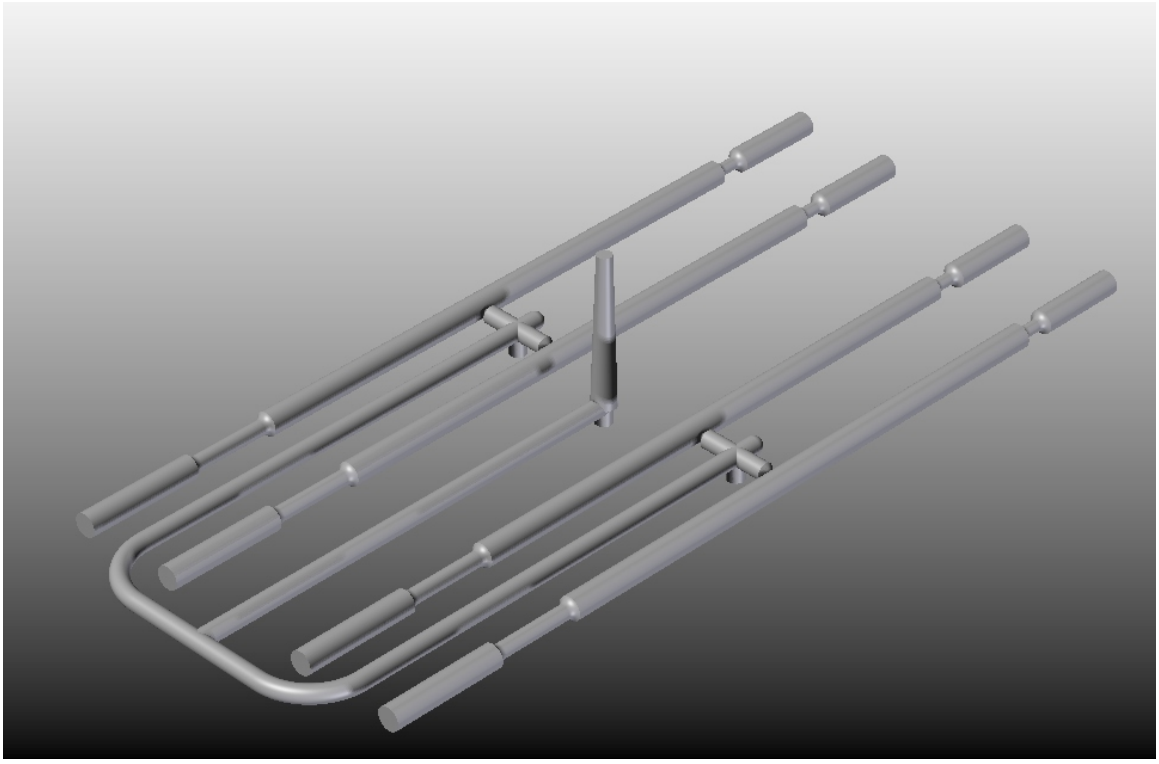

Figure 3.1.2: Molded part from which the specimens were obtained.

As can be seen four identical cylinders, each of which will provide one specimen, constitute the molded part. The four parts were detached from the sprue and cut obtaining the specimen (Figure 3.1.3). The specimen geometry is shown in Figure 3.1.4.

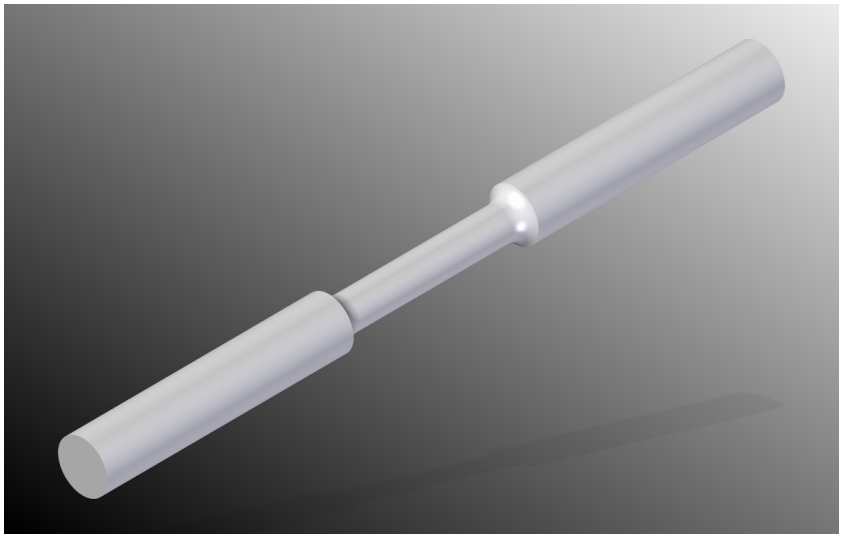

Figure 3.1.3: Image of the specimen.

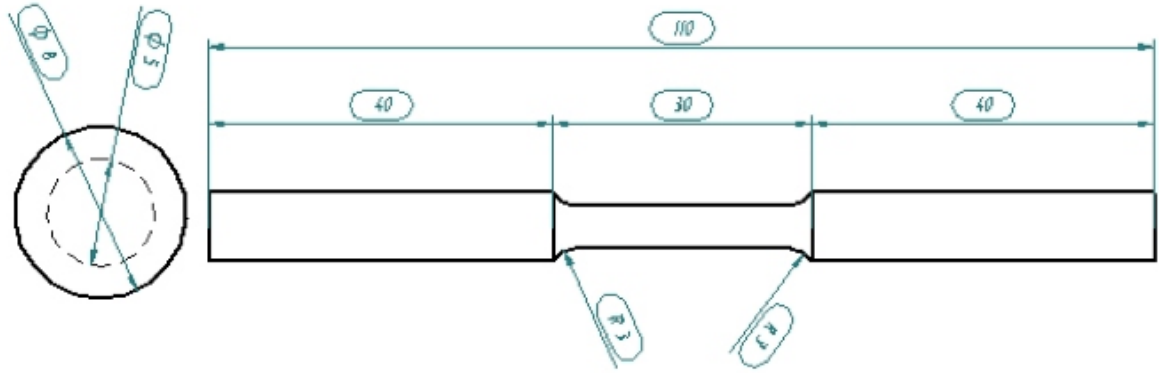

Figure 3.1.4: Dimensions of the specimen used in this thesis work.

In all the other works present in the literature the flat dumb-bell specimen with the classical geometry has been used. The disadvantages of this geometry are that, during the test, the lateral side of the specimen cannot be seen by the cameras. Thus, all the authors introduced an approximation to estimate the deformation value in this face of the specimen introducing an error in the measurement.

The cylindrical geometry adopted in this thesis work is axial symmetric. The principal advantage of adopting this geometry is that, differently from the flat dumb-bell specimen, half of the whole surface of the specimen is seen by the cameras. Thus, the distance between two extreme points located at the same height is the diameter of that cross-section of the specimen. This fact allows using an image analyzing software to measure the evolution of the diameter in the most solicited section of the specimen (Figure 3.1.5). The image analysis software used in this thesis work is the ImageJ. Once the diameter in the most solicited section is known the area can be easily calculated. This area is the one used in the calculation of the true stress by dividing the load by this value. Therefore, no systematic error is introduced in the true stress calculation because the true area of the specimen is obtained from the diameter which is directly measured.

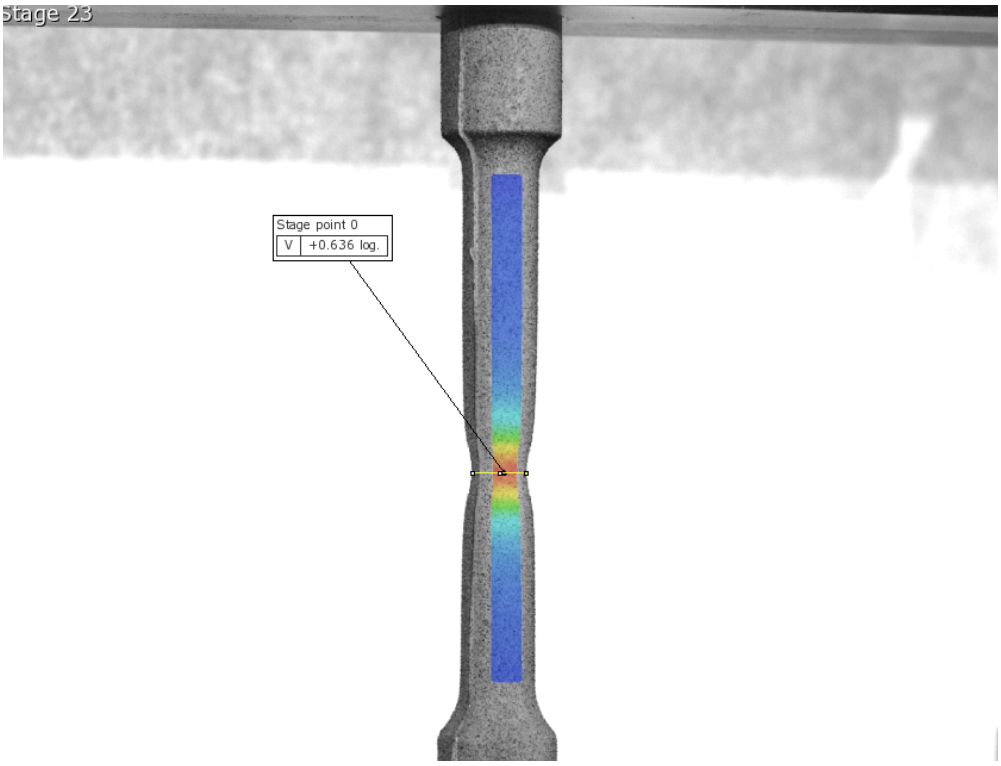

Figure 3.1.5: Example of the measuring diameter method with the software ImageJ; the yellow line in correspondence of the measuring point is the one representing the diameter of the specimen in the most stressed section.

3.2. Strain measurement by DIC

A lot of different DIC software have been developed in the last years. The algorithm is the same for all of them but each one has different analysis tools for the management of the results. The one used in this thesis work is the Aramis software by GOM and in the following paragraph its functions will be presented and explained.

The software used in this work is the Aramis developed by GOM. Aramis is a 3D Digital Image Correlation (DIC) software that allows to analyze, calculate and document deformations. This software recognizes the surface structure of the measuring object in digital camera images and allocates coordinates to the image pixels. The first image in the measuring project represents the undeformed state of the object; the software will compare the digital images with the first one and calculates the displacement and deformation of the object characteristics.

If the measuring specimen has only a few object characteristics like in the case of homogeneous surfaces, the operator needs to prepare the surface by means of suitable methods, e.g. apply a stochastic color spray pattern.

Aramis is very useful for three-dimensional deformation measurements under static and dynamic load in order to analyze deformations and strain of real components.

In this work the Aramis software was used to analyze the true strain in the two directions (parallel and perpendicular to the direction of load application) in the most strained section of the specimen. This data has been used to derive the true stress-true strain diagram and the true volumetric strain-true linear strain diagram of the specimen.

Aramis system is composed by:

- Sensor with two digital cameras (for 3D setup) with 23 mm lenses
- Stand for secure and steady hold of the sensor
- Trigger box for power supply of the cameras and to control image recording
- High-performance PC system

There are a series of steps needed in order to carry out a test; these steps will be explained below and are: calibration of the sensor, preparation of the specimen, computation and analysis of the results [27].

3.2.1. Calibration of the sensor

In general, the Aramis sensor unit operates on a stand in order to optimally position the digital cameras with respect to the specimen. For a 3D measurement setup, two cameras are used and calibrated prior to measuring. The calibration process creates a 3D space in which the specimen needs to be during the test because this is the space in which the measurement is possible. After creating the measuring project in the software, images are recorded in the various loading stages of the specimen.

Depending on the size of the measuring object, the correct measuring volume is assigned. This is the volume in which the software can detect the object and compute the strain. Once the volume is known, to calibrate the sensor is necessary to set the following parameters using the manual of the Aramis system (Figure 3.2.1):

- Measuring distance
- Base distance
- Depth of field at aperture
- Camera angle
- Size of the calibration pattern

Once the sensor is positioned, it is necessary to focus the two cameras separately and set the aperture of the lenses so that the image of each camera presents the same temperature map. The temperature map (Figure 3.2.2) shows the quantity of light captured by the lens in every point of the image. Together with the focus this is a very important step of the preparation of the sensor because otherwise the analysis will be impossible.

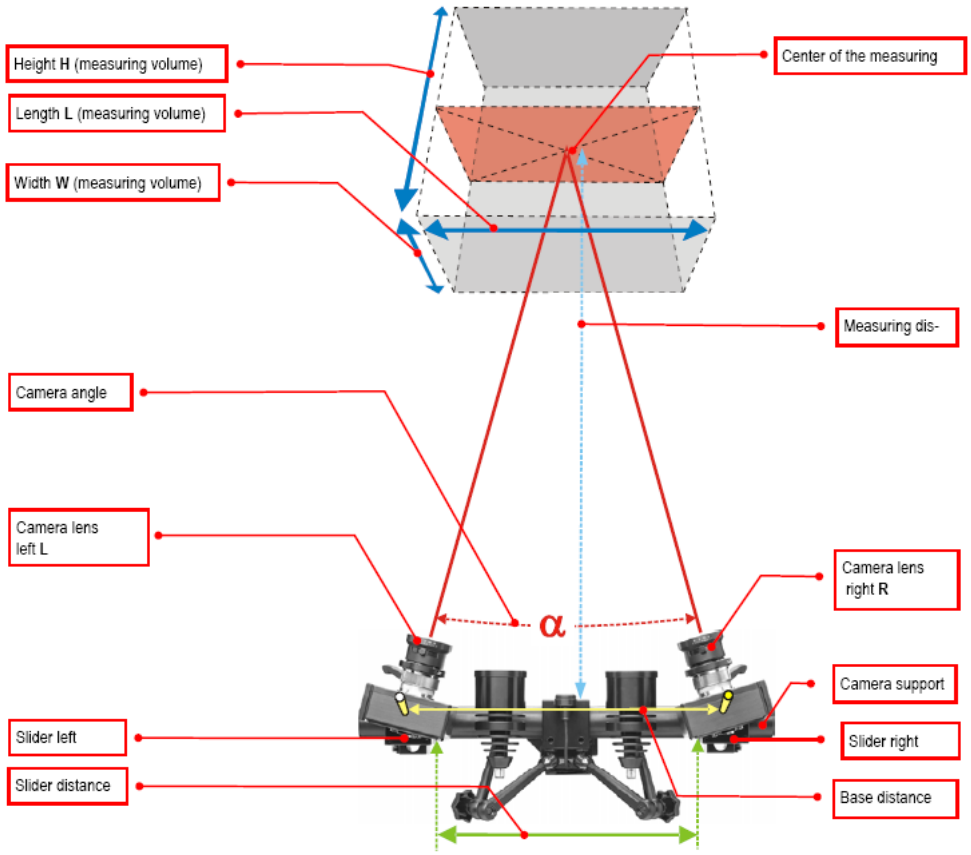

Figure 3.2.1: Position and parameters of the cameras.

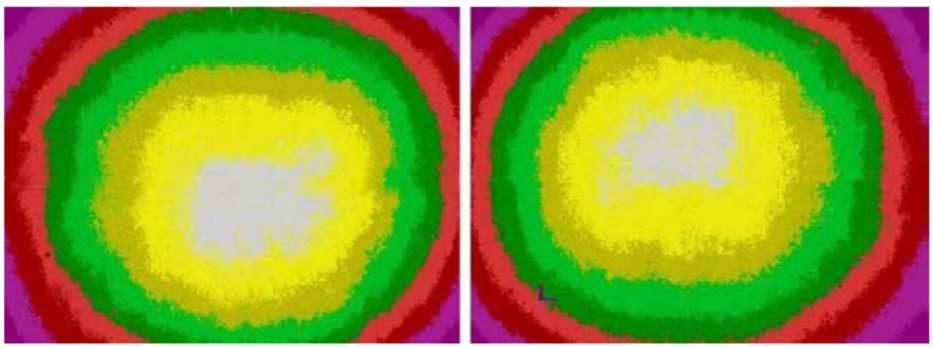

Left camera Right camera

Figure 3.2.2: Example of a temperature map.

The third and last step is the calibration of the measuring system to ensure the dimensional consistency with the measuring volume. Associated with the Aramis software there are two different calibration objects (Figure 3.2.3): calibration panels for small measuring volume and calibration crosses for large measuring volume. They are available in different sizes depending on the measuring volume. The calibration objects are equipped with so called reference points. Also, each calibration object contains the scale bar, which is the specified distance between two specific points. In this thesis work is the calibration panel characterized by the dimensions 65mmx52mm was used.

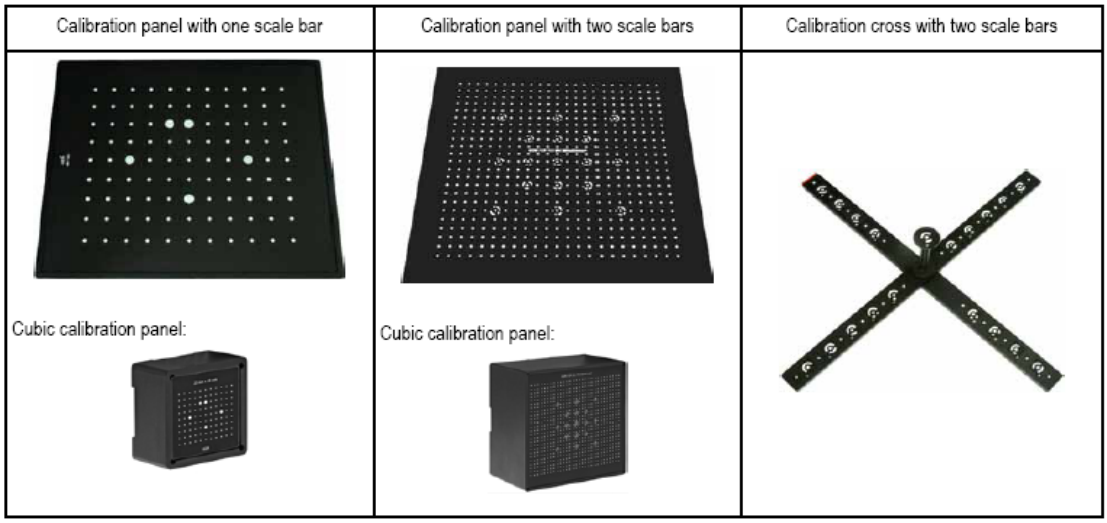

Figure 3.2.3: Different types of calibration objects which can be used in the calibration phase of the Aramis software. The first on the left is the one used in this thesis work.

At the end of the calibration process the software displays the results in terms of deviation. For a correct calibration, this value may be between 0.01 and 0.04 pixels. A

high deviation indicates a wrong or damaged calibration object or an incorrect scale parameters.

3.2.2. Preparation of the specimen

The preparation of the specimen is a key step of the process because without a good preparation the computation will be impossible. If the surface of the specimen has only a few object characteristics like in the case of homogeneous surfaces, the operator needs to prepare the surface by means of suitable methods, for example apply a stochastic color spray pattern. The specimen's surface must meet the following requirements:

- The surface of the measuring object is divided into zones (facets) which must have a pattern (grey level structure) to be identified. Then a facet pattern within the reference image can be allocated in the corresponding one in the target image.
- The surface pattern must be able to follow the deformation of the specimen. The surface pattern must not break early.
- The optimum specimen surface is smooth. Highly structured surfaces may cause problems in facet identification and 3D point computation.
- The pattern of the object should show a good contrast because otherwise such an allocation (matching) does not work.
- The surface pattern must be matte. Reflections cause a bad contrast and brightness differences between the right and the left camera, which prevent the facet computation in the areas of reflection.
- On one hand, the size of the surface characteristic should be small enough to allow a fine raster of facets during evaluation. On the other hand, the pattern should be large enough to be completely resolved by the camera.
- Stochastic patterns adapted to the measuring volume, camera resolution and facet size are the most suitable. In addition, for calculation, it is advantageous if they do not have large areas of constant brightness (for example large spots). The more appropriate are structures with changing grey values typical of the random speckle patterns.

These characteristics of the surface pattern depend on certain parameters: the surface quality, the paint quality and the ability of the operator. The surface has to be clean and degreased in such a way that the paint can optimally adhere. Furthermore the paint has to be matte so that the reflections will be avoided. Finally, the operator has to find the correct distance between the specimen and the source of the paint, the correct pressure on the valve and the exposure time of the surface to the spray to produce a good stochastic pattern, which will lead to a good and easy computation of the software.

3.2.3. Computation

At the end of the test the captured images can be analyzed. At this point the operator needs to perform a series of steps in order to analyze the images and obtain the deformation in every point of the specimen. The four steps are definition of the parameters of the facets, definition of the area to be evaluated, definition of the "start point" and computation of the strain.

3.2.3.1. Definition of the parameters of the facets

During computation, Aramis observes the deformation of the specimen through the images by means of various square or rectangular image details (facets). From each valid facet, a measuring point results after computation. Therefore, the adjustment parameters of the facets are important for strain computation and visualization. There are two parameters that can be changed in order to vary the facet field: the facet size and the facet step. The facet size is the size of the edges of the facet; the facet step is the distance between the center points of two adjacent facets (Figure 3.2.4). The software applies default values for facet size and step that are a compromise between accuracy and computation time, but the operator can change these values if, for example, the surface pattern of the specimen or the measuring test requires it. In general the stochastic pattern structure should clearly result within the facets. Varying the parameters will change the accuracy and the computation time of the project: if the size increases the accuracy improves but the computation time is longer and vice versa; if the step increase the measuring point density decreases and the computation time is shorter and vice versa.

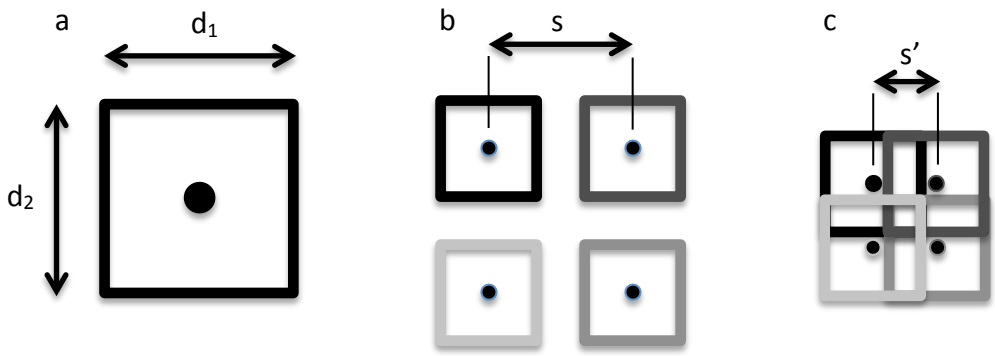

Figure 3.2.4: Scheme of a facet (a), representation of a mesh with large facet step (b), representation of a mesh with short facet step (c).

Figure 3.2.4 (a) represents a scheme of a facet: the two dimensions are the facets sizes in the two directions; the black dot in the center of the facet is the point in which is calculated the deformation. This means that for every facet there is only one measuring point. Figure 3.2.4 (b) is a representation of the mesh of facets: the distance between two center points of two adjacent facets is the facets step and can be set differently in the two directions of the plane. In this case the resulting strain field will be spread and not dense enough to describe what happens locally. Finally, Figure 3.2.4 (c) represents a mesh of facets in which the facets step is shorter than the facets size; thus the center point of a facet results inside the area of the near one. This allows obtaining a denser distribution of analysis points and so a better representation of the strain field. However, if the facets step is too small, the strain measured can be wrong because the results are redundant.

The best representation is obtained compromising between measurement reliability and faithful representation of what is happening locally to the deformation.

In Figure 3.2.5 a practical example of how the facets parameters influence the analysis is presented. In the analysis on the left the facets size is 15 and the facets step 15; as can be seen the mesh is coarse and the analysis become impossible at the stage number 56 (5.6 seconds since the beginning of the test). While, in the analysis on the right (same test but different parameters) the facets size is 19 and the facets step is 3; as can be seen the mesh is much more fine and thus the resulting analysis is better: the last image on the right refers to the same stage (56) but, in this case, the analysis is still possible.

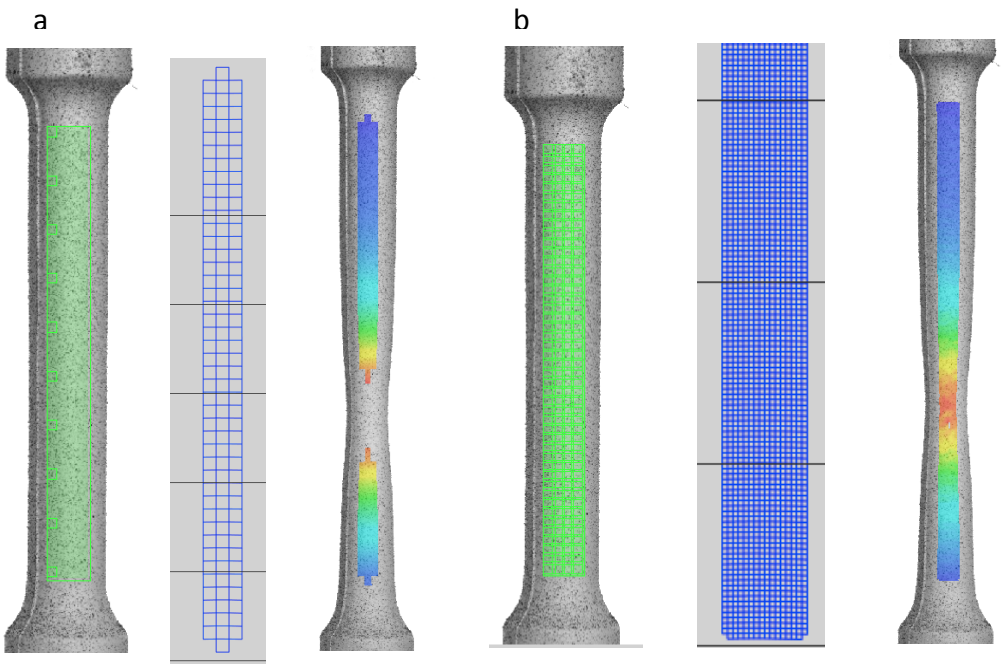

Figure 3.2.5: Example of how the facet parameters influence the analysis; larger facet parameters (a) and smaller facet parameters (b) analysis.

Another important characteristic of the facets is the shape, which can be set as square, rectangular or quadrangular. The facet shape influences the computability of the measuring project. Square and rectangular facets in the reference stage are always aligned according to the x-y orientation of the 2D image. The quadrangular facets are used in case of quadrangular specimens if one wanted to create valid facets up to the edge. In this case a facet field, which follows the specimen's geometry, has to be created manually.

3.2.3.2. Definition of the area to be evaluated

Before starting the computation an area of analysis has to be defined. This area is the zone of the image in which the software will carry out the analysis excluding the other parts; this area can be the whole picture or a part of the image (i.e. if only the deformation of a part of the specimen is needed). Moreover, Aramis has a second area definition tool: the computation mask tool. This allows eliminating specific regions of the image from the analysis; for example fixtures, backgrounds, specimen edges and contour jumps. This tool is very important in some 3D case as the 3D computation of the measuring points is based on facets that need to be seen from the right and left camera. Thus a proper 3D computation is impossible in case that only one camera can see a part

of the specimen like specimen edges, holes and contour jumps (Figure 3.2.6). This problem has been found also in this thesis work tests because the specimen contours, with this geometry, is seen only from one of the two cameras; thus, these zones of the images were eliminated from the analysis.

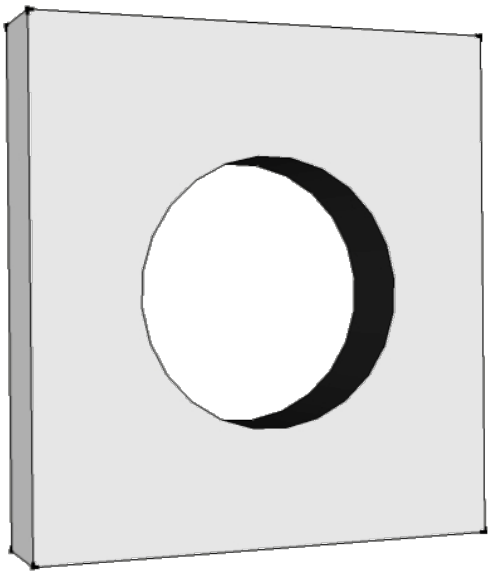

Figure 3.2.6: Example of a specimen which presents a hole in the center. In this case the surface of the specimen near the hole has to be eliminated from the analysis.

3.2.3.3. Definition of the "start points"

Before computing the strain, a "start point" in every image of the project has to be defined (Figure 3.2.7). A start point is a facet whose strain is calculated before running the analysis. The software needs to know this value of deformation in order to compute the strain in all the facets that compose the mesh of the project. The final strain field is function of the value of the start point deformation.

Generally, the start point refers to the same facet in all images. However it is possible to work with different start points in one measuring project. For example, if after computation it turns out that for some stages Aramis could not calculate any facets. Finally, if a specimen breaks apart during the test and if it is necessary to record the deformation in the fragment as well, it is necessary to define another start point in the area of the fragment.

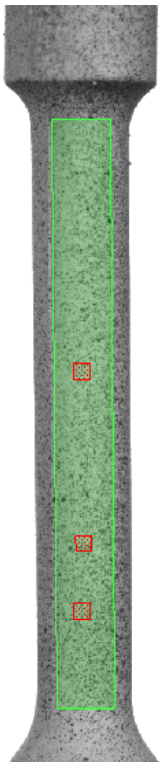

Figure 3.2.7: Positioning of the start points (red squares) in the region of the analysis (green area).

3.2.3.4. Computation of the strains

The computation of the project is possible because in the different loading stages the facets are identified and followed by means of the individual grey level structure. The system determines the 2D coordinates of the facet from the corner points of the facets and the resulting centers. Using photo-grammetric methods, the 2D coordinates of a facet, observed from the left camera and the 2D coordinates of the same facet, observed from the right camera, lead to common 3D coordinates.

The information that Aramis collects during the test are displacements and strains of the facets as a function of time. As previously explained, in the undeformed stage Aramis constructs the facets mesh over the stochastic pattern associating each facet with a level of grey structure. Thus, during computation, the software redesigns the facets in each image depending on the actual position of the black paint dots which composed the stochastic pattern in the undeformed stage. Following the position of the center point of a facet as a function of time gives the relative displacements of the surface of the specimen. Once the facets have been redesigned in each image, Aramis measures the

actual dimensions (height and width) of the rectangle calculating the strains of every facet in the two directions (Figure 3.2.8).

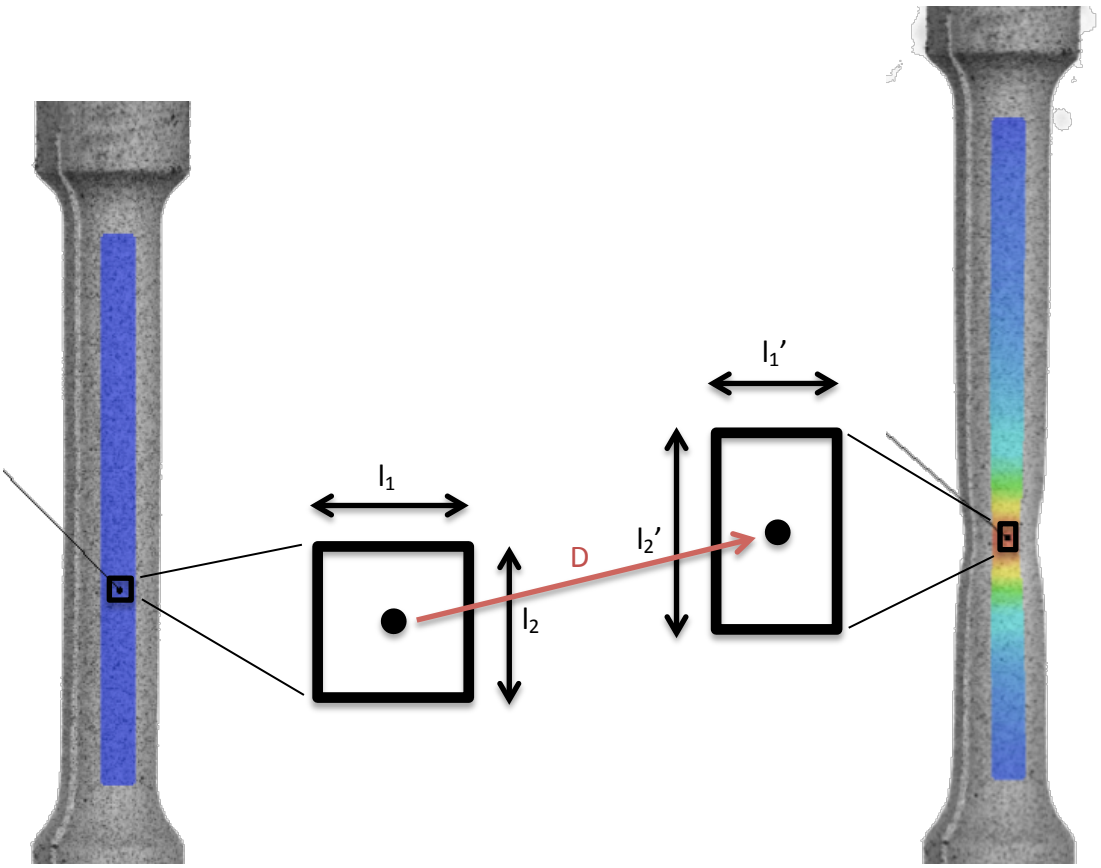

Figure 3.2.8: Scheme of the Aramis analysis process. It compares an image (right) with the undeformed state (left); it compares the position of the same facet in the two images gathering the displacement; it calculates the strains in function of the changing dimensions of one facet.

For strain computation Aramis distinguishes between two methods: linear strain and spline strain computation. The main difference between the two methods is that the spline strain computation allows the analysis also in case of small curvature of the surface (in the order of magnitude of the facet size). This is possible thanks to the fact that the strain computation considers also the interpolated points between the "real" points (center of the facets); these points are interpolated from the real ones using the spline function.

When the project needs to be computed there is also another parameter that can be changed: the strain method that can be set as total or step-by-step. In the first case the deformation is calculated with respect to a determined stage (image) of the project,

which usually is the undeformed one. In the second case, however, the strain is calculated one stage with respect to the previously. In this thesis work the strain method used has been the first one even if at some point during the development of the analysis the step-by-step method has been used leading to the same results.

3.2.4. Analysis of the results

After the strain computation the data are available as color 2D or 3D view of each stage. The software has a lot of different 3D representation; the most important are the representations of the strain: Tresca strain, Mises strain, maximum and minimum strain (maximum strain is the strain in the direction of the application of the stress while the minimum is the strain in the direction perpendicular to the application of the stress). There are also other possible representations like thickness reduction and differences of displacement in the different directions. It is also possible to define different visualizations from the standard ones.

The resulting representation of strain can be visualized as technical, logarithm or according to Green. In this work the representation used is the logarithmic one because this is the true strain (i.e. Hencky strain).

Aramis has some tools which allow to analyze specific results as the deformations at a given location or linear strain between two points. In this thesis work the tools used in order to get the information needed for the analysis are the following:

1. Stage points which are individually definable points in the 3D view of the specimen. These points are used for getting local information (like strain or displacement) and are defined on the surface of the specimen. For every facet one stage point can be assigned in correspondence of the center of the facet. These points are very powerful tools, which allow creating local behavior diagram over all stages. In this work this tool was used to get the local true strain value relevant to the most stressed section of the specimen.
2. Primitives are user-defined objects in the 3D view. These tools are needed, for example, for the analysis or for the documentation of measuring results. These objects can be classified in nine families: points, lines, planes, circles, slotted holes, rectangular holes, spheres, cylinders and cones. In this thesis work the line

primitive was used together with the analysis elements tool which allows to measure distances and angles between points and lines. Using these two tools allows calculating the standard deformation across the necking zone and thus allows knowing the standard stress-strain behavior of the material.

3. Aramis has a third tool: the section tool which allows creating plane sections, circular sections and spline sections in all the stages of the analysis. These sections allow analyzing the deformation or other results along a line on the surface of the specimen. However, the section tool was not used in this work.

Chapter 4. Development of testing procedures

4.1. Setup of the strain measurement procedure

The main objective of this work was to develop a technique that allows the measurement of the true strain of a series of polypropylene based materials up to large strains using the Aramis software. The individuation of a proper paint, the obtaining of a randomly good spread matte surface pattern and the optimization of the deformation analysis are some of the problems that were faced.

4.1.1. Type of paint

To obtain a good contrast of the pattern, in this work two different paints were placed on the surface of the specimen (Figure 4.1.1): a white one and a black one. First of all a white layer is applied on the whole surface homogeneously and then a stochastic black pattern was sprayed with the black paint. In this way a very good contrast is obtained and the software can easily assign and identify the facets and compute the strain on the surface of the specimen.

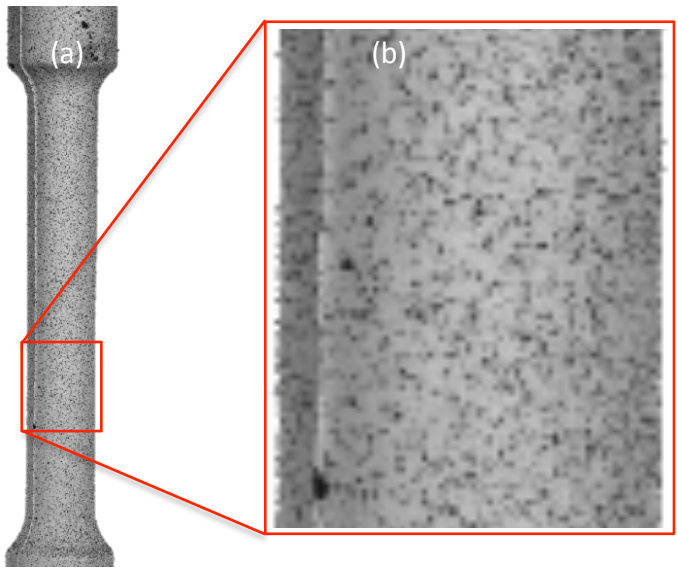

Figure 4.1.1: Image of a specimen before the test (a). Magnification of a section of the surface (b).

A large variety of paints were tested before finding the one that could ensure good quality of the surface, the proper deformability and good adherence with the surface of the specimen. Particularly both paints have to be matte to avoid reflections and deformable like polypropylene because they have to reproduce exactly what is happening on the surface of the specimen if not the analysis will not be correct. Moreover, the white paint has to have a good adherence with the surface of the specimen; for the black paint this is not a problem because it has to adhere on the white layer and not directly on the polypropylene.

Initially, very bright black paints were used and so the analysis resulted impossible because the software could not detect and follow the facets during the test. On the other hand, the white paints used, presented adhesion and deformation problems. Both of them should be avoided because both will false the analysis. The first problem depends on the properties of the paints and of the material while the second one depends only on the paint used. The first white paints used formed a layer of paint that deforms independently of the deformation of the specimen below and so, during the test, this layer breaks after the failure of the specimen. In this way the value of the strain measured is not the one of the specimen. Other types of white paint were not as deformable as the material of the specimen and/or had a poor adherence with the substrate. This caused the layer of paint to break before the specimen itself does.

Finally a good combination of white and black paints was found: a white heatproof paint produced by Felton spray and a black acrylic synthetic enamel. The white paint chosen presents a good adherence on the surface of the specimen and a value of deformation very similar to the one of the polymer. Moreover, the black paint is matte and its nature allows to easily obtain a fine dispersed pattern.

4.1.2. Obtaining of a randomly good spread surface pattern

Obtaining a good quality pattern is not easy but it is very important for the quality of the software analysis. This step of the preparation of the specimen surface, as mentioned before, is very operator dependent because the operator has to find the right conditions of distance between the specimen and the spray, pressure applied to the valve and time of exposition. This three parameters influence the dimensions of the black paint dots of

the pattern, the dispersion of the paints and the contrast between the white paint layer and the random black pattern. Hence they directly influence the success and the quality of the analysis. The optimal values of these parameters were:

- The optimal distance between the specimen and the spray is approximately 80 cm. If the distance is larger the pattern results too white and the dots result too fine, while if the distance is smaller the dots will be too large and the overall level of grey will be too dark.
- The pressure applied to the valve must be neither too high nor too low. If the pressure is low the spray can contain large drop of paint because the valve is not able to disperse the jet, while if the pressure is too high the time of exposition to obtain a good quality grey pattern is very short and difficult to control.
- The time, for the same reasons, has to be a few seconds (approximately 7).

4.1.3. Optimization of the deformation analysis

This problem was the most difficult to solve. In fact the software was not able to analyze the whole set of images captured during the test: in the zone of the specimen where the deformation is maximum (i.e. in the neck zone) the analysis was impossible after the true strain reached a value of approximately 0.9-1. Figure 4.1.2 reports a sequence of strain analysis images of a test; the first image on the left was taken at 5.8 s of analysis and the last one on the right at 6.4 s. As can be seen the strain analysis became impossible around the sixth second.

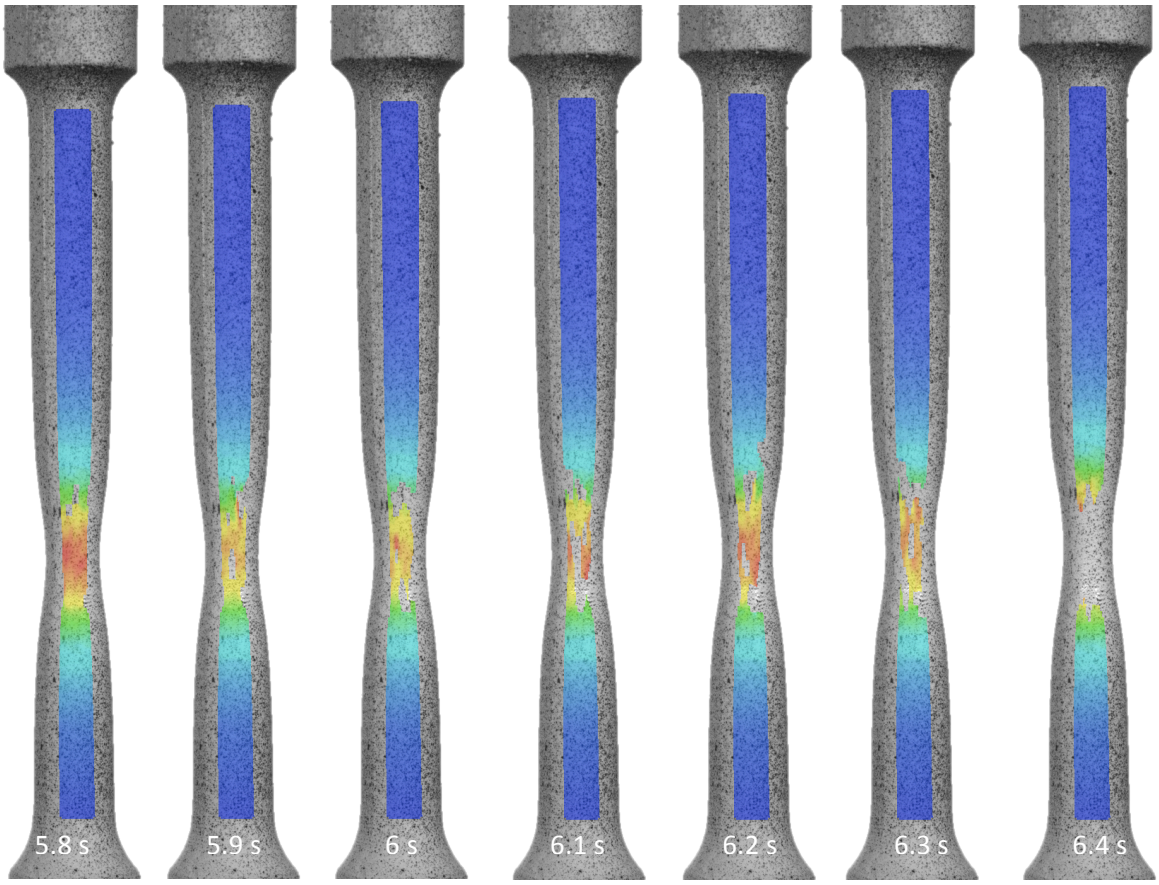

Figure 4.1.2: Series of analyzed images showing that the analysis became impossible after approximately six seconds (true strain of approximately 1 depending on the test).

As said before this was the most difficult problem to solve and a lot of time was spend trying to understand what caused this problem and how to avoid it. Two hypothesis to explain this phenomenon were formulated:

1. The deformations of the facets (length and width) were too high for the software to analyze.
2. The contrast of the random pattern changes significantly during the test and after some value of deformation, locally, the contrast is very different from the original one and so the software cannot “follow” the facets from one image to the next one.

With reference to the first hypothesis two solution were investigated: firstly, it was thought that the cause was the not optimal calibration of the sensors of the Aramis software but no difference was observed after a lot of different calibrations were done. Secondly, the cause of the problem was identified in the software parameters of the

analysis like the size and the shape of the facets and the area of analysis. Different tests were done changing the initial dimensions of the facets and the extension of the analysis area but no significant improvements in terms of maximum strain measured were observed. This was the first signal that the cause of the problem in the analysis was not the large local deformation as will be well explained later. Figure 4.1.3 presents two examples of two different facets dimensions used in these tests; in the first one on the left the facets are squared while in the one on the right the initial geometry is rectangular with the shortest dimension parallel to the direction of application of the load. The difference is that at the same level of deformation the facets on the left results a lot more flat than the one on the right.

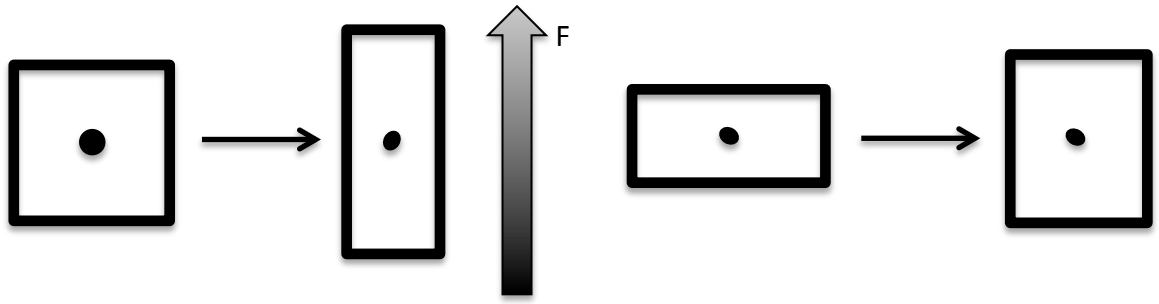

Figure 4.1.3: Example of adopted facet geometries and relative deformed states.

With reference to the second hypothesis two solutions were investigated. Firstly, it was thought that the problem was caused by the paint, but it persists after that the best combination of white and black paint was found although a small increase in the time of the analysis was observed. Secondly, the cause was identified in the initial properties of the pattern like the contrast and the size of the dots of black paint Also in this case a small increase in the time (and maximum deformation) of the analysis was observed but changing the parameters did not affect significantly the quality of the analysis.

After these hypotheses were investigated with no success the final solution of the problem was quite simple conceptually: the analysis is carried out in two steps.

In the first step the analysis is carried out until the software can measure the local deformation in the most stressed section, while, in the second one, the analysis is carried out taking as undeformed stage the last image of the analysis of the first step (Figure 4.1.4). Therefore the total deformation at any time in the second step is the sum of the

deformation in the last image of the first step plus the deformation of the image of the second step, which corresponds, in terms of time, to the one to be measured.

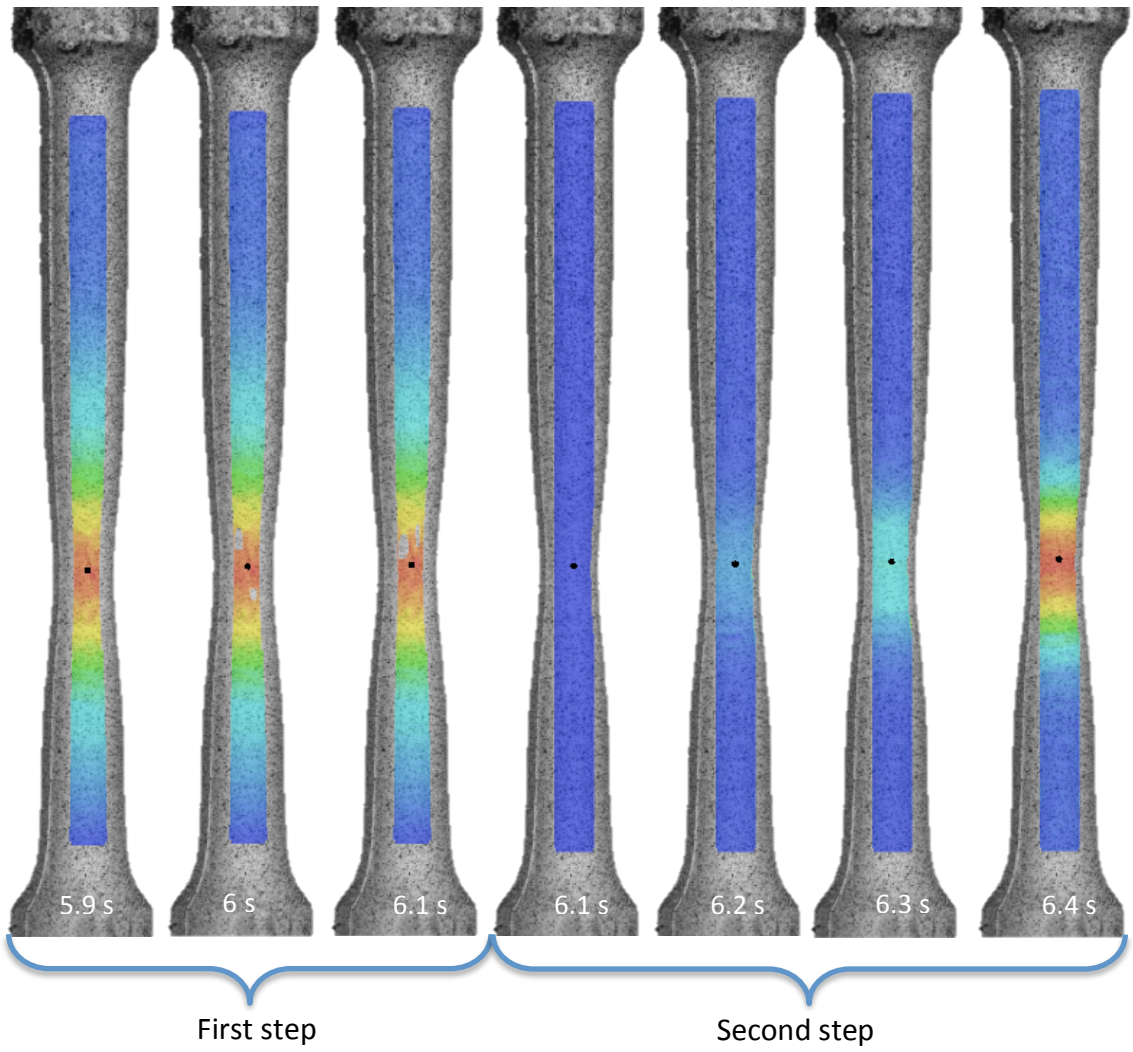

Figure 4.1.4: Demonstration of how works the adopted technique.

This technique is not the standard one and the results are affected by some problems and systematic errors. In the following these problems and the relative solutions are explained.

The first problem is that the results obtained switching from one step to the other at a certain image were different from the ones obtained switching at a different image. This problem was observed and studied in a test with the material PB 150. In this test the volume strain measured changing from one step to the other at the image number 64 is

about 15% larger with respect to the one measured changing at the image number 50 (Figure 4.1.5 a).

Initially has been thought that the cause was mathematical but this hypothesis was immediately rejected. Thus, has been thought that the problem was somehow linked with the mesh and the facets and so a series of hypothesis were made before the cause and the solution of this problem were found:

1. It has been thought that the cause of the problem was the dimension of the "mesh". The parameters of the project were changed to make the mesh denser and so the maximum number of images analyzable descends to 58 from 64. Therefore the results were not directly comparable but the difference between the total volume strain changing the file at the stage number 58 or at the stage number 45 was smaller. In this way has been realized that the problem was not mathematical but it was an error due somehow to the mesh and the change of the mesh between the two steps (Figure 4.1.5 b).
2. The geometry of the facets in the "mesh" of the second file was changed. The original square shape has been substituted by a rectangular one with the height greater than the width (similar to the shape of the facets in the deformed zone in the last picture of the first step). This change introduced a significant decrease in the difference between the two volumetric strain; therefore the next step has been to produce the most similar "mesh" in the first stage of the second step to the last stage of the first one (Figure 4.1.5 c).
3. Finally the last passage has been to try to produce the most similar "mesh", in the most stressed section, between the last image of the first step and the first image (undeformed stage) of the second step. This caused a significant reduction of the difference between the two values of the volumetric strain (Figure 4.1.5 d).

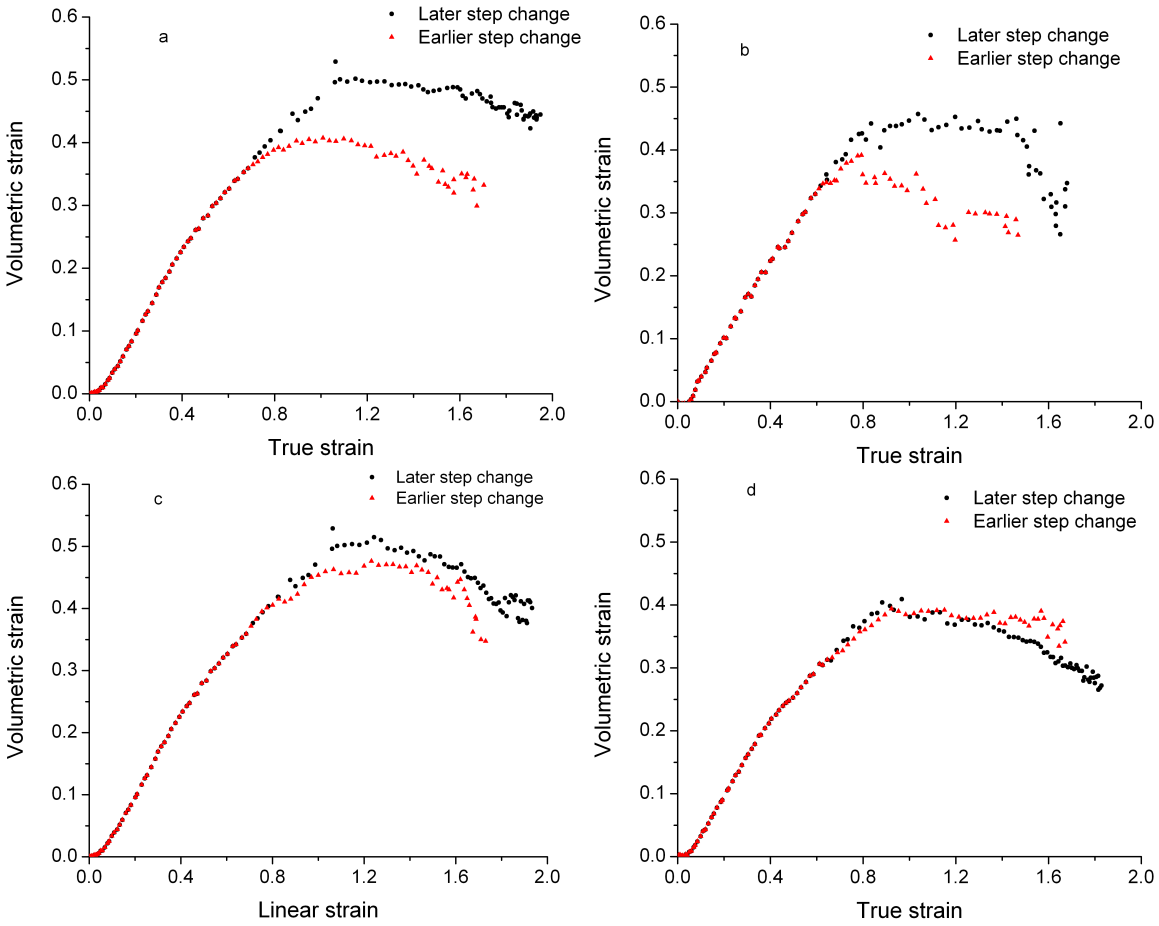

Figure 4.1.5: Volumetric strain-linear strain curves of the initial analysis (a), the analysis of the tests with the denser facet mesh (b), the analysis of the tests with the facets with changed geometry (c) and the analysis of the tests with the same mesh (d).

With this method two results have been obtained.

The first is that the cause of the limits of the analysis after that the true strain reaches the value of 0.9-1 (as previously explained in this paragraph) was not the large local deformation but it was the difference in contrast between the reference stage and the final image. This is due to the fact that if the problem was the difference between the two dimensions of the facets (height and width), in the second step, which shows the same mesh dimensions, the analysis should not be possible, while the analysis in the second file can easily reach the same deformation of the first file (and so, in total, a true strain of approximately 2).

The second result is that the cause of the high error in the volumetric strain is due to the different positioning of the analysis point in the last stage of the first file and in the first

stage of the second one. This difference is going to increases in time because the two points deform differently (although very slightly). Unfortunately there is not an option in the software that allows the positioning of a point by inserting the coordinates and, moreover the points can only be placed in the center of the facets of the "mesh". Therefore, the error in the strain determination cannot be eliminated but only reduced by changing the shape and the dimensions of the facets of the mesh in the second step of the analysis. In this way the difference between the volume strains has been decreased to about 5% (down from 15%) and has been considerate as acceptable.

4.2. Setup of a procedure to perform tests at constant true-strain rate

One of the requirements of this thesis work was to perform test at constant strain rate in the most stressed section of the specimen, while the tensile machine can only work at constant crosshead rate. Thus the experimental procedure was divided in two different parts: analysis at constant crosshead velocity and analysis at constant true strain rate.

For the first part the procedure is very simple because it only consist in the preparation of the specimen, calibration of the sensor, set up of the traction test, traction test and analysis of the images with the Aramis software. The second part differs from the first one in the set up of the tensile test.

The set up of the tensile test is a necessary step, in the procedure of analysis, done using the software of the tensile machine. In this software it is possible to set a profile of crosshead rate with a maximum of eight different steps. For the analysis at constant crosshead rate this profile was simply composed by one step with the velocity set at 130 mm/min for the whole time of the test.

On the contrary, in the analysis at constant true strain rate, the crosshead rate profile was quite complicated and hard to find because it could be found only experimentally and not mathematically. Depending on the material, the profile was composed by six, seven or eight steps each of which had a different value of velocity. These values were found experimentally because it is not possible to calculate the velocity starting from the

true strain rate in one point. By acting in this way an approximately constant strain rate has been reach for the firsts 12 seconds of the tests for every material analyzed.

The velocity value of each step has been found with a “trial and error” method. The initial value of velocity (130 mm/min) has been increased or decreased every two seconds (or one second for some materials) depending if in that period of time the true strain rate of the test at constant crosshead rate was lower or higher than a fixed value. This process did not lead to the perfect profile at the first try because the decrease or increase in the velocity, and, consequently, the strain rate, depends a lot on the material. Before obtaining a good constant true strain rate analysis a number of 4 to 9 different velocity profiles were tried (depending on the material).

As an example Figure 4.2.1 reports the case of the material PB 150: the first material to be analyzed. The diagram shows the evolution of the true strain in time in the constant crosshead rate analysis.

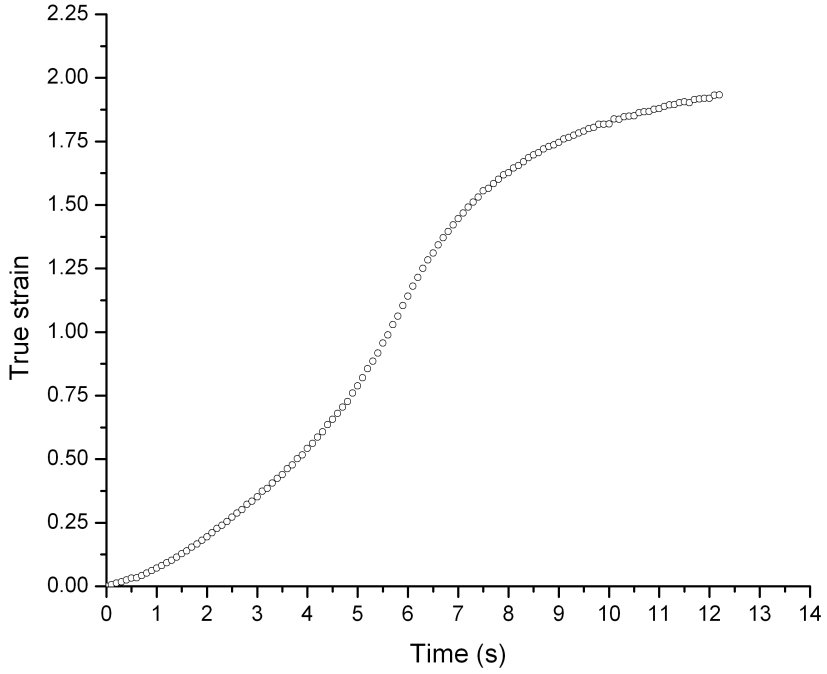

Figure 4.2.1: True strain-time behavior of the PB 150 material in a constant crosshead rate test.

This curve is a typical example of the shape of the local true strain during the tensile test: the first part in which the strain rate increases, then a middle part of constant strain rate and finally, in the last part, the strain rate decreases until it reaches a nearly constant value.

Analyze this curve was the first step of the process to derive the right crosshead rate profile by which obtain a constant strain rate curve. As previously mentioned the curve was divided in period of time (one or two seconds depending on the material) and for every period the slope (i.e. the strain rate) was calculated (Figure 4.2.2).

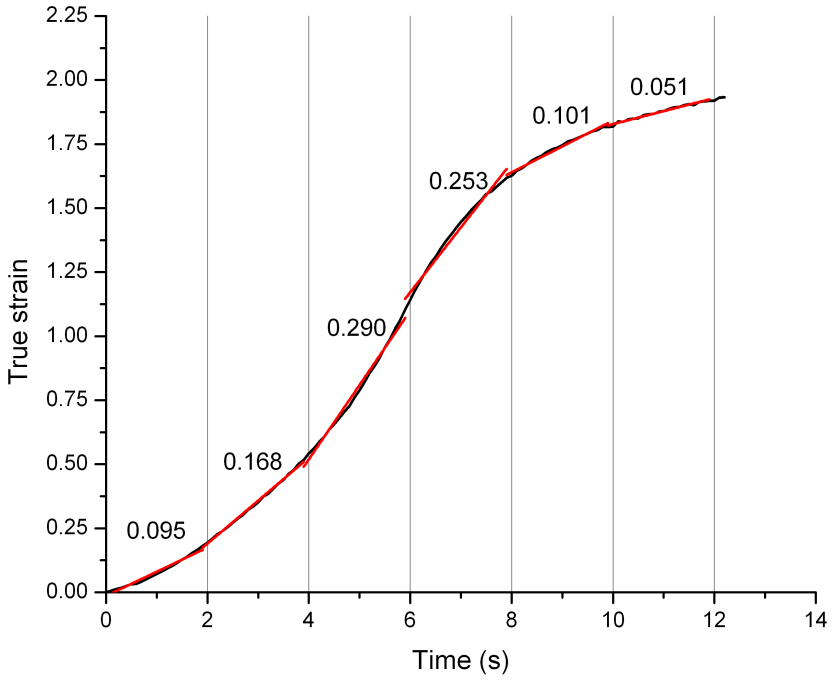

Figure 4.2.2: Analysis of the strain rate of the test by calculating the slope in every section of the true strain time curve.

As can be seen in Figure 4.2.2 the shape of the curve presents a first and a last part were the strain rate value is equal or lower to 0.1 s^{-1}, while, in the central part, this value is higher and almost reaches a value of 0.3 s^{-1}. In this work has been decided to realize the test at an almost constant value of the strain rate of about 0.15 s^{-1}.

The second step is to draw a profile of crosshead rate which is thought to produce a constant strain rate. In every period of time in which the previous curve was divided, the velocity is changed depending if the slope was lower or higher than the fixed value. In Figure 4.2.3 can be seen the first crosshead rate profile realized for the material PB 150. The value of velocity in the firsts two seconds is the same as before (130 mm/min), then, in the second period of time, this value was lowered at 106 mm/min. The same thing has been done for the other steps until a minimum value of crosshead rate of 70 mm/min has been reached between the sixth and the eight seconds.

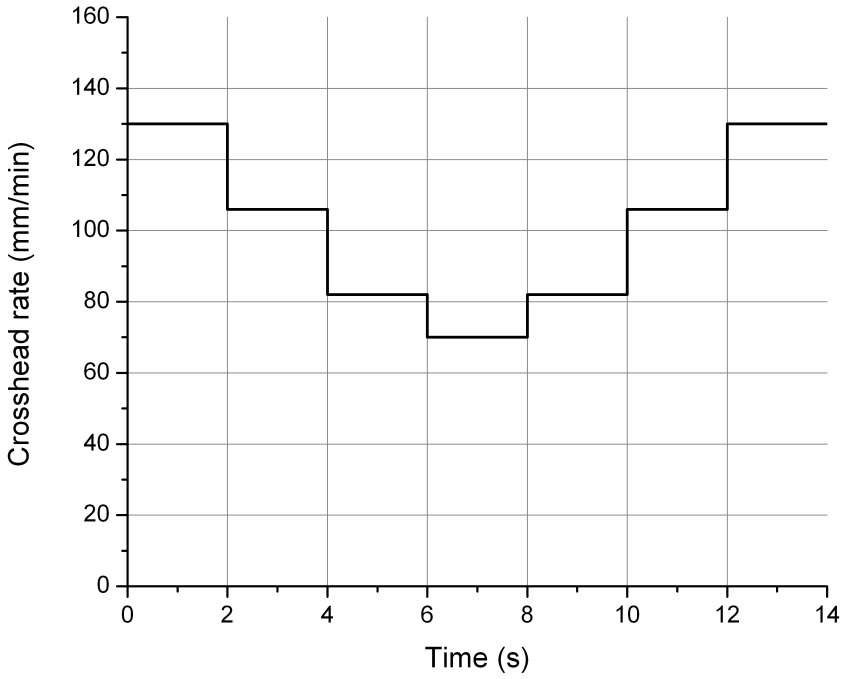

Figure 4.2.3: First crosshead rate profile of the PB 150 copolymer.

As told before this is a try-and-error method and so, as expected, the resulting strain rate was not constant as can be see in Figure 4.2.4.

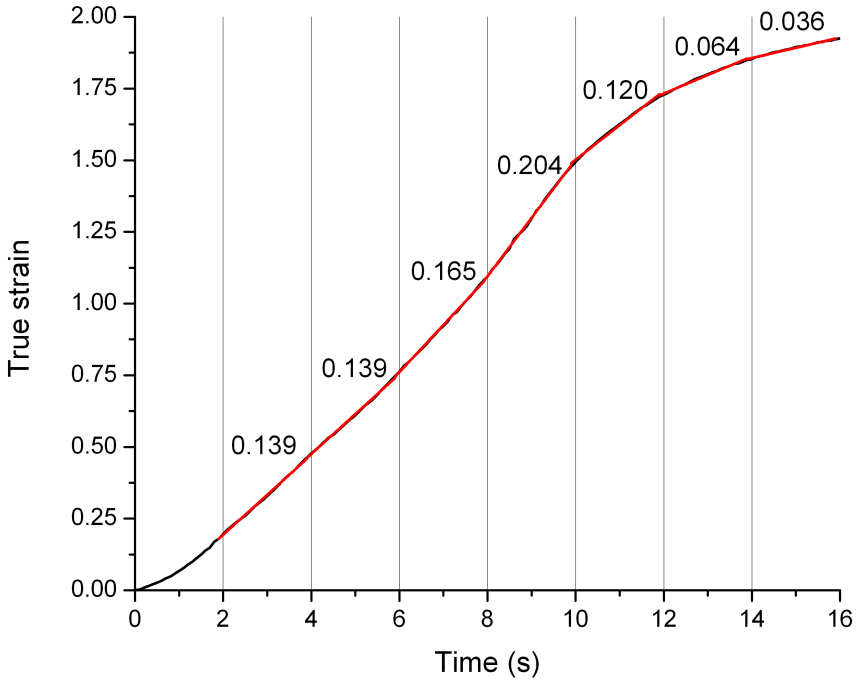

Figure 4.2.4: Strain-time of the material PB 150 during the test adopting the crosshead rate profile and relatives strain rate values.

Analyzing the diagram in Figure 4.2.4 it can be noticed that the slope of the whole curve is not so constant; particularly the section between the eighth and the tenth seconds presents a slope higher than the previous and following sectors; so, in the profile number two, the crosshead rate in this period has been decreased.

Finally, at the fourth try, adopting the crosshead rate profile presented in Figure 4.2.5 an almost constant strain rate diagram was obtained with a mean value of the strain rate of about 0.152 s^{-1} in the sector between the second and the tenth second (Figure 4.2.6). The diagram of the crosshead rate profile (Figure 4.2.5) used and the diagram of the variation of the true strain in time (with the strain rate for every sector) are reported below.

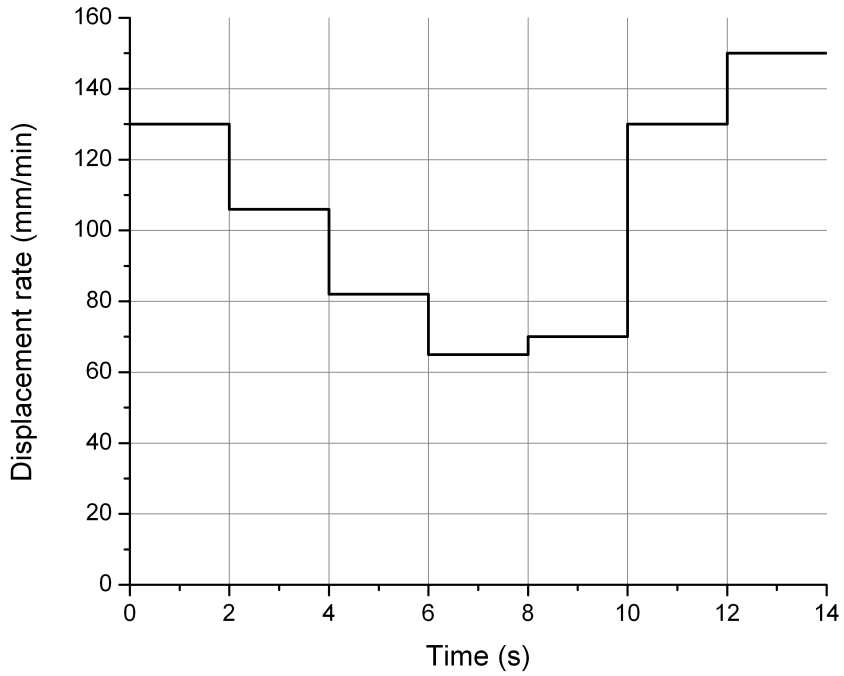

Figure 4.2.5: Profile of crosshead rate used in the PB 150 tests at constant strain rate.

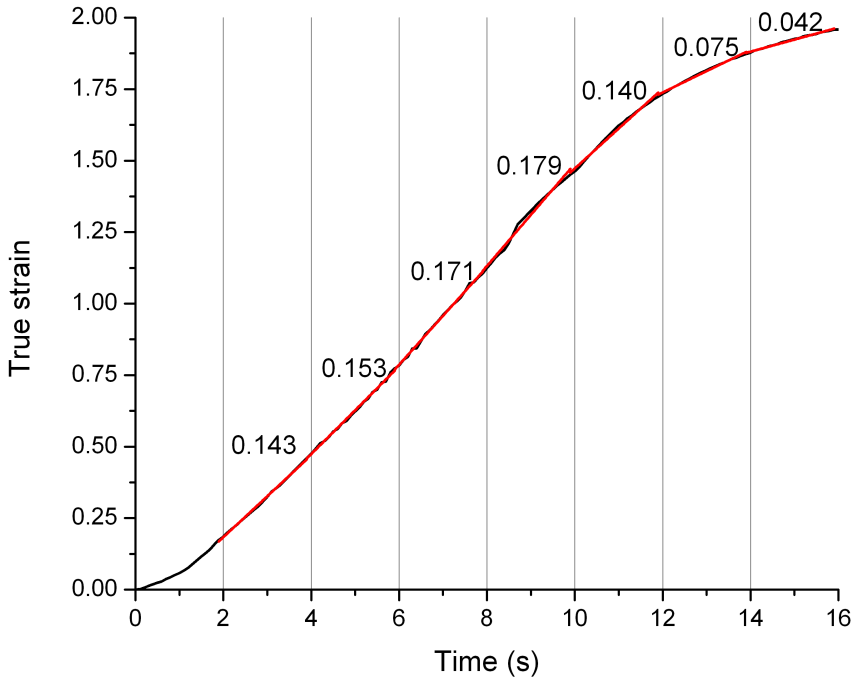

Figure 4.2.6: Strain-time of the material PB 150 during the test adopting the crosshead rate profile presented in Figure 4.2.5 and relatives strain rate values.

As can be noticed in Figure 4.2.6 in the first two seconds the slope was not calculated because this is a transition period in which the materials passes from the elastic deformation zone to the plastic one and so the strain rate value cannot be constant. The same thing occurs for the last part of the curve where the strain rate value decreases as a result of the stabilization of the neck.

In the third velocity profile, which is not reported here, the last part of the velocity profile has been replaced with an exponential function but the result was the same. Finally, only the central part, approximately between the second and the twelfth seconds, presents a constant strain rate value.

This process has to be done for every material because the same profile used with two different materials will not lead to the same strain rate diagram. Hence, for example, for the PB 170 it took six tries before reaching a good profile while, for the PP 060, it took nine try.

For each material and for each procedure (constant crosshead rate and constant strain rate) five different tests were done and the results were averaged obtaining one

behavior. Figure 4.2.7 and Figure 4.2.8 present the diagrams of the five specimens of the material PB 150 tested at constant strain rate.

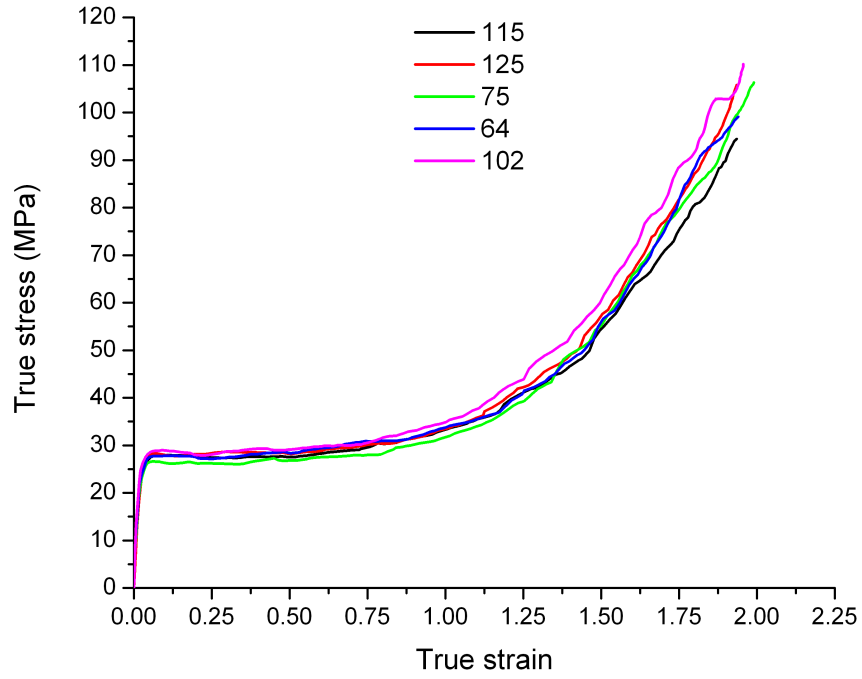

Figure 4.2.7: True stress-true strain curves of the five tests at constant strain rate of the PB 150.

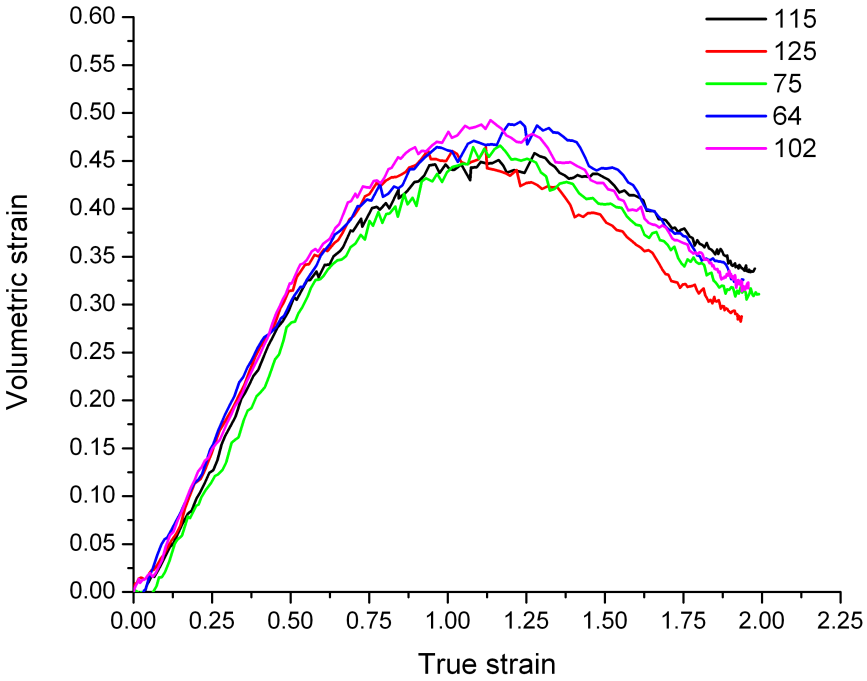

Figure 4.2.8: Volume strain-linear strain curves of the five tests at constant strain rate of the PB 150

The first sections of the five curves are very similar while the results are more dispersed after the true strain reached a value of almost 1.2; this is caused by the technique of

analysis which, as explained in paragraph 4.1.3, introduced an error in the positioning of the analysis point.

Before analyzing the results a consideration has to be done for the PB 110. This material is the one with the highest molecular weight among all the materials analyzed (Table 3.1.1) and this fact caused some problems during the injection process. Particularly, the viscosity of this material is very high and so the flow of the melted polymer in the cavities of the mold was difficult. Thus, the injection conditions (temperature and pressure) were almost extreme. Therefore, during the tensile test, every specimen peeled off almost in correspondence of the same value of deformation: ε_{true}=1.5. Consequently the tests need to be stopped at this value because the measured deformation after this would not be the real deformation of the specimen because its skin, which is the part where the software measure the deformation, deforms differently from the core of the specimen (Figure 4.2.9).

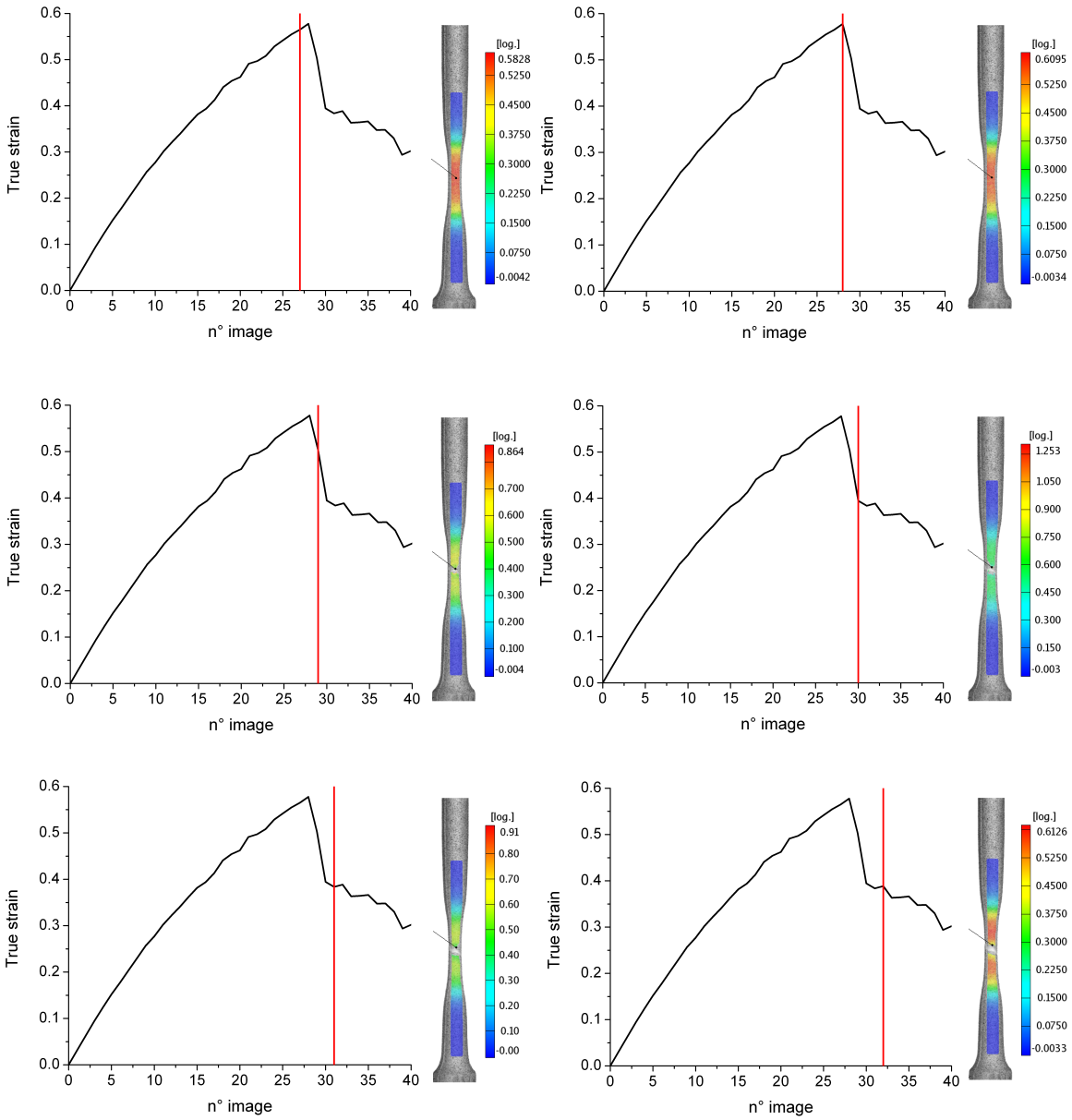

Figure 4.2.9: Peeling phenomenon during the test of PB 110 copolymer. In every image is represented the specimen with the color map of the strain, the measuring point with the logarithmic strain value and the correspondent point on the true strain-time curve.

Chapter 5. Results and discussions

Once the crosshead rate profile has been setup for every material, obtaining almost the same strain rate value, five specimens were tested for each material and a mean true stress-true strain and volumetric strain-linear strain curves were obtained.

In this chapter the results of the tensile tests of the singles materials will be presented. As mentioned above every material has been analyzed at constant crosshead rate and at constant true strain rate, and for every test two different results have been obtained: the true stress-strain curve and the volumetric strain-linear strain behavior.

Furthermore, a Differential Scanning Calorimetry (DSC) analysis has been performed in order to determine and compare the melting temperature and the crystallinity of the materials in the undeformed and deformed state.

5.1. Constant crosshead rate tensile tests

Figure 5.1.1 to Figure 5.1.5 show the mean true stress–true strain diagrams and the volumetric strain-true strain diagrams at constant crosshead rate (130 mm/min) for the five materials tested: PP 060, PB 110, PB 150, PB 170 and PB 171.

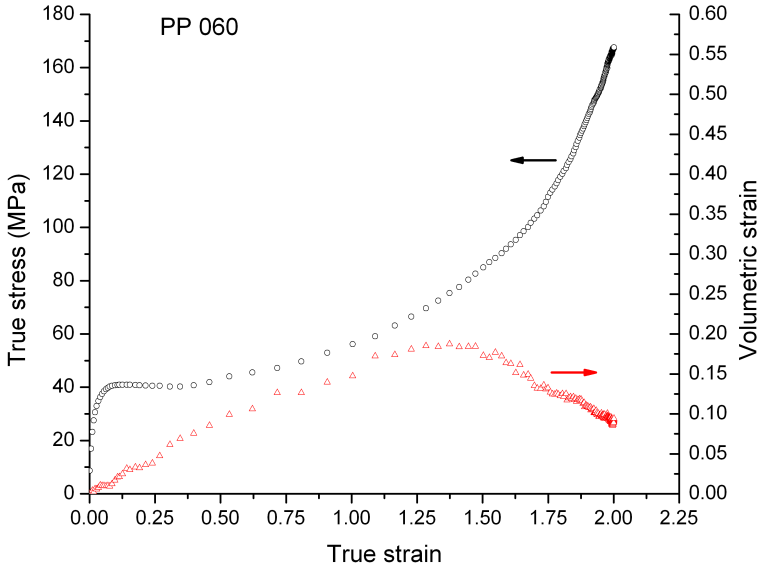

Figure 5.1.1: True stress-true strain and correspondent volumetric strain-true strain diagrams of the PP 060 at constant crosshead rate.

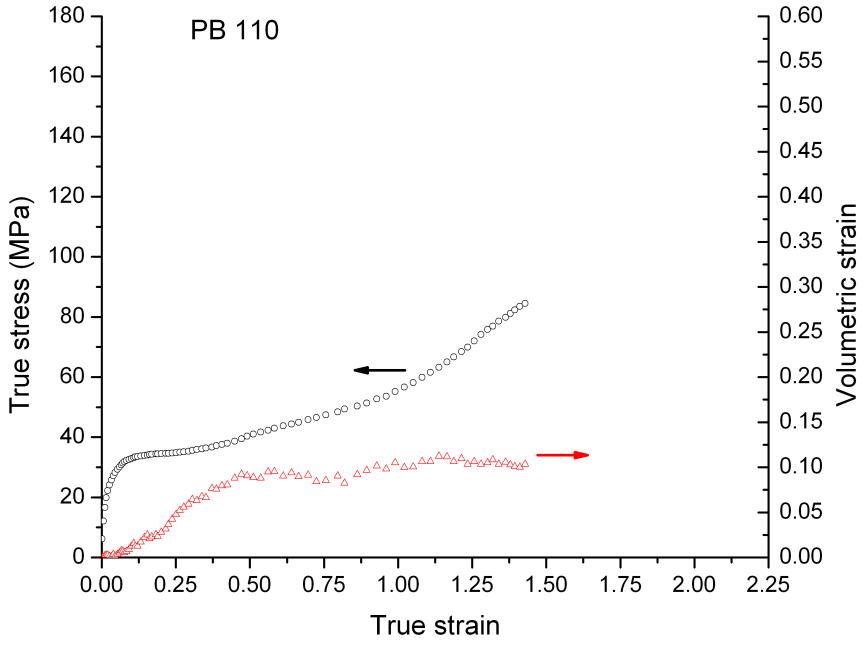

Figure 5.1.2: True stress-true strain and correspondent volumetric strain-true strain diagrams of the PB 110 at constant crosshead rate.

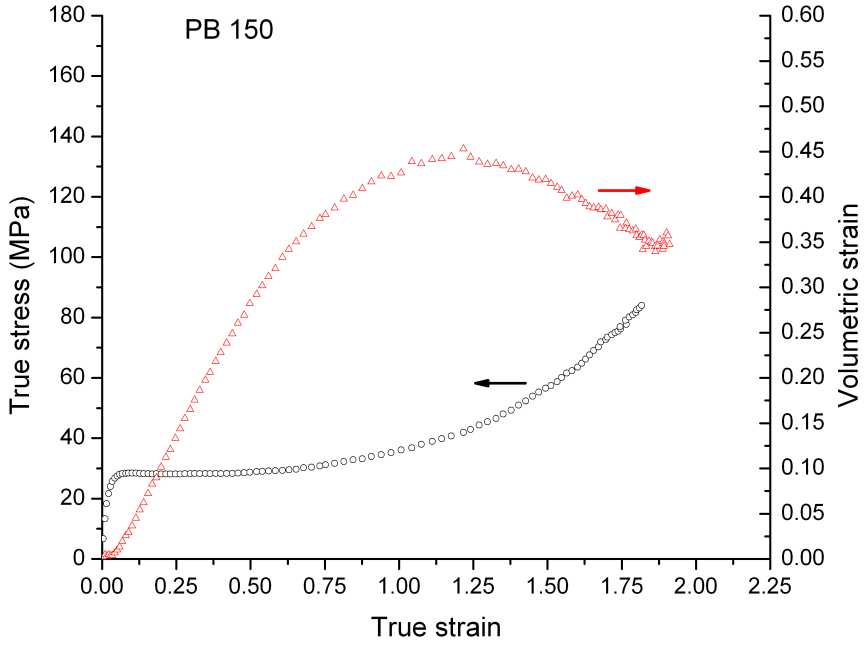

Figure 5.1.3: True stress-true strain and correspondent volumetric strain-true strain diagrams of the PB 150 at constant crosshead rate.

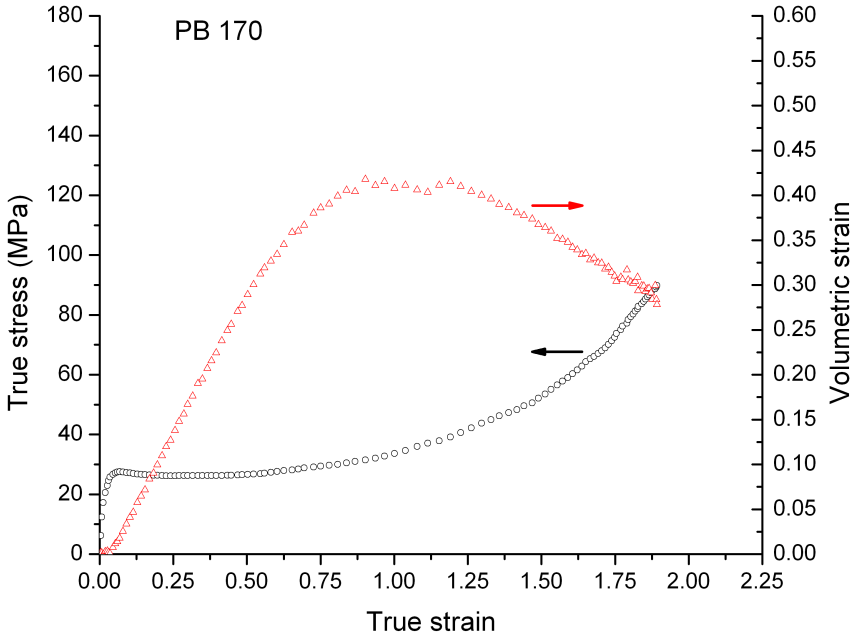

Figure 5.1.4: True stress-true strain and correspondent volumetric strain-true strain diagrams of the PB 170 at constant crosshead rate.

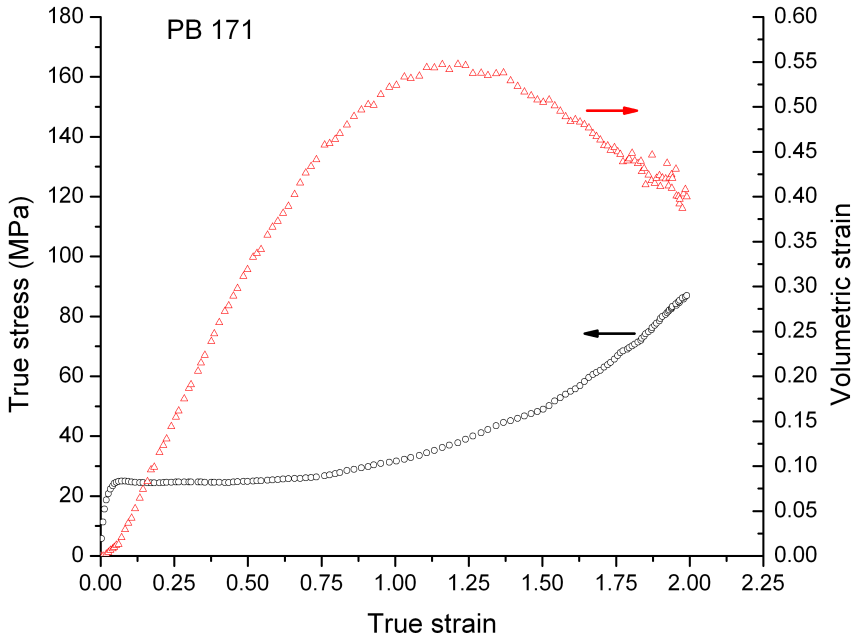

Figure 5.1.5: True stress-true strain and correspondent volumetric strain-true strain diagrams of the PB 171 at constant crosshead rate.

Analyzing the true stress-true strain diagrams of the PP 060 (Figure 5.1.1) some peculiarities can be noticed:

1. The curve is very different from the engineering stress-strain curve of the same material (Figure 5.1.6) which presents a maximum with a subsequently drop of the stress due to the necking of the section of the specimen. On the contrary, the true stress-true strain curve presents, after the yielding, a horizontal section and a final section in which the stress increases again. Moreover, the yielding stress of the true stress-true strain curve is almost the same of the engineering one. In fact, in the elastic zone there is no plastic deformation and thus the cross sectional area does not change. The one represented by the true stress-true strain curve is the real tensile behavior of the material.
2. The true strain experimental points are very separated from each other until the curve reaches a true strain value of 1.5. This is due to the fact that in the polypropylene homopolymer the necking phenomenon is very quick: in a small amount of time the diameter of the specimen in correspondence of the necking passes from 5 mm to 2.5 mm. In this way the true strain increases very fast at the beginning of the curve and thus the experimental points are separated. While, at the end of the curve, the necking area reduction process is slower and so the deformation does not increase so quickly.
3. The material PP 060 presents the highest value of stress in the true stress-strain curve: almost 180 MPa in correspondence of a true strain of almost 2.

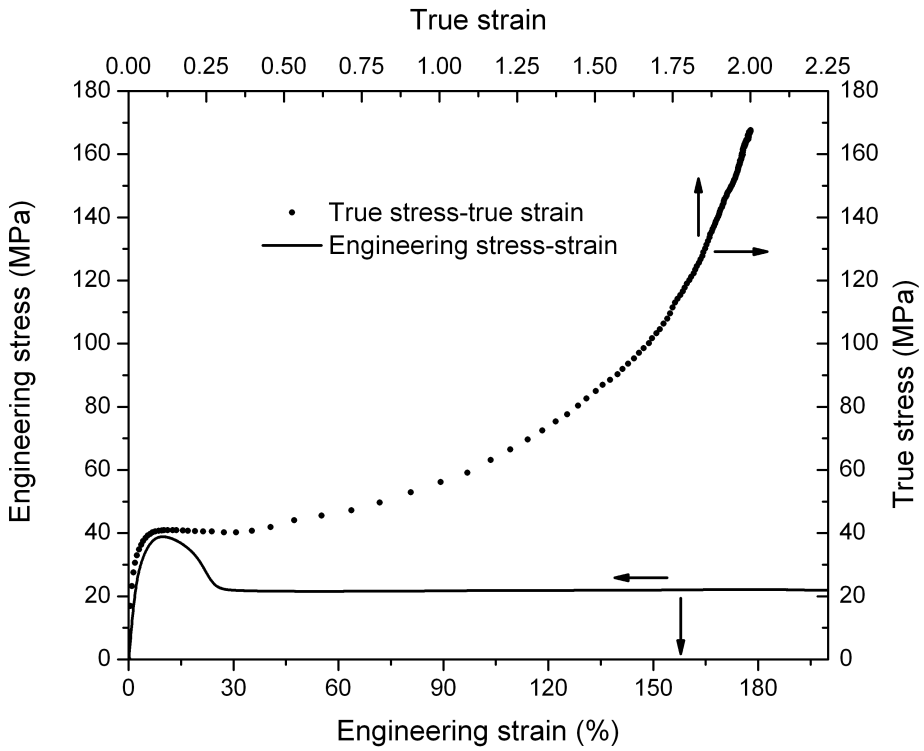

Figure 5.1.6: True stress-true strain and engineering stress-strain curves of the polypropylene PP 060 at constant crosshead rate.

Regarding the PB 110, as explained in paragraph 4.2, the analysis were stopped before the strain reached a value in correspondence of which the peeling phenomenon occurs. As can be seen in Figure 5.1.7 the true stress-true strain diagram is very different from the one of the polypropylene homopolymer. As will be explain later, this material is the only one, among the ones studied in this work, whose curve has this shape. The main difference in the shape of this curve with respect to the one of the polypropylene homopolymer is that after the first maximum (in correspondence of the ending of the elastic phase and the beginning of the plastic one) there is not the horizontal section, which is typical in the other four materials. Instead the curve keeps rising although with a different slope. Moreover, the value of the stress at yield point is lower than the one of the homopolymer and this can be explained by the presence of the ethylene in the material. Finally, the highest value of true stress reached before the peeling phenomenon is lower than the maximum reached by the polypropylene. However, these results are not comparable because the deformation reached is very different and it seems that the trend of the two curves is the same.

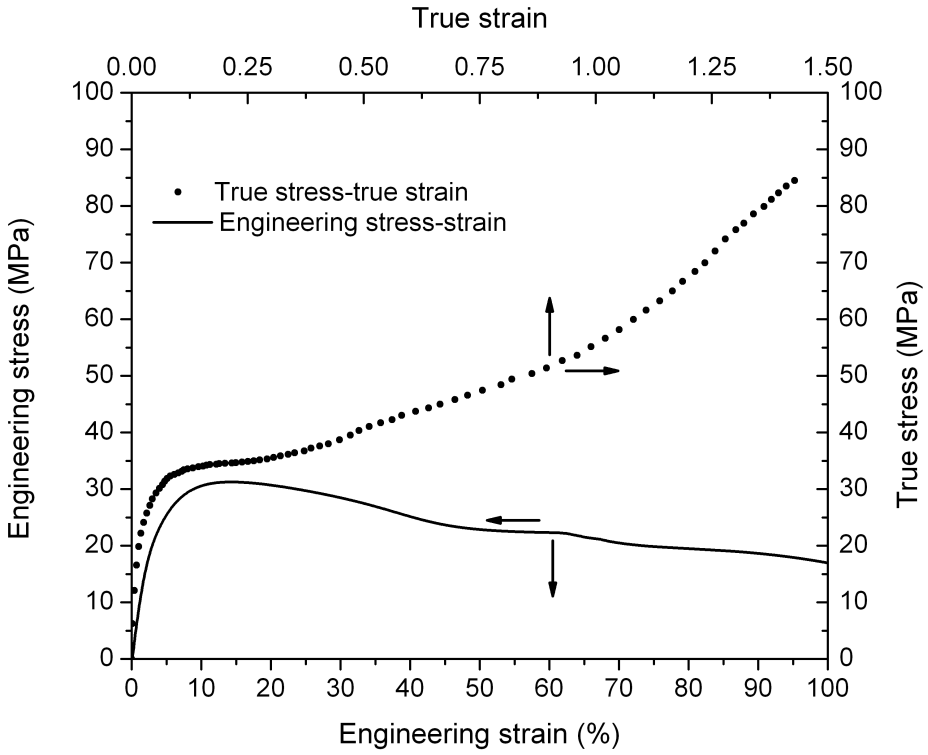

Figure 5.1.7: True stress-true strain and engineering stress-strain curves of the copolymer PB 110 at constant crosshead rate.

Figure 5.1.7 presents the true stress-true strain and the engineering stress-strain diagrams for the copolymer PB 110. In the latter one a drop in the stress can be noticed at a value of deformation of about 65%. This is caused by the peeling phenomenon explained in paragraph 4.2 and it is the strain value in correspondence of which the analysis were stopped.

The last three diagrams (Figure 5.1.3 to Figure 5.1.5) refer to the three higher ethylene content copolymers: PB 150 (8.5%), PB 170 (8.5%) and PB 171 (11.2%). The three behaviors are very similar among each other and the shape of the curve is also similar to the one of the PP 060: the copolymer curves present the same almost horizontal section immediately after the necking. However, the values of true stress for these three copolymers are lower with respect to the values of the homopolymer. Particularly the value of the stress at yield point is just below 30 MPa for the PB 150 and approximately 25 MPa for the PB 170 and the PB 171 while, in the PP 060 curve, this value is almost 45 MPa.

Analyzing the volumetric strain-true strain diagrams (Figure 5.1.1 to Figure 5.1.5) the first characteristic noticed is that, differently from the works previously done and available in literature [14], all of the curves of the materials present two different trends: an increasing trend which ends at a value of true strain between 1.2 and 1.3; and a decreasing trend which starts from this maximum point. Also in this case the PB 110 material deserves a separate discussion since the diagram ends just when the second trend begins. However, with a proper magnification of the scale of the y-axis the two trends can be more easily observed (Figure 5.1.8).

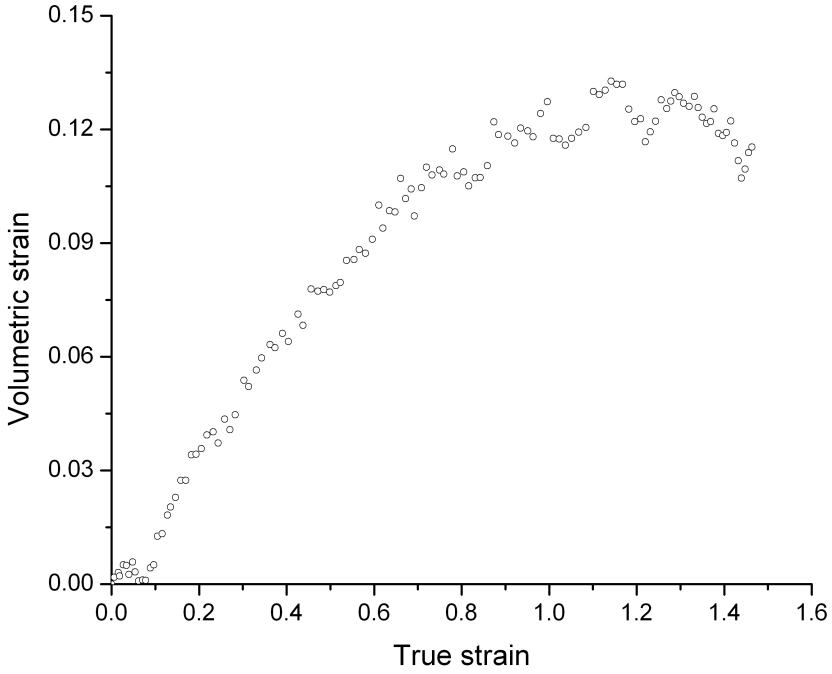

Figure 5.1.8: Volumetric strain-true strain curve of the PB 110.

Another noteworthy characteristic in the volumetric strain-linear strain diagram is the maximum value which seems to be function of the ethylene content. A better analysis of these results will be discussed later in paragraph 5.4.

Finally, looking simultaneously at the two diagrams (true stress-true strain and volumetric strain-true strain) of each material some differences among the five materials can be noticed. In the three copolymers with higher ethylene content diagrams the maximum in volumetric strain almost coincides with the end of the flat section in the true stress-true strain diagram; thus something is happening at this point in the material that cause an increase in the value of stress and a decrease in the value of volumetric

strain. On the contrary, in the other two materials, the maximum value of volumetric strain is located at higher true strain values and it does not seems to be linked with a specific behavior in the correspondent true stress-true strain diagram.

5.2. Constant strain rate tensile tests

As explained in the paragraph 4.2 the constant strain rate tests were carried out not at constant crosshead rate and for each material a crosshead rate profile was found. As previously explained the strain rate has to be constant and has to be almost the same for every material analyzed in such a way that the results can be compared.

Following the crosshead rate profile used for each material and the relative strain rate diagrams are presented (Figure 5.2.1 to Figure 5.2.5).

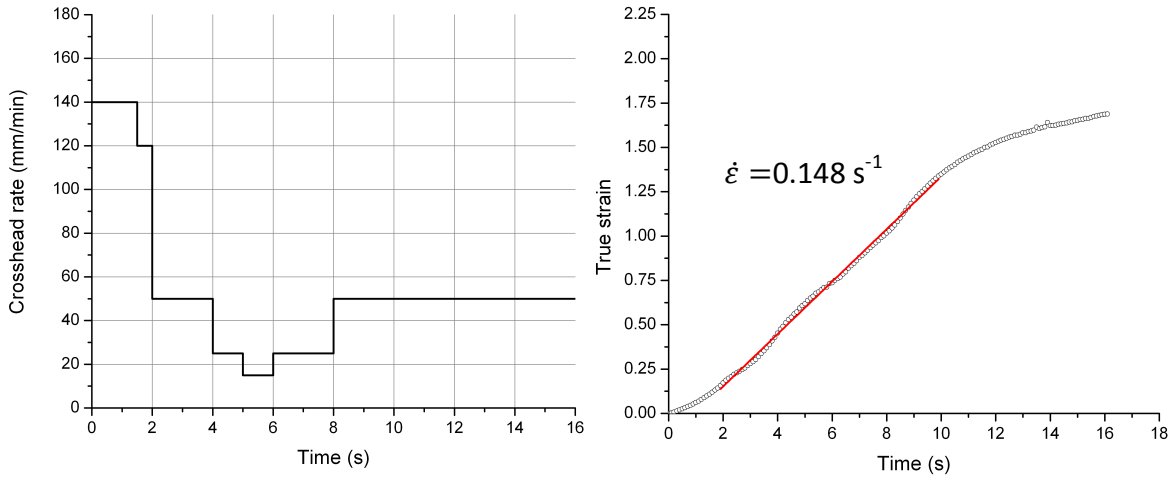

Figure 5.2.1: Crosshead rate profile used in the test of the material PP 060 at constant strain rate and relative strain-time curve.

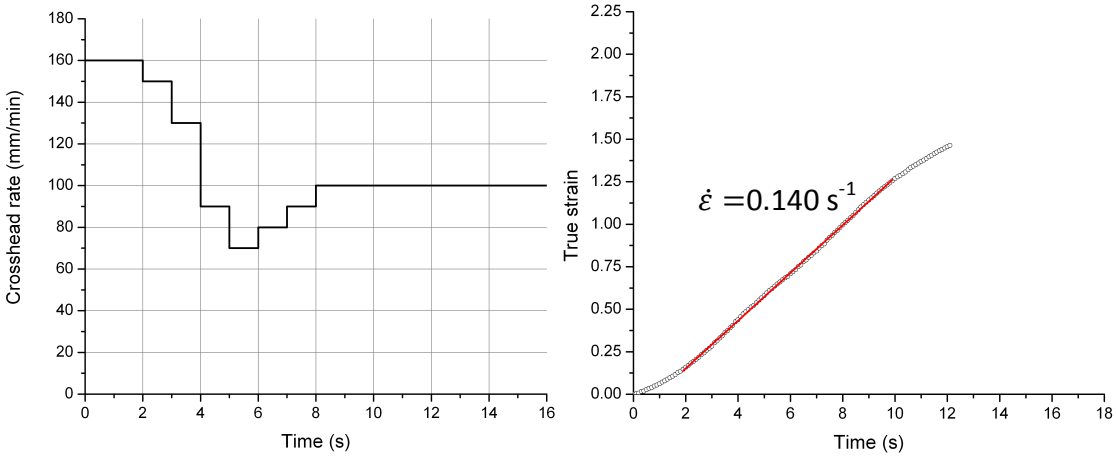

Figure 5.2.2: Crosshead rate profile used in the test of the material PB 110 at constant strain rate and relative strain-time curve.

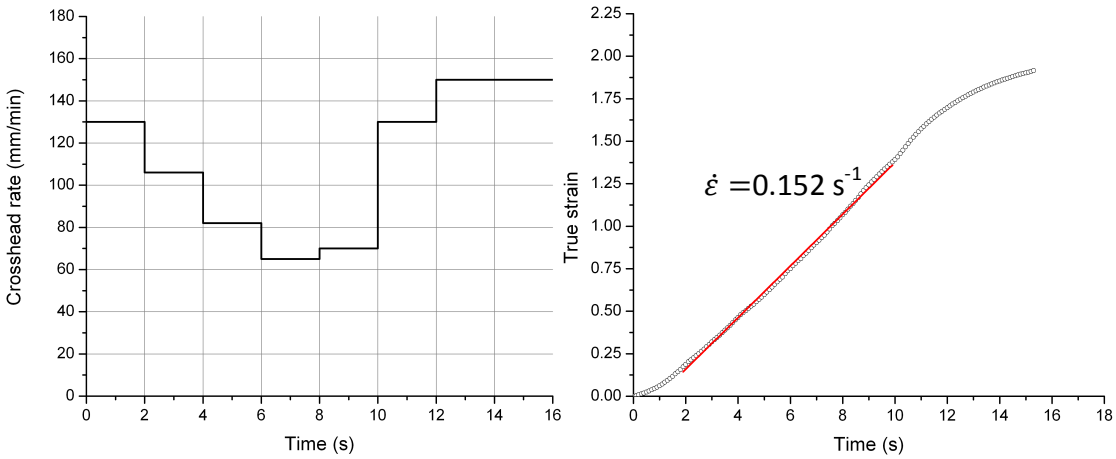

Figure 5.2.3: Crosshead rate profile used in the test of the material PB 150 at constant strain rate and relative strain-time curve.

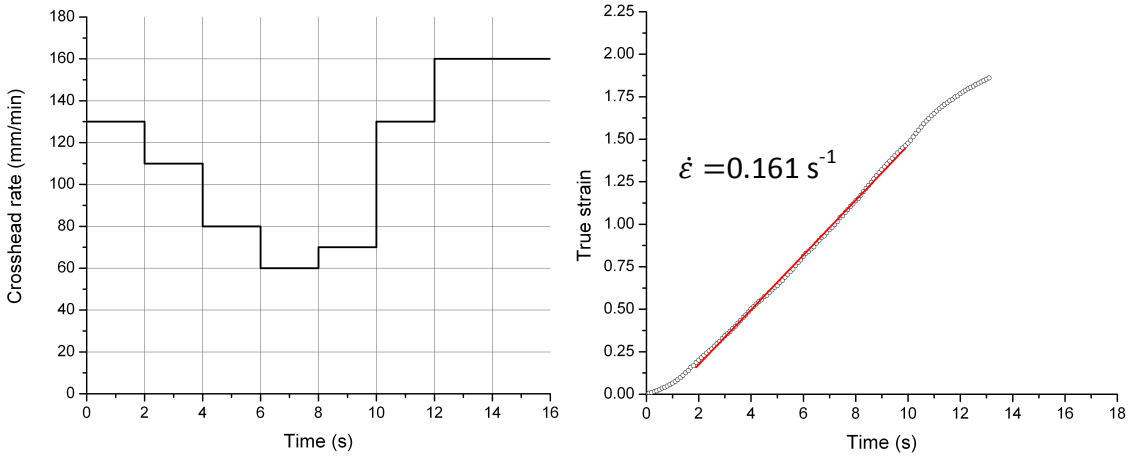

Figure 5.2.4: Crosshead rate profile used in the test of the material PB 170 at constant strain rate and relative strain-time curve.

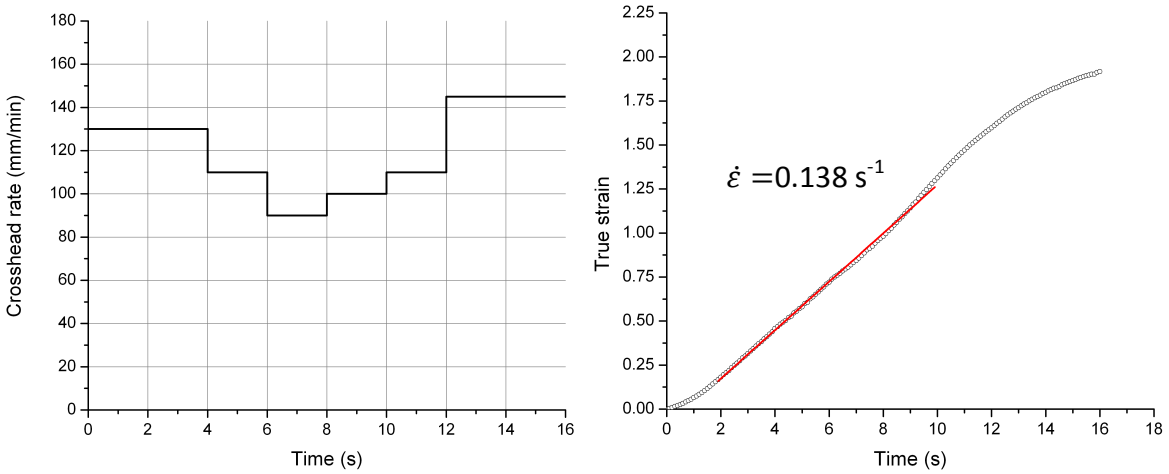

Figure 5.2.5: Crosshead rate profile used in the test of the material PB 171 at constant strain rate and relative strain-time curve.

As can be noticed (Figure 5.2.1 to Figure 5.2.5) the crosshead rate profiles are very different among each other while the value of strain rate (slope of the maximum strain-time curve in the range between 2 and 10 seconds) is comparable in each material. Adopting these profiles the results of the analysis at constant strain rate of the different materials can be compared (Figure 5.2.6).

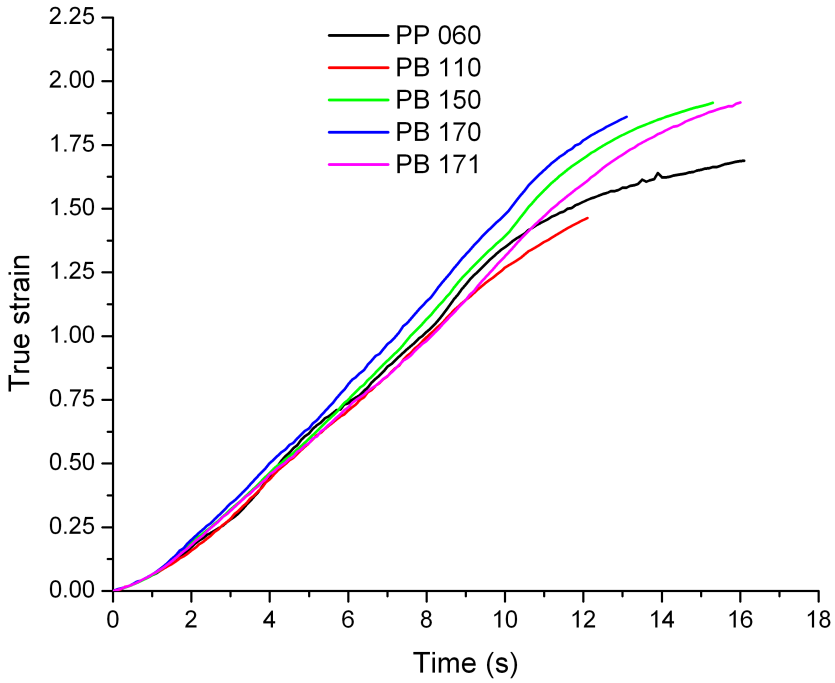

Figure 5.2.6: True strain-time curves of all the materials. The slope of the curves is the strain rate and in the section between the second and the tenth second it is almost the same among the materials.

Figure 5.2.7 to Figure 5.2.11 present the true stress-true strain diagrams and the volumetric strain-true strain diagrams at constant strain rate for, respectively, PP 060, PB 110, PB 150, PB 170 and PB 171.

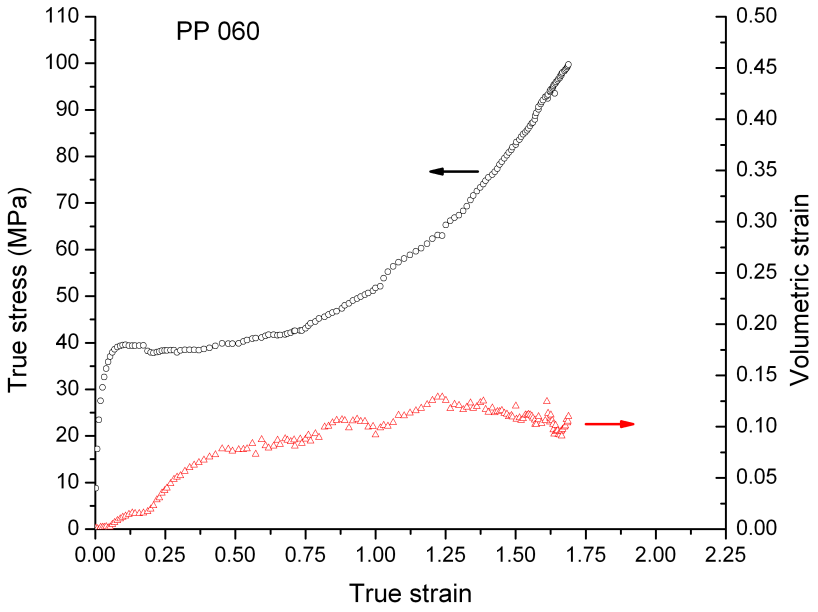

Figure 5.2.7: True stress-true strain and correspondent volumetric strain-true strain diagrams of the PP 060 at constant strain rate.

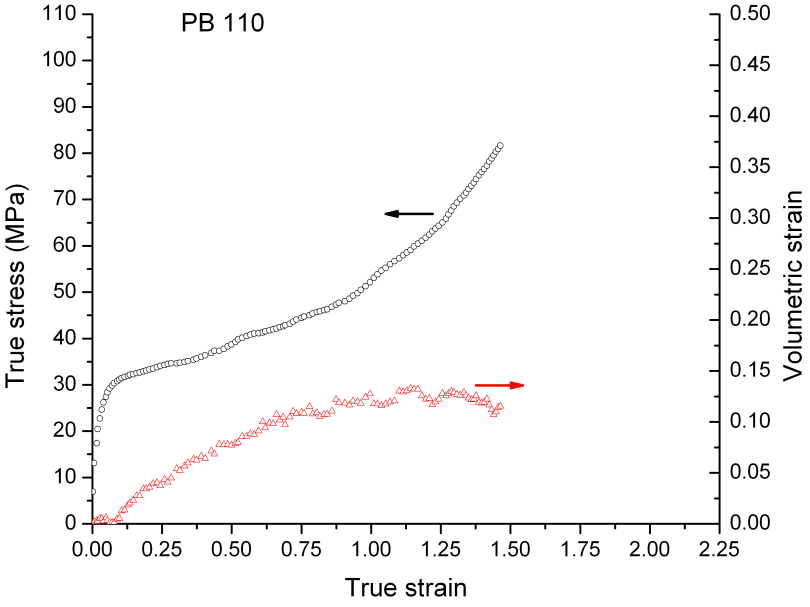

Figure 5.2.8: True stress-true strain and correspondent volumetric strain-true strain diagrams of the PB 110 at constant strain rate.

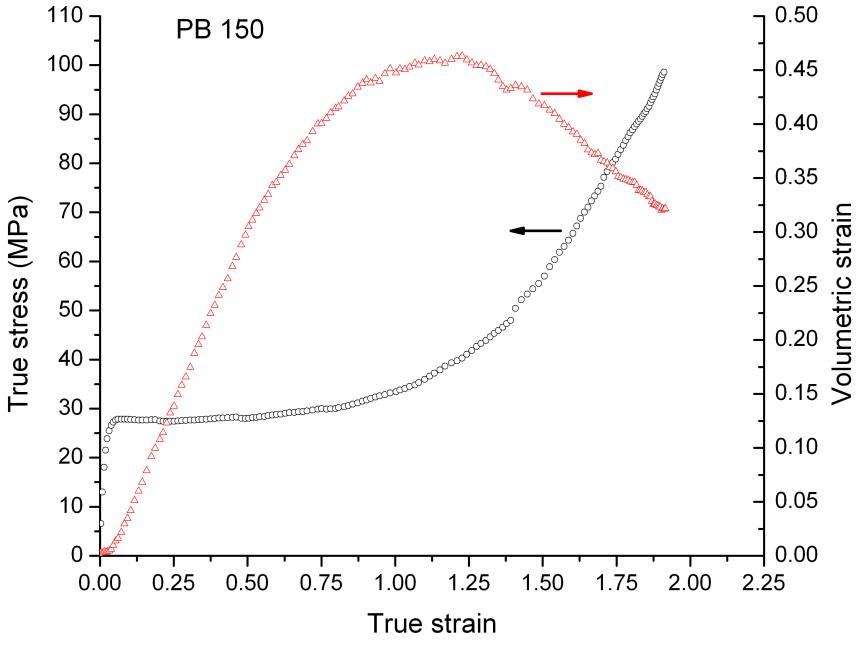

Figure 5.2.9: True stress-true strain and correspondent volumetric strain-true strain diagrams of the PB 150 at constant strain rate.

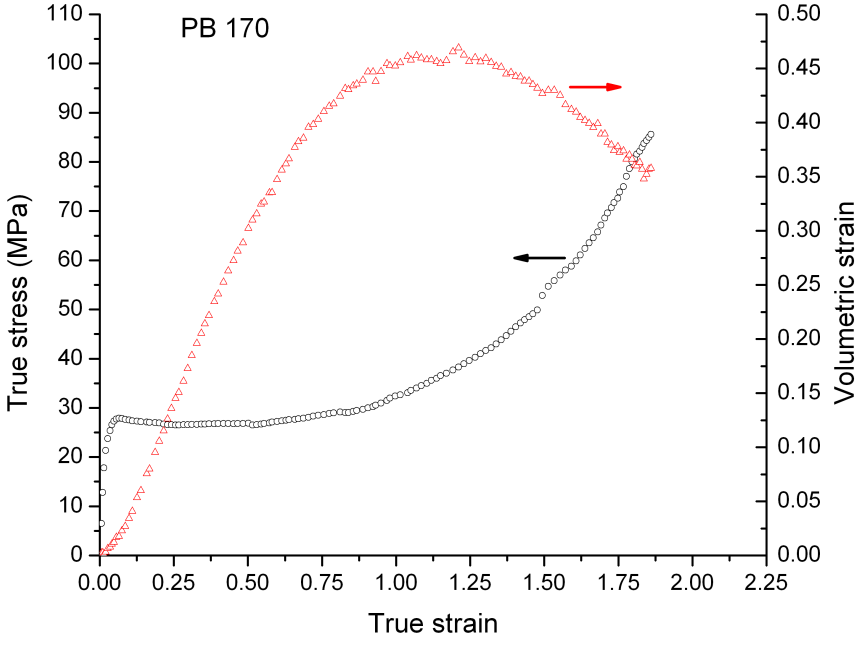

Figure 5.2.10: True stress-true strain and correspondent volumetric strain-true strain diagrams of the PB 170 at constant strain rate.

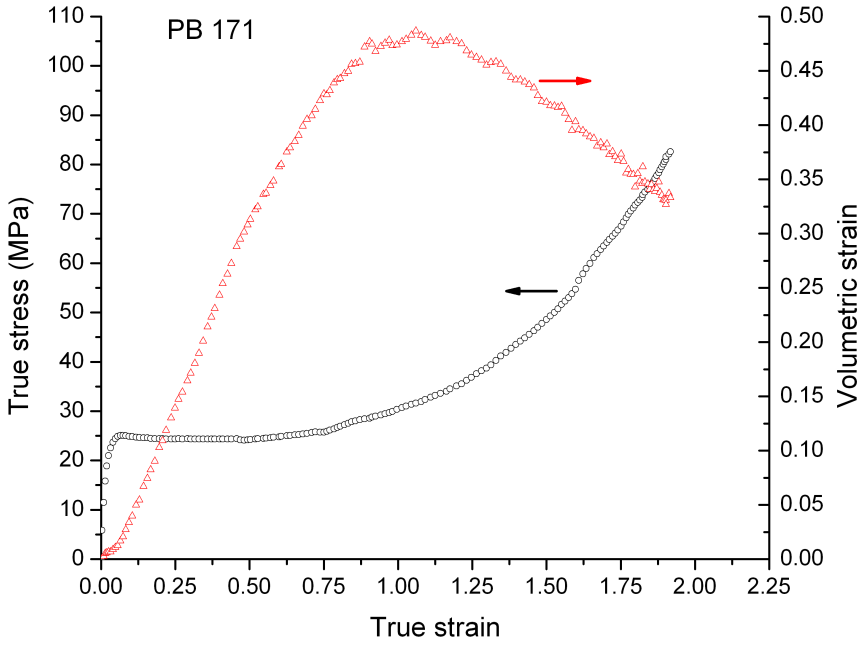

Figure 5.2.11: True stress-true strain and correspondent volumetric strain-true strain diagrams of the PB 171 at constant strain rate.

The shape of the curves is the same of the ones at constant crosshead rate (Figure 5.1.1 to Figure 5.1.5), even though, as can be noticed, the true stress-true strain curves (especially the ones of the PP 060, PB 150 and PB 170) present discontinuity points (jumps in the value of true stress) due to the fact that the crosshead rate suddenly changes in the profile. Furthermore, the volume strain maximum value of the three copolymers with higher ethylene content is lower than the one of the constant crosshead rate tests.

Like in the constant crosshead rate diagrams, also in this case a difference between the behavior of the first two materials (PP 060 and PB 110) and the one of the other three copolymers (PB 150, PB 170 and PB 171) can be noticed. In the three copolymers the maximum of volumetric strain occurs in correspondence of the end of the flat section in the true stress-true strain diagrams while in the homopolymer and in the PB 110 the maximum is located at higher values of deformation and not in correspondence of a specific phenomenon in the stress–strain diagram.

5.3. Differential Scanning Calorimetry analysis

In order to understand which phenomena happen inside the materials during the tensile tests a DSC analysis was performed. Two samples for each material were prepared: one in the undeformed region of the specimen and the second in the center of the deformed zone.

The analysis was performed according to the following procedure: the samples were first heated from 0 °C to 200 °C at a heating rate of 10 °C/min, then they were cooled down at the same cooling rate and finally heated again at the same rate to 200 °C.

Hence, analyzing the first heating step will give the information about the actual state of the sample (undeformed and deformed) while, analyzing the data from the second heating step, will give the information about the material itself.

Figure 5.3.1 presents the DSC melting traces (first heating step) of the undeformed and deformed samples of the polypropylene homopolymer PP 060.

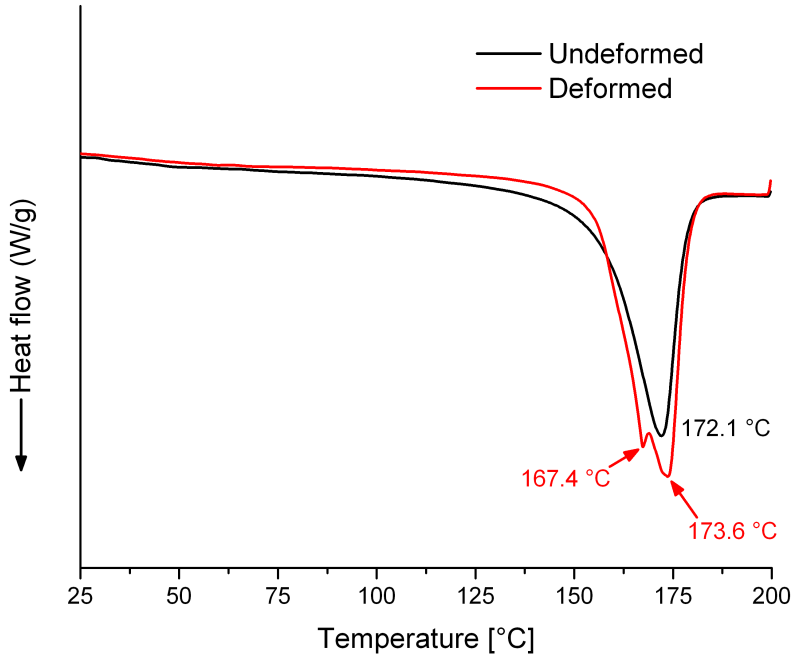

Figure 5.3.1: DSC melting traces of the undeformed and deformed samples of the polypropylene PP 060.

As can be noticed in Figure 5.3.1 the curve of the deformed sample presents two melting temperature while the one of the undeformed sample just one.

When polypropylene is rapidly cooled from the melt state (i.e. in injection molding process) it tends to crystallize as α-phase which presents a melting temperature around 170 °C. The β-phase can be obtained from the α-phase by heating and slowly cooling the material. This phase has a melting temperature which is approximately 10 degrees lower than the one of the α-phase. Thus, observing the DSC curves in Figure 5.3.1 can be assumed that the deformation process caused a partially recrystallization of the α-phase into β-phase. This phenomenon has not been reported in the literature before and is quite interesting but analyzing this aspect is not the aim of this thesis work.

The other three materials analyzed do not present such phenomenon and only have one melting temperature both in the undeformed and deformed state. Table 5.3.1 reports the crystallinity values and melting temperatures before and after the deformation as well as the results of the second heating step. The value of crystallinity has been calculated adopting a value of 165 J/g for the ideal polypropylene with 100% crystallinity according to Wunderlich [28].

Material	Ethylene content	Undeformed state		Deformed state		Second heating step	
		T_m	Crystallinity	T_m	Crystallinity	T_m	Crystallinity
PP 060	0 %	172	61%	174	66%	167	69%
PB 110	6.9 %	168	51%	169	53%	166	55%
PB 170	8.5 %	169	46%	169	55%	165	48%
PB 171	11.2 %	167	42%	168	53%	165	46%

Table 5.3.1: Results of the DSC analysis of the four materials.

The results of the DSC analysis reported in Table 5.3.1 indicate that exist a correlation between the ethylene content of the copolymer and the crystallinity value of the material. For a better understanding of this phenomenon Figure 5.3.2 presents the values of crystallinity and the melting temperature of the materials obtained in the second heating step of the DSC tests.

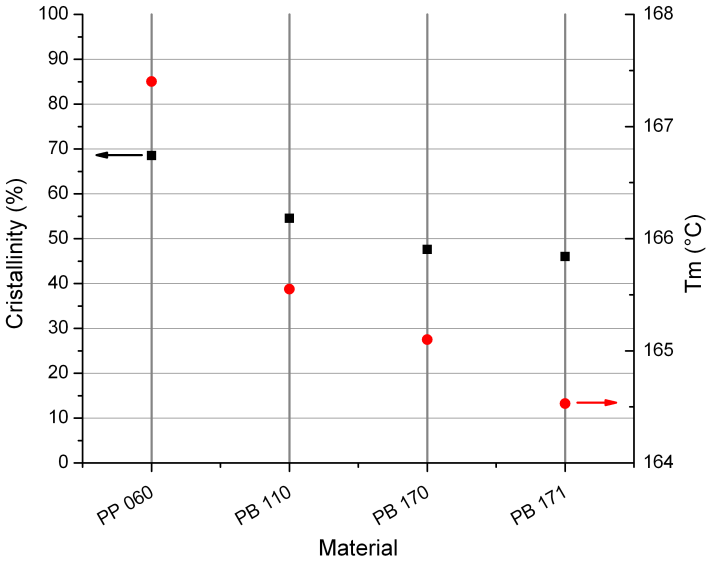

Figure 5.3.2: Crystallinity and melting temperature of the materials analyzed.

Analyzing Figure 5.3.2, can be noticed that also the melting temperature seems to be dependent on the ethylene content; although, the decrease is very low.

Figure 5.3.3 presents the differences in crystallinity between the undeformed and the deformed state of the four materials. All the materials present an increase in crystallinity due to the deformation process. However, also in this case, the PB 110 copolymer presents a different behavior with respect of the other materials: it is the only one that does not present a significant increase in the value of crystallinity due to the deformation process.

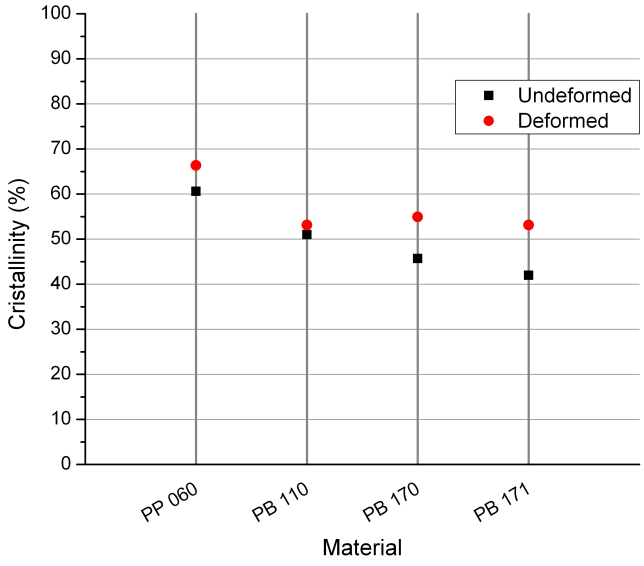

Figure 5.3.3: Crystallinity of the undeformed and deformed samples of the materials analyzed.

5.4. Discussion

In this paragraph the results obtained from the tensile and thermal tests of the five materials will be compared and analyzed. As previously told the mechanical tests were performed both at constant crosshead rate (130 mm/min) and at constant strain rate in the most stressed section of the specimen. Figure 5.4.1 presents the true stress-true strain curves of the materials both at constant crosshead rate and constant strain rate.

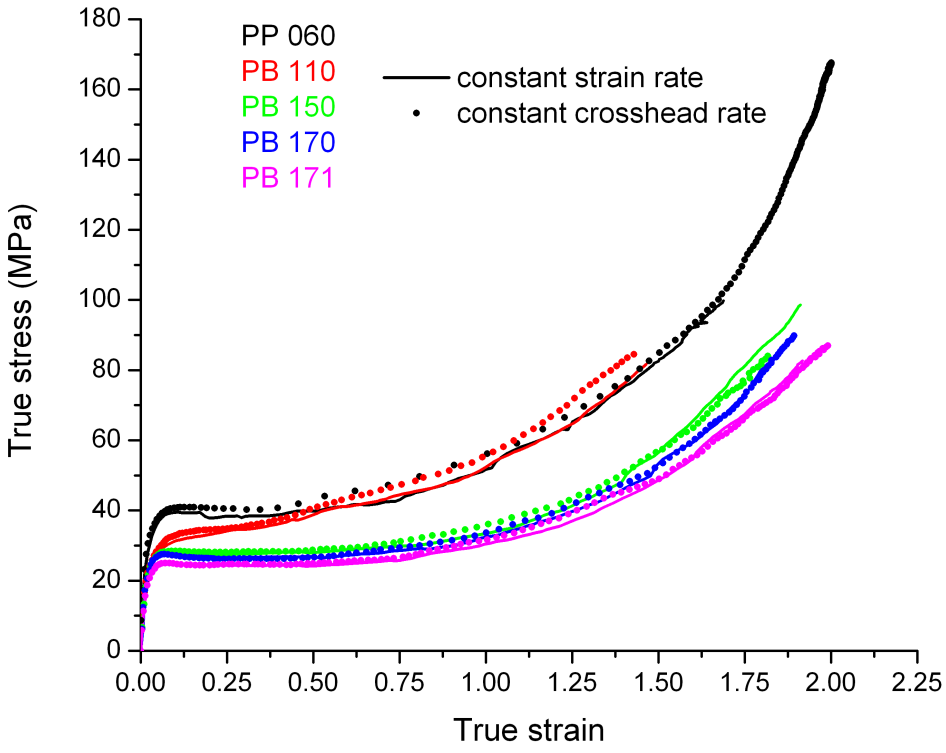

Figure 5.4.1: True stress-true strain curves at constant crosshead rate and constant strain rate of the materials analyzed.

Analyzing Figure 5.4.1 can be noticed that there is no practical difference between the curves. Each material presents the same true stress-true strain behavior at constant crosshead rate and at constant strain rate. Hence, this two different deformation stories do not influence the true stress-true strain behavior of the materials. For this reason, in the following, the discussion of the results will be done analyzing only the constant strain rate curves.

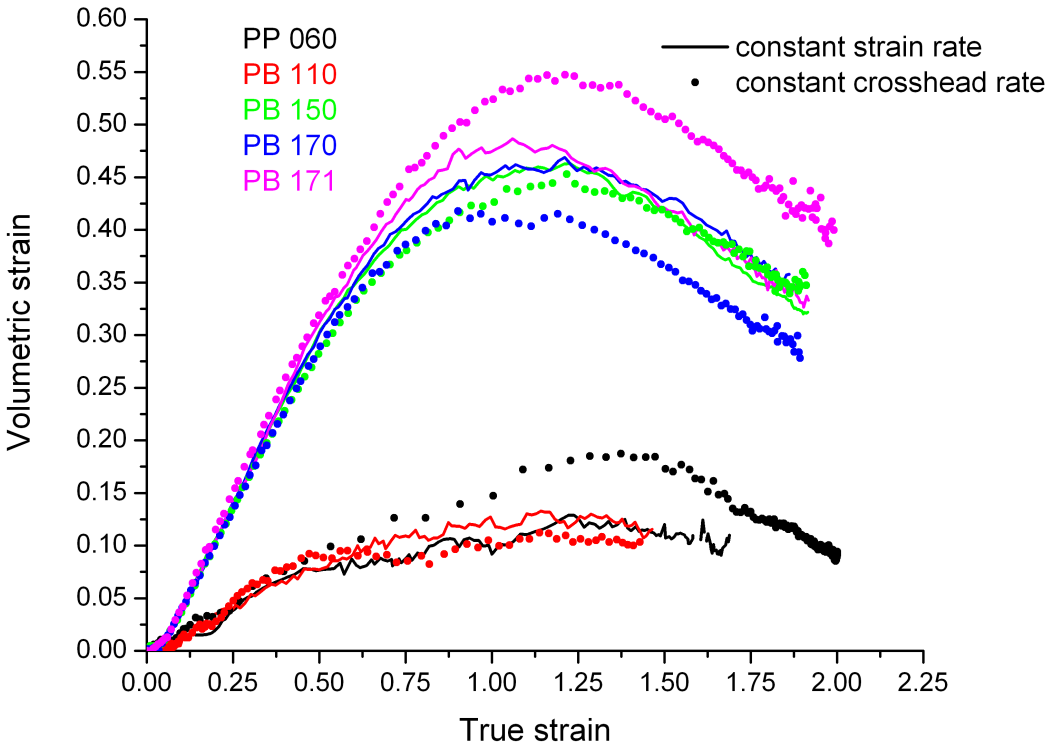

Figure 5.4.2: Volumetric strain-linear strain curves of the materials analyzed at constant crosshead rate and constant strain rate.

Figure 5.4.2 presents the volumetric strain-linear strain curves of the five materials analyzed at constant crosshead rate and constant strain rate. As can be noticed, differently from the true stress-true strain diagram (Figure 5.4.1), in this case the curves at constant crosshead rate are different with respect to the ones at constant strain rate. Only the PB 150 and the PB 110 present the same behavior in the two cases. Hence, the analysis of the volumetric strain-linear strain behaviors will be done, in the following, analyzing the constant strain rate curves. This because the constant strain rate results are more comparable among the materials with respect to the ones at constant crosshead rate.

Table 5.4.1 reports the results of the mechanical tests: the elastic modulus (E) and the yield stress (σ_y).

Material	Ethylene content	M_w	Elastic modulus E [GPa]		Yield stress σ_y [MPa]	
			Mean value	Standard deviation	Mean value	Standard deviation
PP 060	0 %	396000	1.67	0.31	40	0.1
PB 110	6.9 %	816000	1.17	0.12	30	0.1
PB 150	8.5 %	353000	1.28	0.13	28	0.7
PB 170	8.5 %	302000	1.14	0.03	28	0.4
PB 171	11.2 %	307000	1.07	0.19	25	0.5

Table 5.4.1: Elastic modulus and yielding stress of the materials analyzed.

The true stress-true strain behavior and the mechanical values of the materials analyzed deserves some considerations.

Firstly, the yield stress value seems to be related with the ethylene content in the material. Starting from the top, the homopolymer presents a yield stress value of 40 MPa; subsequently the copolymer PP 110, which contains 6.9 % of ethylene, presents 30 MPa of yield stress; the two copolymers (PB 150 and PB 170) with a ethylene content of 8.5 % present a value of stress of 28 MPa; and finally, the PB 171 copolymer which contains 11.2 % of ethylene presents the lowest yield stress value: 25 MPa.

Secondly, the final stress value seems to be greater influenced by the ethylene content rather than the molecular weight. In fact, confronting the curves of the two copolymers PB 150 and PB 170, which have the same ethylene content but different molecular weight (350000 for the PB 150 and 300000 for the PB 170) no great difference can be noticed; while, between the PB 170 and the PB 171, which have the same molecular weight but different ethylene content (8.5 % for the PB 170 and 11.2 % for the PB 171), a difference in the behavior can be noticed. The curve of the material with the highest content in ethylene presents lower stress values than the one of the other copolymer.

As for the copolymer PB 110, which presents the largest molecular weight among the analyzed materials and 6.9 % of ethylene content it has to be noticed that its behavior is very similar to the one of the polypropylene homopolymer, and this is attributed, as will be seen below, to its high molecular weight.

Table 5.4.2 presents the results of the volumetric strain analysis: the maximum value of volumetric strain (ε_v), the correspondent true linear strain (ε_{true}) and the value of the difference between the volumetric strain at the maximum point and the one at true strain of 1.47 ($\Delta\varepsilon_v$). This value of deformation was chosen arbitrarily because was the maximum value reached by the PB 110 before the peeling phenomenon happened.

Material	ε_v maximum		ε_{true} (ε_v max)		$\Delta\varepsilon_v$	
	Mean value	Standard deviation	Mean value	Standard deviation	Mean value	Standard deviation
PP 060	0.13	0.02	1.29	0.08	0.02	0.01
PB 110	0.13	0.01	1.29	0.02	0.01	0.00
PB 150	0.47	0.02	1.17	0.08	0.05	0.02
PB 170	0.48	0.01	1.16	0.05	0.04	0.01
PB 171	0.49	0.03	1.06	0.07	0.07	0.01

Table 5.4.2: Maximum value of volumetric strain, the correspondent true linear strain value and the difference between the volumetric strain at the maximum point and the one at true strain of 1.47 of the materials analyzed.

For a better understanding of the volumetric strain-linear strain diagram, Figure 5.4.3 presents the curves at constant strain rate for each material. As can be noticed, the differences among the different materials, which were evidently in the tests at constant crosshead rate (Figure 5.4.2), seem to disappear. Hence, only two behaviors are observed: the one of the three high ethylene content copolymers and the one of the homopolymer and the PB 110 copolymer.

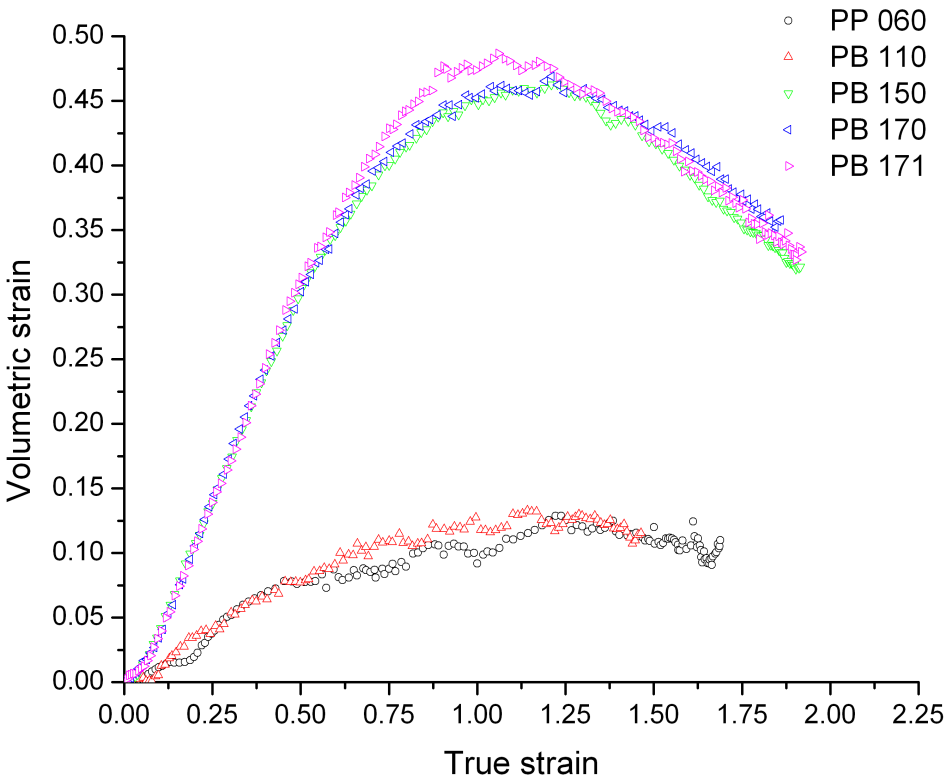

Figure 5.4.3: Diagram of the volumetric strain-linear strain curves at constant strain rate of all the materials analyzed.

Analyzing Figure 5.4.3 some peculiarities can be noticed.

Firstly, all the materials show a common behavior in the first section of the curve. Figure 5.4.4 presents a magnification of this section: two different trends in the curves can be noticed. A first one, until the true strain reached a value of almost 0.05, in which the slope of the curve is lower and a second one, starting from the yield point, with a higher slope.

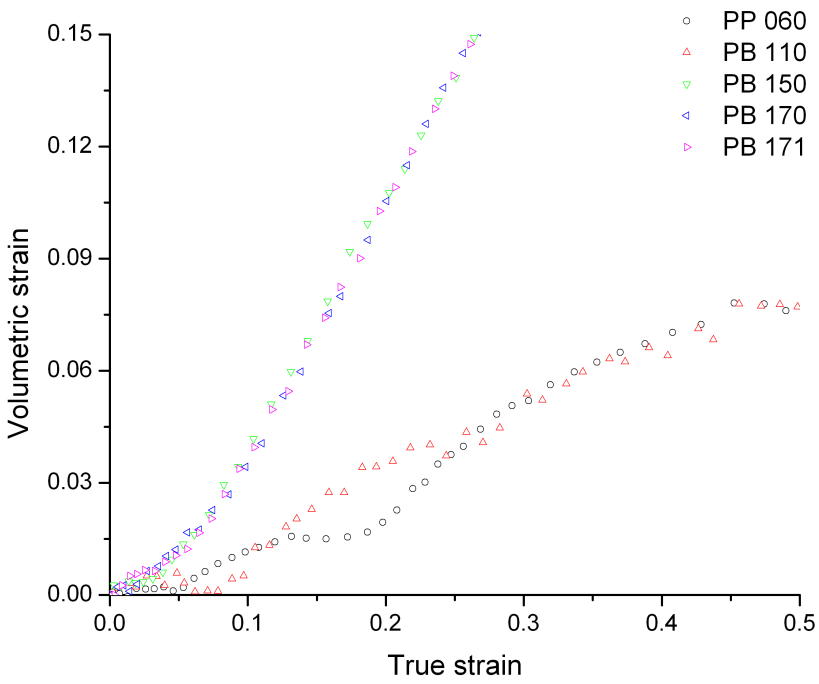

Figure 5.4.4: Magnification of the first section of the volumetric strain-linear strain diagram.

As can be seen in Figure 5.4.5 and Figure 5.4.6, the change in the slope of the volumetric strain-true strain curves seems to occur when the material passes from the elastic zone to the plastic one (yielding phenomenon). This different behavior can be related to the fact that in the elastic zone (before yielding) volumetric changes are due to elastic expansion of the material (Poisson's ratio < 0.5) and amorphous chains compaction [3]. The latter mechanism, reported for polypropylene in other works [20], gives rise to volume contraction and so the total volume strain is very low.

This behavior is remarkable in the polypropylene and in the PB 110 which present a very low slope in the first part of the curve: the value of the volumetric strain is practically zero until the yield point ($\varepsilon_{true} \approx 0.05$) (Figure 5.4.5).

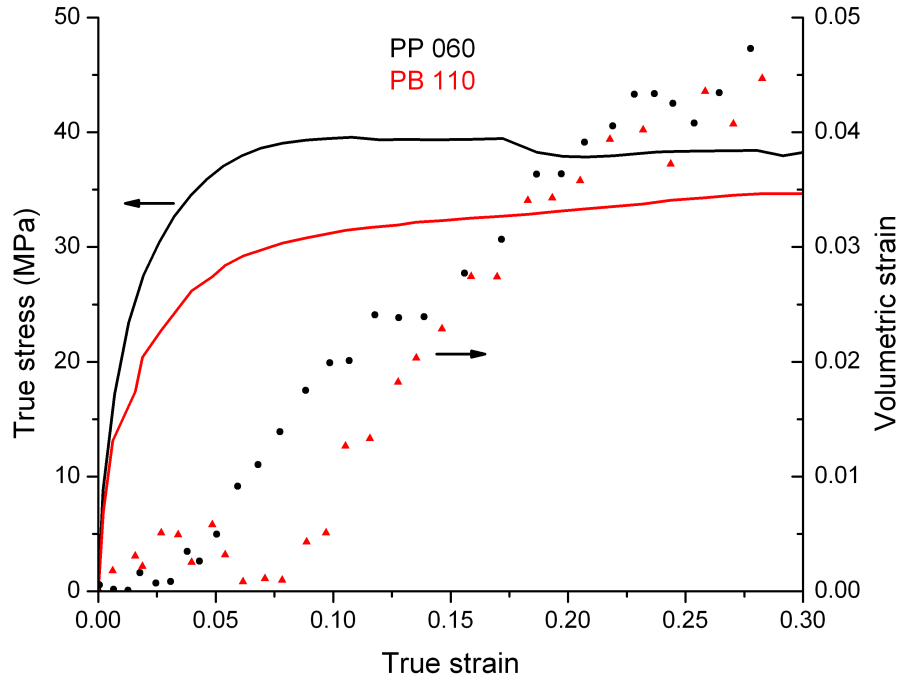

Figure 5.4.5: Change in the slope of the volumetric strain-linear strain curves of the polypropylene homopolymer and the copolymer PB 110 at yield point.

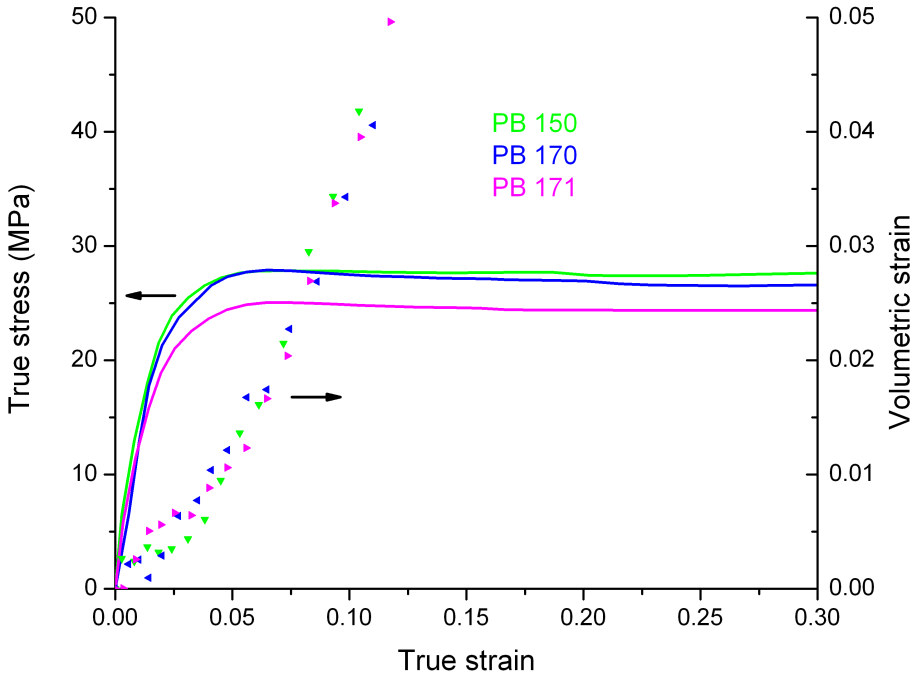

Figure 5.4.6: Change in the slope of the volumetric strain-linear strain curves of the three copolymers with the highest ethylene content at yield point.

A second feature which can be noticed analyzing Figure 5.4.3 is the different behavior among the materials: the homopolymer and the PB 110 which present a volumetric strain-true strain curve with a low maximum value, while the other materials present a

higher value of maximum volumetric strain (almost 3 times higher). In literature the value of volume deformation of the polypropylene seems to be related to different parameters: temperature, strain rate, microstructure of the material, crystalline phases (α, β or γ-phase), dimensions and shape of the spherulites and of the lamellae. Changing the microstructure caused a change in the plastic deformation phenomenon which occurs during the tensile test i.e. β–phase crystals are more "ductile" with respect of the α-phase one and so a polypropylene rich in β–phase crystals does not present crazing during deformation; thus the volumetric strain is lower [4, 29].

All the results presented in literature suggest a value of the volumetric strain for the polypropylene much higher than the one obtained in this work. The typical maximum value of volumetric strain is around 0.5 while the one obtained in this work is 0.15. It seems that this discrepancy can be attributed to the presence, in the polypropylene analyzed, of low molecular weight fractions. As explained in paragraph 2.1.1, one of the mechanisms of plastic deformation occurring in the polypropylene is cavitation. Cavitation is a high increasing volume process of deformation which is nucleated in the free volume fraction of the amorphous phase of the material. Low molecular weight molecules may cause a lower free volume and, as a result, a suppression of the cavitation process is observed [30]. Thus, the lower value of volume strain observed in this thesis work can be related with the presence of low molecular weight fractions in the commercial material analyzed which were not removed before testing as has been done in other works [30, 31].

The behavior of the PB 110 is not easy to understand and explain; this material, because of its composition, should behave as the other three copolymers: a high value of volumetric strain followed by a marked decrease of the deformation. Nevertheless, it behaves like the polypropylene homopolymer: a low maximum value of volumetric deformation with a small decrease at high strains. The different behavior could be due to its very high molecular weight.

The PB 110 presents a molecular weight which is almost twice the value relevant to the homopolymer and three times the value of the other copolymers. As explained in paragraph 2.1.2 failure in ethylene-propylene block copolymers is related to the

dispersed elastomeric particles. In fact, upon loading, small cavities are nucleated either within the particles or at weak points such as the boundary between the particles and the PP matrix. These voids can be stabilized by fibrillar bridges of polypropylene filaments within the particles which are plastically deformed and orientated. It has been shown [32] that these fibrillar bridges are stronger the greater the molecular weight of the material. Thus, the PB 110 which presents a very high molecular weight could present a low volume strain due to this fact.

The three copolymers with the higher ethylene content present a similar volumetric strain-true strain curve but very different from that of the other two materials. The maximum value of volume strain is almost 0.5 (while for the other two materials it is 0.13) and after the maximum the curves displays a significant negative slope. As explained in paragraph 2.1.2 the deformation mechanism of ethylene-propylene block copolymers is based on the cavitation phenomenon. This phenomenon takes place inside the inclusions and in the amorphous phase of the polypropylene matrix. The combination of these two cavitation phenomena causes a marked increase in the volume of the material.

Finally, the shape of the curves in Figure 5.4.3 presents two trends: a first increasing trend until the true strain reaches a value of about 1.2 (depending on the material) and a second decreasing trend at higher strain. Regarding this behavior no such trend has been reported in the literature. In the works found [3, 13, 14, 20, 23] the authors analyze the behavior up to much lower strain values. However, the decrease in the volume strain coul be related with recrystallization. In support of this idea are the results of the DSC analysis (Table 5.3.1 and Figure 5.3.3) from which an increase of the crystallinity after the tensile test for all the materials was observed. This increment is higher for the copolymers with respect to the polypropylene homopolymer (Figure 5.3.3). The only exception is presented by the PB 110 which presents practically the same value of crystallinity in the undeformed and deformed state and whose volumetric strain-true strain curve does not present a marked decreasing trend after the maximum (Figure 5.4.3). This is probably due to the fact that it was not possible to carry out the tests up to high strains (paragraph 4.2).

Chapter 6. Conclusions

The first objective of this work was to suitably apply a 3D DIC technique, which allows the measurement of the three components of the strain in a cylindrical specimen made of highly deformable polymers (polypropylene and ethylene-propylene copolymers) up to high strains.

To apply this technique different issues had to be solved and, finally, a solution which allows the measurement of the three component of the true strain up to a value of approximately 2 has been set up. The main feature of this technique is that it exploits a double analysis obtaining the final results by summing the partial results of the two analysis.

Once the technique was developed, the true stress-true strain and the volumetric strain-true strain curves for the five materials were analyzed.

As for the true stress-true strain curve, the results indicate that there are two main behaviors: one for the polypropylene homopolymer (PP 060) and the other one for the three high ethylene content copolymers. The shape of the curve of the two behaviors is similar but the stress values for the homopolymer are higher compared to those of the three copolymers. As expected, there is also a correlation between yield stress and the ethylene content in the material: the higher the ethylene content the lower the yield stress. This is due to the presence of dispersed low modulus rubber particles in the material.

As for the volumetric strain, for all materials this curve shows a maximum as a function of strain. Moreover, also in this case, like in the true stress-strain analysis, two different behaviors can be identified: the one of the polypropylene homopolymer and the one of the three high ethylene content copolymers. The main difference in the two behaviors is that the three copolymers present volumetric strains higher than those of the homopolymer. This fact can be related to the different deformation mechanisms taking place in the materials.

In the polypropylene the deformation mechanism is due to different phenomena [2, 3]: at low strain elastic expansion (Poisson's ratio < 0.5) ($\Delta V>0$) and strain induced reorganization of the amorphous phase in the interlamellar zones ($\Delta V<0$); then strain of molecular chains in the interlamellar amorphous phase which is accompanied by lamellae separation, rotation of lamellar stacks and interlamellar shear ($\Delta V>0$); at the yield point the crystalline order destruction begins because of the activated fragmentation among the crystallites and the crystal structure begins to transform into a fibrillar structure ($\Delta V>0$); finally, at higher strains cavitation is the main cause of dilatation ($\Delta V>0$).

In the copolymers the overall behavior is similar but the cavitation phenomenon is more pronounced because it takes place also inside the dispersed rubbery phase and at the interface between the dispersed particles and the polypropylene matrix. Thus, a higher value of volumetric strain is expected in the latter materials.

Moreover, the volumetric strain-linear strain of all the materials analyzed, presents two trends: an increasing trend until a certain value of true strain after which a decreasing trend is observed. A possible explanation of the fact that the volumetric deformation decreases at high linear strains is that recrystallization occurs. This is due to the fact that at very high strain the molecular chains of the polymer are oriented in the loading direction favoring further crystallization. This hypothesis was supported by the DSC analysis which indicated an increase in the crystallinity on the deformed specimen with respect to the undeformed ones.

The lower ethylene content copolymer PP 110 despite being a propylene-ethylene block copolymer, presents a behavior very similar to the one of the homopolymer and this was related to its very high molecular weight.

Chapter 7. References

1. Clive Maier, T.C., *Polypropylene. The definitive user's guide and databook.*1998: Plastic Design Library.
2. Andrzej Pawlak, A.G., *Cavitation during Tensile Deformation of Polypropylene.* Macromolecules, 2008. **41**: p. 2839-2851.
3. Frederic Addiego, A.D., Christian G'Sell, Jean-Maria Hiver, *Characterization of volume strain at large deformation under uniaxial tension in high-density polyethylene.* Polymer, 2006. **47**: p. 4387-4399.
4. M. Aboulfaraj, C.G.S., B. Ulrich, A. Dahoun, *In situ observation of the plastic deformation of polypropylene spherulites under uniaxial tension and simple shear in the scanning electron microscope.* Polymer, 1995. **36**(4): p. 731-742.
5. Karger-Kocsis, J., *Polypropylene: structure, blends and composites. Copolymers and blends.*1994: Chapman & Hall.
6. Chunhui Zhang, Y.S., Ruifen Chen, Yuanzhi Wu, Feng Chen, Qiang Zheng, Guohua Hu, *Morphology, microstructure and compatibility of impact polyèpropylene copolymer.* Polymer, 2010. **51**: p. 4969-4977.
7. Hongshend Tan, L.L., Zhineng Chen, Yihu Song, Qiang Zheng, *Phase morphology and impact toughness of impact polypropylene copolymer.* Polymer, 2005. **46**: p. 3522-3527.
8. Chunhui Zhang, Y.S., Ruifen Chen, Qiang Zheng, *Study on thermal behavior of impact polypropylene copolymer and its fractions.* Journal of Applied Polymer Science, 2010.
9. G.-M. Kim, G.H.M., M. Gahleitner, J. Fiebig, *Relationship between morphology and micromechanical toughening mechanisms in modified polypropylenes.* Journal of Applied Polymer Science, 1996. **60**: p. 1391-1403.
10. G.-M. Kim, G.H.M., *Micromechanical deformation processes in toughened and particle-filled semicrystalline polymers. Part 1: Characterization of deformation processes in dependence on phase morphology.* Polymer, 1998. **39**(23): p. 5689-5697.

11. G.-M. Kim, G.H.M., *Micromechanical deformation processes in toughened and particle filled semycristalline polymers. Part 2: Model representation for micromechanical deformation processes.* Polymer, 1998. **39**(23): p. 5699-5703.
12. P. Doshev, R.L., G. Lohse, A. Heuvelsland, W. Grellmann, H.-J. Radusch, *Fracture characteristics and deformation behavior of heterophasic ethylene-propylene copolymers as a function of the dispersed phase composition.* Polymer, 2005. **46**: p. 9411-9422.
13. C. G'sell, J.M.H., A. Dahoun, *Experimental characterization of deformation damage in solid polymers under tension, and its interrelation with necking.* International Journal of Solids and Structures, 2002.
14. C. G'sell, S.L.B., J.M. Hiver, *Polypropylene/polyamide 6/polyethylene-octene elastomer blends. Part 2: volume dilatation during plastic deformation under uniaxial tension.* Polymer, 2004.
15. J. Mohanraj, D.C.B., I.M. Ward, A. Dahoun, J.M. Hiver, C. G'Sell, *Plastic deformation and damage of polyoxymethylene in the large strain range at elevated temperatures.* Polymer, 2006.
16. O. De Almeida, F.L., J. Brillaud, *Analysis by a 3D DIC technique of volumetric deformation gradients: Application to polypropylene/EPR/talc composites.* Composites, 2008.
17. Qin-Zhi Fang, T.J.W., H.G. Beom, H.P. Zhao, *Rate-dependent large deformation behavior of PC/ABS.* Polymer, 2009.
18. F. Grytten, H.D., M. Polanco-Loria, S. Dumoulin, *Use of digital image correlation to measure large-strain tensile properties of ductile thermoplastics.* Polymer Testing, 2009.
19. Roylance, D., *Stress-Strain Curves*, 2001, Department of Materials Science and Engineering Massachusetts Institute of Technology: Cambridge.
20. J.M. Gloaguen, J.M.L., *Plastic deformation behaviour of thermoplastic/clay nanocomposites.* Polymer, 2001.
21. P. François, J.M.G., B. Hue, J.M. Lefebvre, *Volume strain measurements by optical extensometry: application to the tensile behavior of RT-PMMA.* Journal de Physique III, 1994.

22. E. Parsons, M.C.B., D.M. Parks, *An experimental investigation of the large-strain tensile behavior of neat and rubber-toughened polycarbonate.* Polymer, 2004.
23. E.M. Parsons, M.C.B., D.M. Parks, M. Weinberg, *Three-dimensional large-strain tensile deformation of neat and calcium carbonate-filled high-density polyethylene.* Polymer, 2005. **46**: p. 2257-2265.
24. Qin-Zhi Fang, T.J.W., Hui-Min Li, *Large tensile deformation behavior of PC/ABS alloy.* Polymer, 2006.
25. M. Jerabek, Z.M., R.W. Lang, *Strain determination of polymeric materials using digital image correlation.* Polymer Testing, 2010.
26. Segovia, A., *Integridad estructural de grados de copolimeros etileno-propileno procesados por diferentes métodos de transformación*, 2008, Universitat Politècnica de Catalunya: Barcelona.
27. *Aramis User-Manual Software*, 2010, GOM Optical Measuring Techniques.
28. Wunderlich, B., *Macromolecular Physics, Volume 3: Crystal Melting*. Vol. 3. 1980, New York: Academic Press.
29. Bing Na, R.L., Wenfei Xu, *Effect of network relaxation on void propagation and failure in isotactic polypropylene at large strain.* Journal of Applied Polymer Science, 2009. **113**: p. 4092-4099.
30. Artur Rozanski, A.G., *Controlling cavitation of semicrystalline polymers during tensile drawing.* Macromolecules, 2011. **44**: p. 7273-7287.
31. A. Rozanski, A.G., M. Debowska, *Initation of cavitation of polypropylene during tensile drawing.* Macromolecules, 2011. **44**: p. 20-28.
32. Alicia Salazar, T.M., José M. Navarro, Jesús Rodríguez, *Fracture behavior of controlled-rheology ethylene-propylene block copolymers.* Polym Int, 2011. **60**: p. 765-771.